https://orcid.org/0009-0003-8652-7574

VILNIUS UNIVERSITY
CENTER FOR PHYSICAL SCIENCES AND TECHNOLOGY

Jurgita
KONCEVIČIŪTĖ

Theoretical Study of Electron-Impact Double and Triple Ionization Using a Multi-Step Approach

DOCTORAL DISSERTATION

Natural Sciences,
Physics (N 002)

Vilnius, 2023

Doctoral Dissertation was completed during 2016-2022 at Vilnius University, Institute of Theoretical Physics and Astronomy.

Academic supervisor - Assoc. Prof. Dr. Valdas Jonauskas (Vilnius University, Natural Sciences, Physics, N 002).

https://orcid.org/0009-0003-8652-7574

VILNIAUS UNIVERSITETAS
FIZINIŲ IR TECHNOLOGIJOS MOKSLŲ CENTRAS

Jurgita
KONCEVIČIŪTĖ

Teorinis dvigubos ir trigubos jonizacijos elektronais tyrimas taikant kelių žingsnių metodą

DAKTARO DISERTACIJA

Gamtos mokslai,
Fizika (N 002)

Vilnius, 2023

Contents

1. LIST OF ABBREVIATIONS

AI Autoionization
BE Binary-encounter
BED Binary-encounter-dipole
CE Collisional excitation
CI Collisional ionization
CIS Configuration interaction strength
SCSF Single configuration state function
DC Dielectronic capture
DDI Direct double ionization
DDI-AI Direct double ionization-autoionization
DDI-EII Direct double ionization process through the excitation-ionization-ionization path
DDI-II Direct double ionization process through the ionization-ionization path
DDI-IEI Direct double ionization process through the ionization-excitation-ionization path
DDI(EII)-AI Direct double ionization process through the excitation-ionization-ionization path, followed by autoionization
DDI(IEI)-AI Direct double ionization process through the ionization-excitation-ionization path, followed by autoionization
DDI(II)-AI Direct double ionization process through the ionization-ionization path, followed by autoionization
DFS Dirac-Fock-Slater
DI Double ionization
DW Distorted wave
EA Excitation autoionization
EDA Excitation-double autoionization
EI-AI Excitation-ionization-autoionization
EII Excitation-ionization-ionization
FAC Flexible Atomic Code
HF Hartree-Fock
IA Ionization-autoionization
IE-AI Ionization-excitation-autoionization
IEI Ionization-excitation-ionization
IDI Indirect double ionization

II Ionization-ionization

MRC Maxwellian rate coefficients

NIST National Institute of Standarts and Technology

REDA Resonant-excitation–double-autoionization

RETA Resonant excitation triple autoionization

SI Single ionization

TDCC Time-dependent close-coupling

TI Triple ionization

2. INTRODUCTION

Microscopic many-particle systems featuring long-range Coulomb interactions are of fundamental importance for understanding of the universe. The pairwise interactions govern atomic and nuclear systems. One of the universe's fundamental interactions, is the Coulomb potential, a $1/r$ interaction, which strength is directly proportional to particle charges and inversely proportional to inter-particle distances. This interaction exhibits a long-range character, allowing it to influence systems even at effectively infinite distances. However, this long-range nature creates divergence problems that affect various branches of physics, from quantum mechanics and quantum electrodynamics to field theories, statistical physics, celestial mechanics, and cosmology [1]. Despite being recognized for a long time, these challenges remain unresolved.

Atomic physics focuses on the time-dependent properties of atomic systems, including their structure, interactions, and dynamics. The ultimate aim of both experimental and theoretical work in this field is to provide a quantitative description of the relationships between microscopic and macroscopic characteristics.

In the early 20th century, atomic physics emerged as a distinct field of study [2]. Initially, it was primarily considered a pure fundamental science with no immediate practical applications. However, this perspective has undergone a significant transformation over time. Atomic physics, driven by intensive fundamental research, has not only made substantial contributions to our fundamental understanding of nature but has also witnessed a remarkable increase in the number of scientific and technical applications.

An unprecedented demand for precise atomic data has arisen due to the necessity for predicting and analyzing experimental data gathered by various space missions (e.g., AXAF, SOHO, Chandra, XMM, Hubble Space Telescope, etc.) and ground-based instruments. This demand is particularly significant for ions with relatively high abundances, requiring greater accuracy in available atomic data. Furthermore, previously undetected elements from ground-based instruments have now been observed in stellar objects, especially the heavy elements [3].

Moreover, there is a significant demand for precise atomic data to determine physical conditions such as temperature and densities in current

and future fusion research programs, including ITER and laser fusion [3]. Furthermore, accurate atomic data are essential for understanding the fundamental interactions in nature and correlations in quantum many-particle systems.

Electron-impact single and multiple ionization processes provide an understanding of the electronic dynamics and the structure of the target therefore these processes have applicability that varies from plasma physics [4], stellar atmospheres [5, 6] to cancer treatment by irradiation [7–9].

The word "plasma" is used in physics to designate the high temperature ionized gaseous state with charge neutrality and collective interaction between the charged particles and waves [10]. Plasma constitutes over 99% of the observable universe and has significant potential for various applications.

Within the plasma environment, a multitude of ionization processes affecting atoms occur. Consequently, numerous atomic processes emerge, which not only contribute to the evolution of the plasma but also serve as important elements in its diagnostics. Alongside radiative processes, a diverse range of atomic collisional phenomena plays a significant role in calculating radiation emissions [11].

In plasmas, as well as in other environments with abundances of high-energy electrons, multiple ionization has considerable impact on charge-state distribution [6, 12]. The study of the multiple ionization processes is quite complicated as one has to deal at least with four body Coulomb problem.

From a theoretical atomic perspective, electron collision processes in both astrophysical and magnetic fusion plasmas have much in common. Both require data for excitation, ionization and recombination for a multitude of elemental ions. Therefore electron-impact single and multiple ionization processes have been the focus of many theoretical and experimental studies. An information about such small systems like atoms and ions can be obtained by perturbing the system under investigation. Collisions of the atomic systems with electrons is a typical method for such studies. Products of these processes are singly and multiply ionized ions, which can be measured directly in experiments.

The most direct source of information regarding electron-ion collisions is the technique of interacting particle beams. Over half a century

ago, Dolder et al. [13] first reported the use of colliding beams with an accelerated ion beam. Their pioneering measurement of electron-impact ionization of He^+ set a high standard for subsequent colliding-beams experiments. Since then, the colliding-beams method has been employed in numerous measurements of fundamental processes, including elastic scattering, excitation, ionization, and recombination [14].

Another method to obtain data for electron collisions with atoms is through numerical calculations. These calculations have seen significant enhancements in both accuracy and complexity, driven by the rapid progress in computational methodologies and advancements in hardware technology.

Numerical methods can generally be classified as either perturbative or non-perturbative. In perturbative methods, the effect of the target on collision outcomes is handled through variants of the Born series, such as first-order or second-order plane-wave or distorted-wave Born approximations. On the other hand, non-perturbative methods aim to solve the time-independent Schrödinger equation for a fixed collision system energy. While some computer codes have been developed to solve the time-dependent Schrödinger equation, this often requires significant approximations regarding the target structure, limiting result accuracy. Additionally, there are semi-empirical methods available, primarily used for specific purposes [15]. Successful computational techniques have been developed in formal ionization theory to fully address ionization problems without relying on limiting approximations. These techniques encompass methods such as exterior complex scaling [16], convergent close coupling [17], R-matrix with pseudo-states [18], and time-dependent close-coupling (TDCC) [19]. However, these methods are computationally intensive and are primarily applicable to simple atoms and low-impact energies. Therefore perturbative methods are still widely used.

In this study, an investigation of electron-impact single ionization (SI), double ionization (DI), and triple ionization (TI) processes was performed for B^+, Se^{2+}, and Se^{3+} ions. As demonstrated later in this work, in addition to pure theoretical interest, SI, DI, and TI cross sections of these ions are required for various applications. Hence, these ions were chosen for this study.

Boron, one of the three light elements (Li, Be, B) that cannot be

effectively synthesized by nuclear reactions in stable stars, is relatively scarce in the solar system and stars, with lower abundances compared to neighboring elements on the periodic table [20]. However, boron plays a crucial role in fusion devices. Here, plasma-induced deposition of boron-containing films on plasma-exposed surfaces, known as boronization, serves as a powerful method for achieving highly pure fusion plasmas [21, 22]. To comprehend the erosion processes of neutral and ionized boron in fusion experiments like ITER, comprehensive data on electron collisions with these ions are essential. These data should encompass not only collisions with atoms and ions in their ground state but also those involving excited states.

Previous nonperturbative calculations have been conducted for electron-impact ionization of the B atom [23, 24], as well as the B^+ [25] and B^{2+} [26] ions in their ground and metastable states. Crossed-beams experiments were employed to obtain SI cross sections for the B^+ ion [25, 27].

For the electron-impact DI of the B^+ ion, previous studies utilized the nonperturbative TDCC method to address the direct double ionization (DDI) process and the perturbative time-independent distorted wave approximation for the indirect DI processes [28]. However, TDCC calculations are limited to the energy range between the DDI threshold and the inner-shell SI threshold. Notably, there is a lack of both experimental results and theoretical studies for the TI process of the B^+ ion.

The merger of two neutron stars or a neutron star with a black hole results in the production of elements heavier than iron through rapid neutron capture (r-process) nucleosynthesis [29]. Simulation models, which incorporate the full general relativistic framework along with neutrino transport, have shown a significant abundance of elements with an atomic mass number $A \sim 90$ [30]. Among the elements generated in this merging process, selenium is notably produced with a high probability.

Furthermore, selenium has been observed in a variety of astrophysical nebulae and metal-poor stars [31–36]. Its presence in these celestial objects makes selenium a valuable element for investigations related to nucleosynthetic models of stellar populations.

The first and to date the only experimental investigations of electron-impact SI, DI, and TI for Se ions were conducted at the Multicharged Ion Research Facility of the University of Nevada in Reno, employing the

dynamic-crossed-beams technique [37]. These experiments measured the absolute cross sections for SI to TI of Se^{2+} ions from their ionization thresholds up to 500 eV [38] and Se^{3+} ions from their ionization thresholds up to 1 keV [39].

To compare these experimental results, the Lotz semi-empirical formula for direct ionization [40] was employed. Significant differences were noted, suggesting a substantial contribution from indirect processes. In the case of DI of Se^{2+} [38], a least-squares fit to the experimental data was achieved using a semi-empirical formula [41].

Ab initio investigations were previously carried out for electron-impact SI and DI cross sections, focusing on the ground configurations of Se^{2+} and Se^{3+} ions. These calculations employed the semi-relativistic configuration-average distorted-wave (CADW) method [42]. Additionally, electron-impact SI of the Se^{3+} ion was studied through level-to-level calculations [43]

In this study, electron-impact DI and TI processes for B^+, Se^{2+}, and Se^{3+} ions are investigated using a multi-step approach [44]. This approach encompasses ionization-ionization (II), excitation-ionization-ionization (EII), and ionization-excitation-ionization (IEI) processes.

The impact of several processes on DI is analyzed, including ionization-autoionization (IA), excitation-double autoionization (EDA), DDI, and resonant excitation triple autoionization (RETA) processes. For B^+ ions, in addition to these processes, two-step processes are also considered in the study of DI. These additional processes involve ionization-excitation-autoionization (IE-AI) and excitation-ionization-autoionization (EI-AI).

The electron-impact TI process is examined as a result of the DDI-AI process and Auger cascade following SI of the inner shell of the initial ion. DI and TI processes of the Se^{3+} ion are examined through level-to-level calculations.

The contribution from various atomic shells can be of significance when modeling non-equilibrium plasma. Consequently, cross sections and rates for distinct processes and various shells are also provided.

The atomic data required for studying electron-impact SI, DI, and TI cross sections, including energy levels, radiative and Auger transition probabilities, as well as electron-impact excitation and ionization cross sections, are computed using the Flexible Atomic Code (FAC) [45],

which employs the Dirac-Fock-Slater (DFS) approach. Continuum orbitals of incident and scattered electrons are assessed in the potentials of ionizing and ionized ions to compare with experimental results. The electron-impact excitation and ionization processes are examined using the distorted wave (DW) approximation.

2.1. The Main Goal of this Work

The main goal of this research is to investigate the processes of electron-impact DI and TI employing a multi-step approach, with the aim of suggesting efficient techniques for achieving precise theoretical cross-sections.

2.2. The Main Tasks of the Thesis

1. Investigation of SI processes:

   - study of SI by electron impact using the DW approach;
   - examination of SI cross sections within the potentials of ionizing and ionized ions;
   - investigation of the influence of correlation effects on SI cross sections.

2. Investigation of DDI processes:

   - study of the DDI process by electron impact using the multi-step approach;
   - analysis of the energy distribution of the electron participating in the subsequent ionization or excitation process after the initial interaction;
   - assessment of the impact of the electron-impact TI process on DI direct ionization cross sections.

3. Investigation of indirect double ionization (IDI) processes:

   - study of SI-autoionization (AI) process;
   - study of the contributions of excitation-ionization-autoionization (EI-AI) and ionization-excitation-autoionization (IE-AI) processes;
   - investigation of the RETA process.

4. Investigation of TI processes:

   - study of a TI process as a DDI process followed by an AI process (DDI-AI);

- Investigation of the influence of Auger cascades on TI.

5. Analysis of the scaled DW cross sections:

   - study of scaled collisional ionization (CI) cross sections;
   - analysis of scaled cross sections in the excitation autoionization (EA) process.

2.3. The Scientific Novelty

1. Correlation effects were investigated for Se^{2+} and B^+ ions.

2. The study demonstrated the significant contribution of three-step processes to DDI cross sections for Se^{2+} and B^+ ions.

3. The research identified the important contribution of EI-AI and IE-AI processes to DI cross sections for the B^+ ion.

4. Scaling functions for electron impact collisional excitation (CE) and CI cross sections, obtained using the DW approximation, were applied to explain experimental measurements of the B^+ ion.

5. The influence of the TI process was demonstrated in the theoretical study of DI cross sections for Se^{2+}, Se^{3+}, and B^+ ions.

6. The TI process was investigated using a multi-step approach to estimate DDI in the DDI-AI part of TI.

2.4. Statements to Defend

1. Three-step processes contribute up to approximately 40% of the total DDI cross sections for Se^{3+} ion.

2. EI-AI and IE-AI processes make up approximately 9% of the total DI cross sections for B^+ ion.

3. Correlation effects reduce electron-impact DI cross sections for Se^{3+} and B^+ ions.

4. Scaling of the DW cross sections has to be utilized to explain the experimental data for the DI of B^+.

5. The DDI-AI process constitutes over 75% of the total TI cross sections for Se^{2+} and Se^{3+} ions.

2.5. Personal Contribution

1. Performed research tasks.

2. Carried out calculations, which included electron-impact SI, DI, and TI ionization cross sections using various methods.

3. Collected and analyzed theoretical and experimental data from references for comparisons with calculated results.

4. Performed an analysis of the calculated data.

5. Prepared manuscripts for articles A1, A2, and A3, as well as conference presentations C1, C2, and C5.

6. Contributed ideas and provided roadmaps to achieve scientific goals.

7. Prepared and updated scripts for various computational tasks.

2.6. Thesis Outline

The doctoral dissertation is organized into several chapters, each addressing specific aspects of the research problem and presenting the findings. Here is a breakdown of the structure outlined:

Introduction chapter:

- Provides an introduction to the research problem, highlighting its significance and relevance.

- Discusses the scientific novelty of the research.

- States the main goal and tasks of the scientific study.

- Outlines the key statements of the dissertation.

Theoretical Methods chapter:

- Presents the scientific methods used to investigate electron-impact SI, DI, and TI and is divided into subsections focusing on different aspects of the methods.

- Describes the construction of wave functions.

- Discusses the calculation of Auger transitions, electron-impact excitation, and ionization cross sections.

- Provides an explanation of the DW approximation used in the calculations.

- Introduces scaling factors employed for DW cross sections.

- Presents a multi-step approach, which is applied to study electron-impact DI and TI processes.

Results chapter:

- Divided into sections corresponding to the specific processes studied.

- Presents the energy levels, ionization thresholds, and electron-impact SI, DI, and TI cross sections for B^+, Se^{2+}, and Se^{3+} ions.

Conclusions chapter:

- Summarizes the main conclusions drawn from the research.

- Relates the conclusions to the initial statements of the dissertation.

3. THEORETICAL APPROACH

3.1. Dirac-Fock-Slater approach

Even in the simplest case of a multi-electron atom, such as the two-electron Helium atom, achieving an exact theoretical treatment is challenging. The primary obstacle arises from the interactions between the electrons. These interactions, characterized by a non-spherical symmetry, prevent the Schrödinger equation from being separated, as is the case of one-electron atoms. To address this issue, one must resort to either numerical methods or approximate models that allow for analytical calculations.

In the independent electron model, the interactions between the electrons within an ion are not explicitly introduced. Instead, they are implicitly accounted for by employing an effective potential. This potential depends on both the nuclear charge and the time-averaged spherical charge distribution resulting from all the other electrons. One of such methods is DFS approximation [46, 47].

According to DFS approximation, the Hamiltonian H for an ion with N bound electrons and nuclear charge Z is given by

$$H = \sum_{i=1}^{N} H_D(i) + \sum_{\substack{i,j \\ i<j}}^{N} \frac{2}{r_{ij}}, \tag{1}$$

Here, $H_D(i)$ is the single-electron Dirac Hamiltonian for a pure Coulomb potential $-2Z/r_i$ due to the nucleus of the ion, r_{ij} is the distance between each two interacting electrons.

Hamiltonian H can be rewritten by adding and subtracting the electron-electron electrostatic contributions $V^{ee}(r_i)$ to the central potential $V(r_i)$ as follows,

$$H = \sum_{i=1}^{N} H'_D(i) - \sum_{i=1}^{N} V^{ee}(r_i) + \sum_{\substack{i,j \\ i<j}}^{N} \frac{2}{r_{ij}}, \tag{2}$$

where

$$H'_D = H_D + V^{ee}(r_i). \tag{3}$$

Thus, H'_D is the single-electron Dirac Hamiltonian with the local central potential

$$V(r_i) = V^N(r_i) + V^{ee}(r_i). \qquad (4)$$

This local central potential includes the contributions from the nuclear charge $V^N(r)$ and the electron-electron interaction $V^{ee}(r)$.

The nuclear potential can be expressed as

$$V^N(r) = \frac{-2Z(r)}{r}, \qquad (5)$$

here, distributed nuclear charge $Z(r)$ is used, which differs from Z only for extremely small values of r.

In the DFS approach the relativistic version of the Hartree-Fock-Slater potential [48] is used for the central potential. The electron-electron interaction potential $V^{ee}(r)$ includes the spherically averaged classical potential due to the bound electrons and a local approximation to the exchange energy,

$$
\begin{aligned}
V^{ee}(r) = V_c(r) - V_{ex}(r) = \\
= \sum_{nk} \int \frac{\omega_{n\kappa}}{r_>} (P_{n\kappa}^2(r) + Q_{n\kappa}^2(r)) - \\
- \left[\frac{3}{4\pi^2 r^2} \sum_{n\kappa} \omega_{n\kappa}(P_{n\kappa}^2(r) + Q_{n\kappa}^2(r)) \right]
\end{aligned}
\qquad (6)
$$

This expression includes the self-interaction, which is undesirable. It also has incorrect asymptotic behaviour. To exclude self-interaction, the following expression was used to describe local central potential electron-electron interaction [45]:

$$
\begin{aligned}
V^{ee}(r) = \frac{1}{r \sum_a \omega_a \rho_a(r)} \Bigg\{ \sum_{ab} \omega_a(\omega_b - \delta_{ab}) Y_{bb}^0(r)\rho_a(r) \\
+ \sum_a \omega_a(\omega_a - 1) \sum_{k>0} f_k(a,a) Y_{aa}^k(r)\rho_a(r) \\
+ \sum_{a \neq b} \sum_k \omega_a \omega_b g_k(a,b) Y_{ab}^k(r)\rho_{ab}(r) \Bigg\},
\end{aligned}
\qquad (7)
$$

where $\alpha = n\kappa$ and $\alpha = n'\kappa'$ are virtual indices denoting the subshells and

$$\rho_{ab} = P_a(r)P_b(r) + Q_a(r)Q_b(r),$$

$$Y_{ab}^k(r) = r \int \frac{r_<^k}{r_>^{k+1}} \rho_{ab}(r') \, dr' ,$$

(8)

here, $r <$ and $r >$ note the lesser and greater of r and r' respectively. f_k and g_k are the direct and exchange coefficients defined as

$$f_k(a,b) = -(1 + \frac{1}{2j_a}) \begin{pmatrix} j_a & k & j_b \\ -\frac{1}{2} & 0 & \frac{1}{2} \end{pmatrix}^2$$

$$g_k(a,b) = \begin{pmatrix} j_a & k & j_b \\ -\frac{1}{2} & 0 & \frac{1}{2} \end{pmatrix},$$

(9)

where $\begin{pmatrix} j_1 & j_2 & j_3 \\ m_1 & m_2 & m_3 \end{pmatrix}$ is the Wigner $3j$ symbol. The equation has the correct asymptotic behaviour at large r since the self-interaction term is explicitly excluded.

The coupled Dirac radial equations determining $P_{n\kappa}$ and $Q_{n\kappa}$ are

$$\left[\frac{d}{dr} + \frac{\kappa}{r} \right] P_{n\kappa}(r) = \frac{\alpha}{2} \left[\varepsilon_{n\kappa} - V(r) + \frac{4}{\alpha^2} \right] Q_{n\kappa}$$

(10)

and

$$\left[\frac{d}{dr} - \frac{\kappa}{r} \right] Q_{n\kappa}(r) = \frac{\alpha}{2} \left[V(r) - \varepsilon_{n\kappa} \right] P_{n\kappa},$$

(11)

where α is the fine-structure constant and $\varepsilon_{n\kappa}$ are the energy eigenvalues of the radial orbitals.

Basis states $\Phi_\nu(1, 2, \ldots, N)$, that are single configuration state functions (SCSF) are used in treating an atomic system with N bound electrons. SCSFs are antisymmetric sums of the products of N single-electron Dirac spinors, given by equation

$$u_{n\kappa m}(x) = \frac{1}{r} \begin{bmatrix} P_{n\kappa} & \chi_{\kappa m}(\theta, \phi, \sigma) \\ iQ_{n\kappa} & \chi_{-\kappa m}(\theta, \phi, \sigma) \end{bmatrix},$$

(12)

where χ stands for both spatial and spin coordinates of the electron [46].

In forming the Φ_ν, the standard jj-coupling scheme is followed:

- The j values of all electrons in a subshell $n_r l_r j_r$ are coupled together to form a total angular momentum J_r of the subshell.

- Total subshell values for the angular momentum are successively coupled together, starting with the lowest subshell, to form the total angular momentum J of the ion.

One then obtains approximate, fine-structure ion wave functions Ψ given by

$$\Psi = \sum_{\nu=1}^{NSCFS} b_\nu \Phi_\nu, \tag{13}$$

where b_ν are the mixing coefficients, which together with corresponding eigenenergies are obtained by diagonalizing the Hamiltonian (see Eq. (2)) , expressed in the Φ_ν basis.

3.2. Correlation Effects

The total wave function obtained through the DFS approximation is never an exact solution to the Schrödinger equation. As mentioned earlier in this work, the presence of a two-electron term in the actual Hamiltonian prevents its representation as a sum of one-electron operators. This limitation makes the separation of variables in the Schrödinger equation impossible. The DFS approximation, which is based on the Hartree-Fock (HF) approach, utilizes an effective potential that characterizes the average electrostatic interaction experienced by an individual electron within a multi-electron system.

In order to address electronic states that could not be adequately described using single-configuration wave functions, the concept of configuration interaction and its various forms emerged within the field of atomic electronic structure theory. Configuration interaction involves the perturbation of an electronic configuration by neighboring configurations [49].

Consequently, the correlation energy E_{corr} for a certain state with respect to a specified Hamiltonian is defined as the difference between the exact eigenvalue of the Hamiltonian E_{exact} and its expectation value in the HF approximation E_{HF} for the state under consideration [50]:

$$E_{corr} = E_{exact} - E_{HF} \tag{14}$$

The many-configuration method represents one of the approaches used to incorporate electron correlations. In this method, the atom's wave function is expanded not only in terms of the basis functions of its own configuration but also in terms of other configurations that share the same parity [51, 52]:

$$\Phi(\Gamma J) = \sum_{K'\gamma'} C^{\Gamma}_{K'\gamma'J} \Psi(K', \gamma', J). \tag{15}$$

Here, $C^{\Gamma}_{K'\gamma'J}$ represents the expansion coefficient, Ψ stands for the one-configuration function, which can be defined within either a one-configuration or many-configuration approximation. Meanwhile, Φ denotes the many-configuration function that corresponds to a combination of various configurations. Here, K represents a specific configuration, and Γ denotes a many-electron state.

If the functions Φ are calculated in a one-configuration approximation, and the expansion coefficients are defined by diagonalizing the energy matrix in the basis of these functions, we then have a simpler version of the many-configuration method, called the method of configuration interaction.

It is important to emphasize that configurations differing from one another by the quantum numbers of more than two electrons only influence each other through interactions with other configurations. In an orthonormalized basis, many-configuration matrix elements tend to zero for such configurations.

By increasing the configuration basis, the convergence of the configuration interaction method occurs rather slowly. Therefore, the average characteristics of configuration interaction can be successfully applied for the selection of the most important configurations that are admixed to the considered configuration.

According to the energy correction in second-order perturbation theory and to the wave function correction in first-order perturbation theory, stronger mixing of levels of two configurations occurs when the interconfiguration matrix elements are larger, and these levels are closer in energy to one another. This allows to introduce a new quantity for estimating the degree of mixing - the configuration interaction strength

(CIS). Previously, the CIS method has been successfully employed for investigating energy levels [53], Auger cascades [54–56], as well as electric dipole [57] and magnetic dipole [58, 59] transitions.

The expression for CIS can be written as:

$$T(K,K') = \frac{\sum_{\gamma\gamma'} \langle K\gamma|H|K'\gamma'\rangle^2}{\sigma^2(K, K')}. \tag{16}$$

Here, summation is performed over all states γ and γ' of configurations K and K' and the variance of the energy distances between interacting levels of both configurations is denoted by $\sigma^2(K,K')$.

A simpler expression for CIS can also be formulated. In this version, the difference in the average distance between two interacting configurations, denoted as $E_{av}(K, K')$, is employed instead of the variance in distances [60]:

$$T(K,K') = \frac{\sum_{\gamma\gamma'} < K\gamma|H|K'\gamma' >^2}{E_{av}(K,K')^2}. \tag{17}$$

The CIS $T(K, K')$, divided by the number of states of configuration K that are mixed with states of configuration K', denoted by $\beta(K, K')$, approximately is equal to the square of mixing coefficient at the wave function of configuration K' in the expansion of the wave function of configuration K:

$$c^2 = \frac{T(K,K')}{\beta(K, K')}. \tag{18}$$

3.3. Distorted Wave Approximation

The DW approximation was first introduced in 1933 to address electron-scattering problems. In their initial paper [61], Massey and Mohr considered the distortion only for the incident wave. However, in their subsequent work [62], they extended their investigation to encompass the distortion effects on both the incident and scattered waves. This marked the first instance in which numerical results for cross-section calculations using the DW approximation were provided.

However, this approach received relatively little attention until the 1970s. Interest in the DW approximation increased significantly when

other plane-wave approximations proved inadequate for explaining newly available experimental data. Additionally, the resurgence of interest in DW approximation was facilitated by the availability of computing machinery capable of accurately performing DW calculations [63]. The DW approximation has become a fundamental tool in atomic and molecular physics. It is used to study a wide range of processes, including electron-atom collisions, electron-molecule interactions, and more.

The DW method is defined based on two fundamental assumptions [64]:

1. The interaction between the electron and the target atom (ion), leading to excitation, is addressed through perturbation theory.

2. The presence of the target atom (or ion) induces a distortion in the waves of the scattering electrons.

Various versions of the DW approximations exist, each involving distinct methods for introducing the distortion for the electron wave. Coulomb-wave Born approximation is one of these approximations. This approximation considers the distortion of the continuum due to a pure Coulomb potential. The most precise within this category is the DW Born approximation. In this approach, the free orbitals are computed within a more realistic potential, which takes into consideration the electronic structure of the target ion.

3.3.1. Electron-Impact Excitation

Regarding electron impact excitation, the DW approximation addresses two distinct scenarios that involve incident electrons interacting with the initial-state atomic potential:

1. In the direct process, the atomic system undergoes excitation, simultaneously the incident electron transitions to a state in which it is scattered by the final-state atomic potential.

2. In the exchange process, the atomic system is excited as one of its bound electrons is ejected into an elastic-scattering state. Concurrently, the incident electron is captured into a bound state of the atom.

In both instances, perturbation techniques are utilized to compute the transitions between the initial and final scattering states. This effectively considers the electronic structure of the target atomic system.

In the relativistic case, the collision strength Ω_{01} is related to the collisional cross section σ_{01} through [65]

$$\sigma_{01}(\varepsilon) = \frac{\pi a_0^2}{(2J_1 + 1)} \frac{1}{p^2} \Omega_{01}, \tag{19}$$

where the subscripts 01 refer to initial and final states, a_0 is the Bohr radius, $2J_1+1$ is the statistical weight of the initial state, p is the relativistic momentum and ε is the incident electron energy. The collision strength can be written as,

$$\Omega_{01} = 2 \sum_{\kappa_0 \kappa_1} \sum_{J_T} [J_T] \, |\langle \psi_0 \kappa_0, J_T M_T | \sum_{i<j} \frac{1}{r_{ij}} |\psi_1 \kappa_1, J_T M_T \rangle|^2, \tag{20}$$

where κ_0 and κ_1 represent the relativistic angular quantum numbers of the incident and scattered electrons, respectively, J_T signifies the total angular momentum when the target state is coupled to the continuum orbital, M_T denotes the projection of the total angular momentum, and $[J] = 2J + 1$. The distance between two electrons is denoted as r_{ij}. The wave functions for the initial and final states of the bound electrons are represented as ψ_0 and ψ_1, respectively.

This expression can be simplified to give,

$$\Omega_{01} = 2 \sum_k \sum_{\substack{\alpha_0 \alpha_1 \\ \beta_0 \beta_1}} Q^k(\alpha_0 \alpha_1; \beta_0 \beta_1) < \psi_0 || Z^k(\alpha_0, \alpha_1) || \psi_1 >$$
$$< \psi_0 || Z^k(\beta_0, \beta_1) || \psi_1 >, \tag{21}$$

where

$$Q^k(\alpha_0 \alpha_1; \beta_0 \beta_1) = \sum_{\kappa_0 \kappa_1} [k]^{-1} P^k(\kappa_0 \kappa_1; \alpha_0 \alpha_1) P^k(\kappa_0 \kappa_1; \beta_0 \beta_1) \tag{22}$$

and

$$P^k(\kappa_0 \kappa_1; \alpha_0 \alpha_1) = X^k(\alpha_0 \kappa_0; \alpha_1 \kappa_1)$$
$$\sum_t (-1)^{k+t} [k] \begin{pmatrix} j_{\alpha_0} & j_1 & t \\ j_0 & j_{\alpha_1} & k \end{pmatrix} X^t(\alpha_0 \kappa_0; \kappa_1 \alpha_1). \tag{23}$$

Here, $Z^k(\alpha,\beta)$ is an operator, defined in [66].

$$X^k(\alpha\beta;\gamma\delta) = <\alpha||C^k||\gamma><\beta||C^k||\delta>R^k(\alpha\beta;\gamma\delta), \qquad (24)$$

where C^k is the normalized spherical harmonic tensor, and R^k is the generalized Slater integral.

3.3.2. Electron-Impact Ionization

Originally, DW approximation was primarily applied to electron-scattering problems in excitation processes. However the expression for the electron impact ionization cross section differential in energy of the ejected electron within the DW approximation, can be derived from the electron impact ionization formula. The ionization process requires replacing one bound orbital in the final state with the free orbital of the ejected electron and then performing a summation over its angular momentum. In terms of collision strength Ω, the electron impact ionization cross-section can be expressed as [45]:

$$\sigma(\varepsilon_0,\varepsilon) = \frac{1}{k_0^2 g_0}\Omega_{01}, \qquad (25)$$

where the energy and kinetic momentum of the incident electron are represented as ε_0 and k_0, respectively, and ε signifies the energy of the ejected electron.

The expression for the collision strength Ω_{01} is as follows:

$$\Omega_{01} = 2 \sum_{\substack{\kappa, J_T, \\ k, \alpha_0\beta_0}} Q^k(\alpha_0\kappa;\beta_0\kappa) < \psi_0||Z^k(\alpha_0,\kappa)||\psi_1,\kappa;J_T > \\ < \psi_0||Z^k(\beta_0,\kappa)||\psi_1,\kappa;J_T >, \qquad (26)$$

where κ denotes relativistic angular quantum number of the ejected electron, the total angular momentum of the final state coupled with the ejected electron is denoted by J_T. The radial part Q^k is identical to that for excitation process, the only difference is that free orbital replaces one of the the bound ones in the final state.

The total ionization cross section is obtained by integrating Ω_{01} over the energy of the ejected electron ε,

$$\sigma(\varepsilon_0) = \int_0^{(\varepsilon_0 - I)/2} \frac{1}{k_0^2 g_0} \Omega_{01} \, d\varepsilon \qquad (27)$$

where I is defined as ionization energy, ε_0 and k_0 are the energy and kinetic momentum of the incident electron, ε is the energy of the ejected electron and g_0 is a statistical weight of the initial state.

3.4. Scaling of Distorted Wave Cross Sections

Throughout the years, numerous authors have made attempts to describe the functional relationship of electron impact ionization cross sections through theoretical or empirical formulas. The initial semiempirical formula, which provided a reasonably accurate description of direct SI by electron impact, was presented by Lotz [40]. Subsequently, multiple efforts were undertaken to suggest various fitting guidelines for electron-impact single and multiple ionization [67].

The binary-encounter-dipole and binary-encounter-Bethe models for CI and the scaled plane-wave Born approximation for the CE were developed to study the cross sections for neutral atoms and near neutral ions [68–71]. Application of this scaling approach for plane-wave cross sections led to a good agreement with experimental data [72, 73].

The scaling method was initially developed to address limitations of the plane-wave Born approximation, which include [69]:

- the electron exchange effect with the target electrons,

- the distortion of plane waves near the target atom,

- polarization of the target induced by the incident electron.

It is important to note that the proposed scaling method is free from adjustable parameters, as it relies solely on atomic properties:

1. ionization energy,

2. excitation energy.

It is well known that the DW approximation often overestimates the electron-impact ionization and excitation cross sections for atoms and near neutral ions. Since these scaling factors have been demonstrated

to be successful in CE and CI studies using the plane-wave Born approximation, they were also applied to reduce the DW cross sections for the electron-impact ionization and excitation processes [74–76]. Furthermore, this scaling not only reduces the cross section magnitude at low ε but also shifts the peak to a higher ε while keeping validity of the original cross sections at high ε intact.

Following equation describes the scaled DW cross sections (σ^{CE^*}) for CE:

$$\sigma_{ik}^{\mathrm{CE}^*}(\varepsilon) = \frac{\varepsilon}{\varepsilon + E_{ik} + \varepsilon_b} \sigma_{ik}^{\mathrm{CE}}(\varepsilon), \tag{28}$$

where ε_b is the binding energy of the electron being excited, E_{ik} is a transition energy between the level i and the level k, and $\sigma_{ik}^{\mathrm{CE}}(\varepsilon)$ is the electron-impact excitation cross section.

The scaled CI cross sections (σ^{CI^*} for neutral atoms are represented by the following equation:

$$\sigma_{if}^{\mathrm{CI}^*}(\varepsilon) = \frac{\varepsilon}{\varepsilon + I + \varepsilon_k} \sigma_{if}^{\mathrm{CI}}(\varepsilon), \tag{29}$$

here, I is the ionization threshold of the ground state and ε_k represents the kinetic energy of the bound electron.

The equation for scaled CI cross sections for near-neutral ions can be expressed as:

$$\sigma_{if}^{\mathrm{CI}^*}(\varepsilon) = \frac{\varepsilon}{\varepsilon + I} \sigma_{if}^{\mathrm{CI}}(\varepsilon), \tag{30}$$

3.5. Radiative Transitions

To estimate the impact of radiative transitions between various levels of an ion following the interaction with an impacting electron on the DI process, branching ratios of the AI process are necessary. Calculating the branching ratios requires information on radiative transition rates. The Hamiltonian describing the interaction between an atom and radiation can be expressed as the sum of the multipole transition operators. The equation for the electric multipole (dipole or quadrupole) transition operators can be written as [51]

$$O_p^{(t)} = -e \sum_i r_i^t C(t)_p (\theta_i, \phi_i), \tag{31}$$

here, e is an elementary charge, a particle position operator is denoted by r_i^t, and $C(t)_p$ is a spherical function operator. Coordinates of all electrons of an atomic system are denoted by subscript i. $O^{(1)} \equiv D^{(1)}$ and $^{(1)}$ are dipole and quadrupole moments of electron shells respectively. According to the Wigner-Eckart theorem, the matrix element of a transition operator depends on the projection of the total momentum:

$$<\gamma J M | O_p^{(t)} | \gamma' J' M'> = (-1)^{J-M} \begin{pmatrix} J & t & J' \\ -M & p & M' \end{pmatrix}$$

$$<\gamma J || O^{(t)} || \gamma' O(t) || \gamma' J' > . \tag{32}$$

In this work radiative transition rates are calculated in the single multipole approximation. This means that the interference between different multipoles is not taken into account. For a given multipole operator O_M^L and initial and final states of the transition $\psi_i = \sum_\nu b_{i\nu} \Phi_\nu$ and $\psi_f = \sum_\mu b_{f\mu} \Phi_\mu$, the line strength of the transition is

$$S_{fi} = \left| < \psi_f || O_M^L || \psi_i > \right|^2$$
$$= \left| \sum_{\mu\nu} b_{f\mu} b_{i\nu} \sum_{\alpha\beta} < \Phi_\mu || Z_M^L(\alpha, \beta) || \Phi_\nu > \right.$$
$$\left. < \alpha || C^L || \beta > M_{\alpha\beta}^L \right|^2, \tag{33}$$

where $M_{\alpha\beta}^L$ is the radial part of the single-electron multipole operator, which can be expressed by the equation [77]:

$$M_{\alpha\beta}^L = i^L (2L+1) \frac{c}{\omega} \int_\infty^0 j_L(\frac{\omega r}{c}) \left\{ \frac{d}{dr}(P_\alpha Q_\beta - Q_\alpha P_\beta) + \right.$$
$$\left. + (\frac{\kappa_\alpha - \kappa_\beta}{r})(P_\alpha Q_\beta - Q_\alpha P_\beta) + \frac{\omega}{c}(P_\alpha P_\beta + Q_\alpha Q_\beta) \right\} \tag{34}$$

The weighed transition rates gA_{fi} are given by,

$$gA_{fi} = 2\alpha^3 \omega^3 [L]^{-1} (\alpha\omega)^{2L-2} S_{fi}, \tag{35}$$

where transition energy is defined by $\omega = E_i - E_f$, L is the rank of the multipole operator, inducing the transition, and $[L] = 2L + 1$.

3.6. Electron-Impact Single Ionization

Electron impact SI is a process in which an incoming electron collides with an ion at sufficiently high collision energy (i.e., above the SI threshold). This collision results in the removal of one of the ion's bound electrons, thereby increasing the ion's charge state. This outcome is observed as the SI of the initial ion and is referred to as direct ionization.

In addition to the direct ionization process, there exist alternative mechanisms for ionization. One of these mechanisms involves excitation of an inner-shell electron, followed by subsequent AI. This process is commonly referred to as EA.

When an electron from an inner shell becomes excited and moves into higher unoccupied energy states, it leaves a vacancy in the inner shell. This vacancy can be filled when an electron from a higher energy state undergoes a transition into this vacant inner-shell state. During this transition, energy is generated and can be directly transferred to another electron within the same ion due to electron-electron interactions. If the binding energy of this second electron is lower than the transition energy, it can escape from the ion, resulting in AI. This specific type of AI is known as the Auger effect.

Since both direct and indirect electron-impact ionization processes contribute to electron-impact SI, the total cross section for electron-impact SI from the initial ion's level i to the level f of the singly ionized ion, denoted as σ^{SI}, can be expressed as the sum of the direct and indirect ionization cross sections using the following equation:

$$\sigma_{if}^{\text{SI}}(\varepsilon) = \sigma_{if}^{\text{CI}}(\varepsilon) + \sum_j \sigma_{ij}^{\text{CE}}(\varepsilon) B_{jf}^a, \tag{36}$$

here, $\sigma_{if}^{\text{CI}}(\varepsilon)$ represents the cross section for single CI, where ε denotes the energy of the incident electron. The expression $\sum_j \sigma_{ij}^{\text{CE}}(\varepsilon) B_{jf}^a$ represents the indirect ionization cross section. Here, $\sigma_{ij}^{\text{CE}}(\varepsilon)$ signifies the cross section for CE to the intermediate level j of the initial ion, while B_{jf}^a represents the branching ratio for the AI process from level j to the final level f.

The branching ratio represents the extent to which the indirect process is affected by radiative damping and can be mathematically represented by the following equation:

$$B_{jf}^a = \frac{A_{jf}^a}{\sum_m A_{jm}^a + \sum_n A_{jn}^r}, \qquad (37)$$

where A^a represents the Auger transition probability, while A^r denotes the radiative transition probability.

In the first-order perturbation theory, the AI rate can be written as,

$$A_\alpha = \sum_\kappa \left| < \psi_f, \kappa; J_T M_T | \sum_{i<j} \frac{1}{r_{ij}} | \psi_i > \right|^2, \qquad (38)$$

where ψ_i is the autoionizing state, ψ_f is the final state that has one less electron than ψ_i.

In the indirect SI process, the first step can involve the creation of an intermediate resonance state. During this step, an inner-shell electron gets excited, and simultaneously, the incident electron is captured into a bound state, a phenomenon known as dielectronic capture (DC). Subsequently, a highly excited, short-lived recombined ion state is formed, and in the relaxation process, two electrons can be ejected. Ultimately, as a result of this entire sequence, the ion loses one electron. The process, where the intermediate resonant state decays by sequential Auger processes is referred as resonant-excitation–double-autoionization (REDA).

The cross section for DC, which is the first step of any resonant electron–ion collision process, can be described as

$$\sigma_d^{\mathrm{DC}}(\varepsilon_e) = 7.88 \cdot 10^{-31} cm^2 eV^2 s \frac{1}{\varepsilon_e} \frac{g_d}{2g_i} \frac{A_{di}^a \cdot \Gamma_d}{(\varepsilon_e - \varepsilon_{res})^2 + \Gamma_d^2/4}, \qquad (39)$$

where ε_e is the energy of the impacting electron and $\varepsilon_{res} = E_d - E_i$ is the resonance energy obtained from the total energies of the resonant state d and the initial state i. The quantities g_d and g_i denote the statistical weights of the states d and i respectively. A_{di}^a is the AI rate from the state d to the state i and Γ_d is the total width of the state d [78].

For all electron-ion processes associated with resonances, the corresponding cross section can be calculated by multiplying the DC cross section σ_d^{DC} (Eq. (39)) by the branching ratio for the specific decay path originating from the intermediate doubly excited state d. However, it's important to note that the REDA process has not been taken into account in this study.

For some plasma applications, it is often more practical to work with Maxwellian rate coefficients (MRCs) rather than cross sections. MRCs

are calculated using the electron-impact ionisation cross sections as follows,

$$\alpha_{ij} = \left(\frac{1}{k_B T_e}\right)^{\frac{3}{2}} \left(\frac{8}{m_e \pi}\right)^{\frac{1}{2}} \int_0^\infty \varepsilon \sigma_{ij}(\varepsilon) exp\left(-\frac{\varepsilon}{k_B T_e}\right) d\varepsilon. \qquad (40)$$

In this equation, k_B represents the Boltzmann constant, m_e denotes the electron mass, and σ_{ij} stands for the cross section governing the transition from level i to level j.

3.7. Electron-Impact Double Ionization

Electron-impact DI is a process in which two electrons are removed from an atomic system by an incoming electron, leading to the creation of a doubly ionized ion. There are various mechanisms through which DI can occur, including DDI and IDI processes. In DDI, both electrons of an initial ion are simultaneously ejected due to the interaction with an external electron. IDI can involve a sequence of processes, such as an initial ionization followed by subsequent interactions that result in the removal of a second electron.

Similar to SI, the total DI cross sections can be expressed as the sum of the direct and indirect ionization cross sections:

$$\sigma_{if}^{\text{DI}}(\varepsilon) = \sigma_{if}^{\text{DDI}}(\varepsilon) + \sigma_{if}^{\text{IDI}}(\varepsilon), \qquad (41)$$

here, $\sigma_{if}^{\text{DDI}}(\varepsilon)$ is the cross section of DDI from the initial level i of the initial target ion to the final level f of the doubly ionized ion at the incident electron energy ε, and $\sigma_{if}^{\text{IDI}}(\varepsilon)$ is the cross section of IDI from the initial level i to the final level f.

3.7.1. Classical Binary Encounter Model for Electron-Impact Direct Double Ionization

During the DDI process, simultaneous emission of the two target electrons is stimulated by the incident electron. Here one has to deal with a four- body Coulomb breakup problem. Currently, only the TDCC method provides good agreement with absolute experimental measurements of total cross sections for DI of light atoms and ions [79–82].

However, investigation of the electron-impact DI of atoms and ions using the TDCC approach is a challenging computational task, therefore this method is ineffective for more complex systems.

In the classical binary encounter (BE) model proposed by Gryziński in 1965 [83], a theoretical framework was developed to describe electron impact DI processes in atomic systems. In this model, the formation of doubly ionized atomic states can occur through two distinct processes involving successive collisions:

- The first process, known as TS1, involves the ionizing incident particle, such as an electron or a photon, colliding successively with different electrons of the target atom. During these successive collisions, the ionizing particle transfers energy and momentum to the electrons, leading to their ejection from the atom. As a result, the atom becomes multiply ionized, with the number of ionized electrons depending on the energy and momentum of the incident particle and the specific target atom's properties.

- The second process, known as TS2, involves a collision between the first ejected electron and the remaining electrons within the atom. After the initial ionization event, one electron is removed from the atom, leaving behind a positively charged ion. Subsequently, the first ejected electron may collide with the remaining electrons in the ionized atom. During this collision, additional electrons may be further ejected from the atom, resulting in higher degrees of ionization.

The cross section for transferring energy ΔE from the incident particle to some of the n_e electrons of the system, considered to be in the same energy state, is $n_e \sigma_{\Delta E}$. The probability that the incident electron will collide once more with another electron of the target and transfer energy $\Delta E'$ to it is

$$\sum_i^{n_e-1} \frac{1}{4\pi} \frac{1}{r_i^2} \sigma \Delta E'(E_q - \Delta E), \tag{42}$$

The cross section for two successive collisions, in which an impacting electron loses energy $\Delta E + \Delta E'$, can be written as

$$n_e \sigma_{\Delta E}(E_q) \sum_i^{n_e-1} \frac{1}{4\pi} \frac{1}{r_i^2} \sigma_{\Delta E'}(E_q - \Delta E), \tag{43}$$

where E_q represents the initial energy of the incident electron and r_i is the distance from the electron that gained energy ΔE to the i-th electron. Under the assumption of uniform electron density in the atomic shell, denoting the average distance between electrons as $\bar{r}$ Eq. (43) can be rewritten as

$$\frac{1}{4\pi} \frac{n_e(n_e - 1)}{\bar{r}^2} \sigma_{\Delta E}(E_q) \sigma_{\Delta E'}(E_q - \Delta E.) \tag{44}$$

To eject the first electron from the system, an energy greater than the first ionization potential U_i is necessary. Similarly, to eject the next electron, an energy greater than the second ionization potential U_{ii} is needed. Ultimately, the cross section for DI by the incident electron can be expressed as follows:

$$\sigma^{TS1} = \frac{n_e(n_e - 1)}{4\pi\bar{r}^2}$$
$$\int_{U_i}^{E_q - U_{ii}} \sigma_{\Delta E} E_q \sigma_{U_{ii}}(E_q - \Delta E) d(\Delta E'). \tag{45}$$

The same rationale applied to ionization by the scattered electron during the initial interaction results in:

$$\sigma^{TS2} = \frac{n_e(n_e - 1)}{4\pi\bar{r}^2}$$
$$\int_{U_i + U_{ii}}^{E_q} \sigma_{\Delta E} E_q \sigma_{U_{ii}}(\Delta E) d(\Delta E). \tag{46}$$

The TS1 and TS2 processes are schematically illustrated in Fig. 1. Both of these processes contribute to the total DDI by electron impact on the atomic system, and the total DDI cross section can be expressed by the equation:

$$\sigma^{II} = \sigma^{TS1} + \sigma^{TS2}. \tag{47}$$
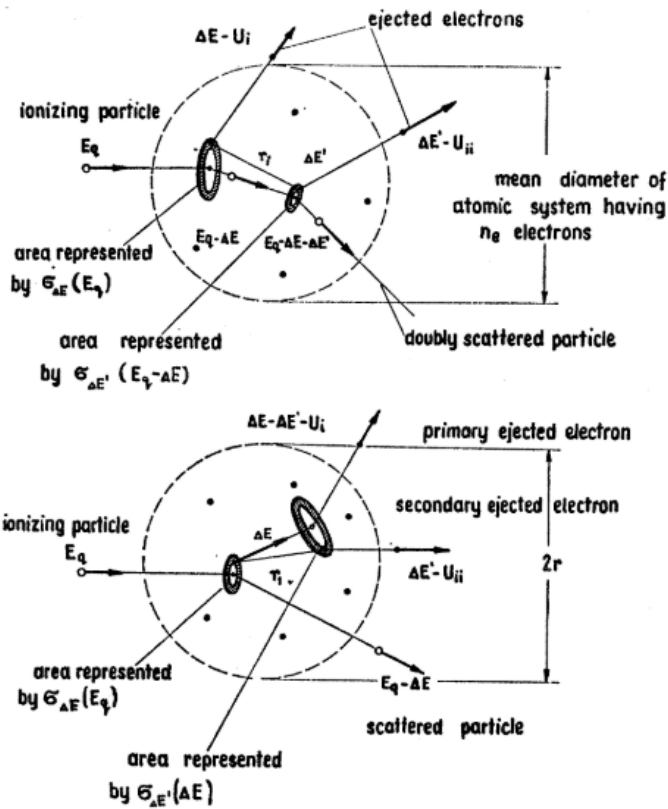
Figure 1. Classical binary encounter model of DDI [83]

The classical model treats DI as an outcome of binary interactions between the incident electron and the target electrons of an atomic system. However, this perspective does not align with the real-world DI process. In reality, the interactions between the incident electron and the two electrons targeted for removal are not isolated binary events. These interactions are influenced by the presence of other atomic electrons, and multiple other processes involving atomic electrons that can come into play during ionization. Consequently, this simplified approach often fails to achieve accurate agreement with experimental observations, and this failure can be attributed to various factors, as evidenced by prior research studies [84–88].

3.7.2. Multi-Step Approach for Electron-Impact Direct Double Ionization

In this work, a multi-step approach [44] is employed to investigate electron-impact DDI cross sections. This approach is based on the classical model of Gryziński but extends its scope by incorporating additional three-step processes to provide a more comprehensive description of the outcomes in electron-ion collisions. Another improvement is the utilization of electron-impact CI and CE cross sections, which are calculated using the DW approach, in the study of the DI process. It is important to note that electron-impact excitation and ionization cross sections used in the multi-step approach can be obtained using any available approximation. This enhances the flexibility of this approach.

While the classical model [83] presented previously considers only two sequential II processes in the study of DDI, the multi-step method expands this analysis by accounting for the possibility of additional three-step processes. This method incorporates both excitation and ionization processes that may occur during electron-ion encounters and describes DDI as a sum of the following processes:

- two sequential ionization processes (II);

- initial ionization process with subsequent excitation, followed by second ionization process (IEI);

- initial excitation process with two subsequent ionization processes (EII).

The equation for the DDI process from the level i to the level f through the II path (DDI(II)), which involves two sequential CI processes, can be written as

$$\sigma_{if}^{\text{DDI(II)}}(\varepsilon) = \sum_j \sigma_{ij}^{\text{CI}}(\varepsilon) \int_{E_{jf}}^{\varepsilon - E_{ij}} \rho_{ij}(\varepsilon, \varepsilon_1) \frac{\sigma_{jf}^{\text{CI}}(\varepsilon_1)}{4\pi \bar{R}_{nl}^2} d\varepsilon_1, \qquad (48)$$

here, E_{ij} is a transition energy, ε_1 is an energy of the scattered or ejected electron. One of these electrons in the further step collides with one of the remaining bound electrons from the nl subshell and ejects it. The energy distribution $\rho_{ij}(\varepsilon, \varepsilon_1)$ is normalized to unity: $\int_0^{\varepsilon - E_{ij}} \rho_{ij}(\varepsilon, \varepsilon_1) d\varepsilon_1 = 1$. A

probability of the second electron-impact ionization process is represented by a factor $\int_{E_{jf}}^{\varepsilon-E_{ij}} \rho_{ij}(\varepsilon,\varepsilon_1)\frac{\sigma_{jf}^{\text{CI}}(\varepsilon_1)}{4\pi\bar{R}_{nl}^2}d\varepsilon_1$; the factor $\frac{\sigma_{jf}^{\text{CI}}(\varepsilon_1)}{4\pi\bar{R}_{nl}^2}$ represents the probability of the ionization process by the electron with the energy ε_1. Term $\bar{R}_{nl}$ describes the mean distance of the electrons from the nucleus.

The distribution of the excess energy between the scattered and ejected electrons from the first ionization process is estimated by using the differential cross sections obtained from the binary-encounter-dipole model (BED) [68]. This approach was implemented to study multiple Auger transitions [89–91] and ionization by electron impact [92].

Another possible path leading to DDI is the EII process, which involves electron-impact excitation followed by two sequential CI. Cross sections of DDI process through the EII path (DDI(EII)) can be expressed by the equation

$$
\sigma_{if}^{\text{DDI(EII)}}(\varepsilon) = \sum_{jk} \sigma_{ij}^{\text{CE}}(\varepsilon)\frac{\sigma_{jk}^{\text{CI}}(\varepsilon-E_{ij})}{4\pi\bar{R}_{nl}^2}
$$
$$
\int_{E_{kf}}^{\varepsilon-E_{ij}-E_{jk}} \rho_{jk}(\varepsilon-E_{ij},\varepsilon_1)\frac{\sigma_{kf}^{\text{CI}}(\varepsilon_1)}{4\pi\bar{R}_{n'l'}^2}d\varepsilon_1. \tag{49}
$$

Another three-step process, through which DDI can occur, is the IEI path. This path involves CI followed by an excitation with subsequent ionization. Cross sections of DDI process through the IEI path (DDI(IEI)) are written as

$$
\sigma_{if}^{\text{DDI(IEI)}}(\varepsilon) = \sum_{jk} \sigma_{ij}^{\text{CI}}(\varepsilon)
$$
$$
\int_{E_{jk}}^{\varepsilon-E_{ij}} \rho_{ij}(\varepsilon,\varepsilon_1)\frac{\sigma_{jk}^{\text{CE}}(\varepsilon_1)}{4\pi\bar{R}_{nl}^2}\frac{\sigma_{kf}^{\text{CI}}(\varepsilon_1-E_{jk})}{4\pi\bar{R}_{n'l'}^2}d\varepsilon_1, \tag{50}
$$

here, $\frac{\sigma_{kj}^{\text{CE}}(\varepsilon_1)}{4\pi\bar{R}_{nl}^2}$ is the excitation probability of electron from the nl subshell of the level k to the level j by the scattered or ejected electron with energy ε_1.

A simpler expressions of DDI(II), DDI(EII), and DDI(IEI) are also possible by considering two limiting cases of the energy distribution of the scattered and ejected electrons:

- scattered and ejected electrons share the excess energy (DDI1),

- one of the electrons takes all the available energy (DDI2).

Taking this simplification into account, the equations for DDI(II), DDI(EII), and DDI(IEI) can be expressed as follows:

$$\sigma_{if}^{DDI(II)}(\varepsilon) = \sum_j \sigma_{ij}^{CI}(\varepsilon) \frac{\sigma_{jf}^{CI}(\varepsilon_1)}{4\pi \bar{R}_{nl}^2},$$ (51)

$$\sigma_{if}^{DDI(EII)}(\varepsilon) = \sum_{kj} \sigma_{ik}^{CE}(\varepsilon) \frac{\sigma_{kj}^{CI}(\varepsilon_1)}{4\pi \bar{R}_{nl}^2} \frac{\sigma_{jf}^{CI}(\varepsilon_2)}{4\pi \bar{R}_{n'l'}^2},$$ (52)

$$\sigma_{if}^{DDI(IEI)}(\varepsilon) = \sum_{kj} \sigma_{ik}^{CI}(\varepsilon) \frac{\sigma_{kj}^{CE}(\varepsilon_1)}{4\pi \bar{R}_{nl}^2} \frac{\sigma_{jf}^{CI}(\varepsilon_2)}{4\pi \bar{R}_{n'l'}^2}.$$ (53)

Previous studies, which considered two limiting cases of the energy distribution for the scattered and ejected electrons during sequential DDI process, demonstrated that a better agreement with measurements at higher energies of the incident electron in the DDI process for the light ions Li$^+$ [93], O$^+$, O^{2+}, O^{3+}, C^{1+}, and Ar^{2+} [44] was obtained when it was assumed that after the initial SI process the scattered and ejected electrons share the excess energy equally. However, it has also been shown that mainly one of the electrons takes all the excess energy and participates in the further processes at the lower energies of the incident electron.

3.7.3. Indirect Double Ionization

The IDI processes correspond to IA, excitation and double AI as well as RETA:

$$\sigma_{if}^{IDI}(\varepsilon) = \sigma_{if}^{IA}(\varepsilon) + \sigma_{if}^{EDA}(\varepsilon) + \sigma_{if}^{RETA}(\varepsilon).$$ (54)

The IA process is initiated by electron-impact ionization from the level i to the intermediate level j:

$$\sigma_{if}^{IA}(\varepsilon) = \sum_j \sigma_{ij}^{CI}(\varepsilon) B_{jf}^a,$$ (55)

here, branching ratio B_{jf}^a is described by the Eq. (37).

The cross sections produced by the EDA process are given by

$$\sigma_{if}^{\mathrm{EDA}}(\varepsilon) = \sum_{jm} \sigma_{ij}^{\mathrm{CE}}(\varepsilon) B_{jm}^a B_{mf}^a, \tag{56}$$

where summation is performed over the autoionizing levels j of the initial ion and the autoionizing levels m of the singly ionized ion.

The RETA process starts with capture of the incident electron by the atomic system and promotion of the bound shell electron to the higher shell. The formed autoionizing state of the initial ion decays through radiative and Auger cascades leading to ions in various ionization stages. The decay which ends in the removal of two electrons of the initial ion contributes to the DI. The cross sections for the RETA process are expressed by the equation:

$$\sigma_{if}^{\mathrm{RETA}}(\varepsilon) = \sum_{lkj} \sigma_{il}^{\mathrm{DC}}(\varepsilon) B_{lk}^a B_{kj}^a B_{jf}^a, \tag{57}$$

where summation is performed over the autoionizing levels l of the initial ion, the levels k of doubly ionized ion, and the levels j of the triply ionized ion. $\sigma_{il}^{\mathrm{DC}}(\varepsilon)$ is the cross section of the DC process (Eq. (39)).

In addition to previously described IDI process, other indirect processes are introduced for DI. These processes include:

- ionization-excitation followed by an autoionization (IE-AI) and

- excitation-ionization with subsequent autoionization (EI-AI).

Equation of the DI process through the IE-AI path can be written as

$$\sigma_{if}^{\mathrm{DI(IE-AI)}}(\varepsilon) = \sum_{jk} \sigma_{ij}^{\mathrm{CI}}(\varepsilon) \int_{E_{jk}}^{\varepsilon - E_{ij}} \rho_{ij}(\varepsilon, \varepsilon_1) \frac{\sigma_{jk}^{\mathrm{CE}}(\varepsilon_1)}{4\pi \bar{R}_{nl}^2} d\varepsilon_1 B_{kf}^a. \tag{58}$$

Similarly, equation of the DI process through the EI-AI path can be written as

$$\sigma_{if}^{\mathrm{DI(EI-AI)}}(\varepsilon) = \sum_{jk} \sigma_{ij}^{\mathrm{CE}}(\varepsilon) \frac{\sigma_{jk}^{\mathrm{CI}}(\varepsilon - E_{ij})}{4\pi \bar{R}_{nl}^2} d\varepsilon_1 B_{kf}^a. \tag{59}$$

3.8. Electron-Impact Triple Ionization

Electron impact TI is one of the multiple ionization processes in which an atom or ion lose three electrons during a collision with an impacting electron. In this study, the electron-impact TI process is investigated, with a focus on the various pathways it can follow.

When the energy of an excited level resulting from the DDI process exceeds the TI threshold, it can undergo further decay through AI, leading to what is referred to as DDI-AI. This AI following DDI ultimately results in TI. Therefore, the investigation of TI encompasses following processes:

- direct double ionization process through ionization-ionization path, followed by autoionization (DDI(II)-AI),

- direct double ionization process through ionization-excitation-ionization path, followed by autoionization (DDI(IEI)-AI),

- direct double ionization process through excitation-ionization-ionization path, followed by autoionization (DDI(EII)-AI).

Additionally, the contribution of Auger cascades, which are initiated when inner-shell vacancies are created by the incident electron, must be taken into account. Auger cascades are significant mechanisms for the generation of ions in highly charged stages, a phenomenon that has been well-documented in previous studies [54–56, 94]. Understanding and estimating this Auger cascade contribution is essential for a comprehensive analysis of electron-impact TI. Therefore the electron-impact TI process is examined as the sum of the DDI-AI processes and the Auger cascade that follows SI from the inner shell.

The equations describing the DDI process, encompassing the II, EII, and IEI paths, along with the subsequent AI from the initial ion's level i to the triply ionized ion's level f, can be formulated as:

$$\sigma_{if}^{\mathrm{DDI(II)-AI}}(\varepsilon) = \sum_{j} \sigma_{ij}^{\mathrm{DDI(II)}}(\varepsilon) B_{jf}^{a}, \tag{60}$$

$$\sigma_{if}^{\mathrm{DDI(EII)-AI}}(\varepsilon) = \sum_{j} \sigma_{ij}^{\mathrm{DDI(EII)}}(\varepsilon) B_{jf}^{a}, \tag{61}$$

$$\sigma_{if}^{\mathrm{DDI(IEI)-AI}}(\varepsilon) = \sum_j \sigma_{ij}^{\mathrm{DDI(IEI)}}(\varepsilon) B_{jf}^a. \qquad (62)$$

Here, the description of DDI involves both two and three-step processes, occurring from the initial ion's level i to the doubly ionized ion's level j, as outlined in Eq. (51), (52), and (53). The subsequent AI process following DDI is characterized by the branching ratio B_{jf}^a, which denotes the transition from level j of the doubly ionized ion to the level f of the triply ionized ion, and is presented in Eq. (60), (61), and (62).

4. RESULTS

4.1. Energy Levels and Ionization Thresholds

The behavior of an atomic system under perturbation is revealed by the information provided in the energy level structure of an ion. Additionally, the spectral characteristics of the ion are identified through the energies associated with its electronic configurations. Various pathways through which single and multiple excitation, ionization, and autoionization processes can occur are highlighted by the energy level structure. Furthermore, it allows for the identification of single and multiple ionization thresholds. Therefore, in the following sections, the energy level structures of Se^{2+}, Se^{3+} and B^+ ions will be discussed.

4.1.1. Se^{2+} ion [A1]

Energy levels of the lowest configurations for the Se^{2+}, Se^{3+}, Se^{4+}, Se^{5+}, and Se^{6+} ions as well as SI, DI and TI thresholds for the Se^{2+} ion are presented in Fig. 2. The comparison of calculated threshold energies with National Institute of Standarts and Technology (NIST) data is presented in Table 1.

The SI threshold for the ground state of the Se^{2+} ion corresponds to 31.06 eV which is in good agreement with NIST value of 31.7 eV. Experimental cross sections start below the ground state ionization threshold what suggests that metastable fraction is present in parent ion beam [38]. More significant discrepancies are observed for the calculated DI and TI thresholds, which are underestimated by 1.22 eV and 3.66 eV, respectively.

Our calculated energy levels of the Se^{2+} ground configuration with the values from the NIST database [95] are presented in Table 2. It can be seen that splitting of the theoretical energy levels of the ground configuration is higher than for the NIST data. This demonstrates importance of correlation effects for the presented energy levels.

Figure 2. Energy levels of the lowest configurations of the Se^{2+}, Se^{3+}, Se^{4+}, Se^{5+}, and Se^{6+} ions. Ionization thresholds are presented by horizontal lines with the corresponding values. Energy levels of even configurations are marked in red, while energy levels of odd configurations are marked in blue.

Table 1. Theoretical ionization thresholds (in eV) for the Se^{2+} ion. The NIST recommended values are presented for comparison.

Threshold	FAC	NIST [95]
SI	31.06	31.7
DI	73.42	74.64
TI	139.28	142.94

The information presented in Fig. 2 reveals that excited states of the Se^{3+} ion, characterized by configurations featuring a vacant $3d$ shell, have the potential to undergo Auger transitions leading to the formation of Se^{4+} ions. This is possible due to the fact that the energies of these excited states exceed the DI threshold for Se^{2+}. Additionally, the energies associated with excited states of the Se^{3+} ion, featuring a vacancy in

the $3p$ shell, surpass the TI threshold for Se^{2+}. Consequently, an Auger cascade process could take place from these configurations, resulting in a transition to the Se^{5+} ion. Previous studies on Kr ions have highlighted the significance of correlation effects in Auger cascades [54–56]. Unfortunately, these calculations are computationally intensive and have not been included in the investigation of Se^{2+} ions.

Table 2. Energy levels of the ground $[Ar]\,3d^{10}4s^2 4p^2$ configuration of Se^{2+}. The NIST recommended values are presented for comparison.

Index	Term	J	Energy (eV)	NIST Energy (eV)
0	^3P	0	0.0000	0.000
1	^3P	1	0.2208	0.2159
2	^3P	2	0.5202	0.4881
3	^1D	2	1.9357	1.6158
4	^1S	0	4.2036	3.5249

4.1.2. Se^{3+} ion [A2]

The energy levels corresponding to the main configurations governing DI and TI of the Se^{3+} ion, along with the thresholds for SI, DI, and TI, can be observed in Fig. 3. Calculated SI, DI, and TI threshold energies for the Se^{3+} ion are compared with NIST data in Table 3.

The SI threshold for the ground state of the Se^{3+} ion is 42.35 eV, which is in good agreement with the NIST value of 42.95 eV [95]. The theoretical SI threshold falls within the error bars of the experimental value determined to be 42.2 ± 1.8 eV [39]. The DI threshold corresponds to 108.21 eV, while the NIST-provided value is 111.25 eV. The largest discrepancy between the calculated threshold and the one provided by NIST is observed for the TI. The calculated value is 189.33 eV, which is 3.75 eV below the NIST value of 193.08 eV.
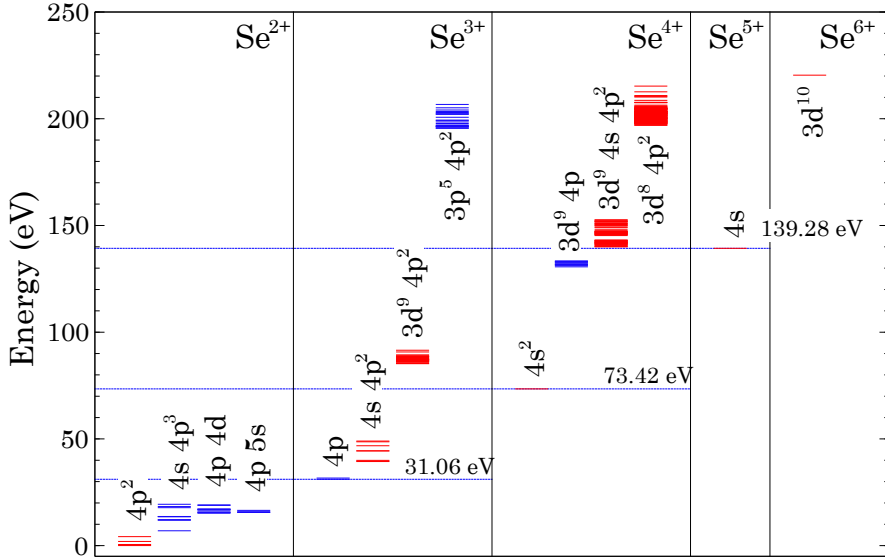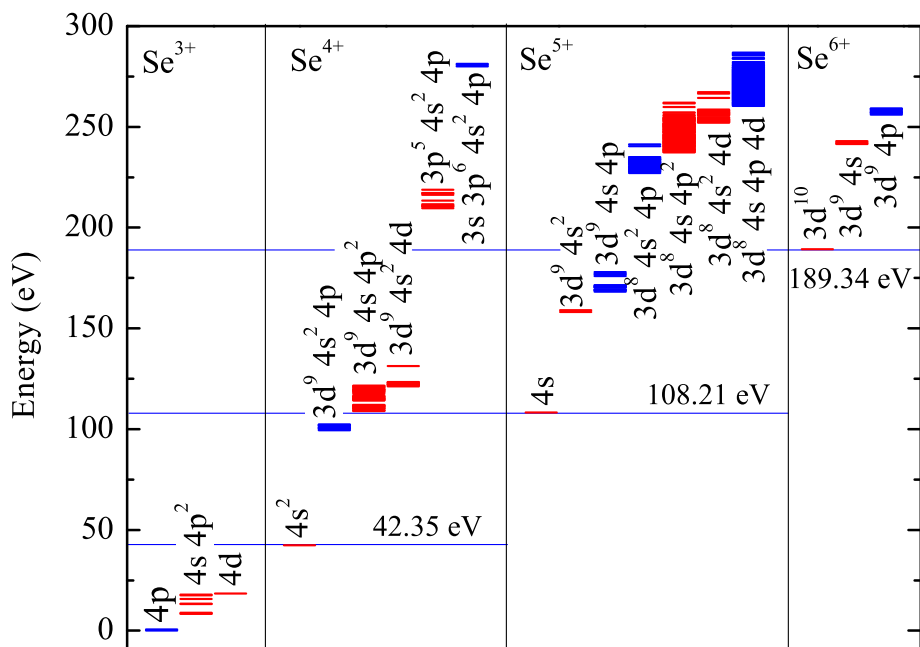
Figure 3. Energy levels of the configurations for the Se^{3+}, Se^{4+}, Se^{5+}, Se^{6+}, and Se^{7+} ions. Ionization thresholds are presented by horizontal lines with the corresponding values. Energy levels of even configurations are marked in red, while energy levels of odd configurations are marked in blue.

As evident from Fig. 3, following the initial ionization process by the incident electron, several excited levels of Se^{4+} ion lie above the TI threshold. Consequently, they can undergo decay through Auger cascades, ultimately leading to the formation of Se^{6+} ion. This highlights the importance of incorporating Auger cascades in the investigation of TI in Se^{3+} ion.

Table 3. Theoretical ionization thresholds (in eV) for the Se^{3+} ion. The NIST recommended values are presented for comparison.

Threshold	FAC	NIST [95]
SI	42.35	42.95
DI	108.21	111.25
TI	189.33	193.08

In case of Se^{5+} ions, several excited levels are created during the DDI and IDI processes of the initial Se^{3+} ion (Fig. 3). Some of these excited levels lie above the TI threshold, making AI possible, which results in the generation of Se^{6+} ion.

4.1.3. B^+ ion [A3]

SI, DI, and TI thresholds for the B^+ ion are compared with the values provided by the NIST [95] in Table 4. It can be observed that the calculated ionization thresholds are slightly lower than the NIST values. The variance between the calculated single-configuration and NIST values ranges from 1.9 eV for the SI threshold to 3.4 eV for the TI threshold. The difference for the DI threshold is approximately 2 eV.

Table 4. Theoretical ionization thresholds (in eV) for the B^+ ion. The NIST recommended values are presented for comparison. FAC1 – single-configuration data, FAC2 – results obtained using configuration interaction method. See text for explanations.

Threshold	FAC1	FAC2	NIST [95]
SI	23.3	24.9	25.2
DI	61.1	62.5	63.1
TI	319.1	320.7	322.5

As per NIST data, the B^+ $2s^2$ $^1S_0$ configuration state function contributes to 93% in the expansion of the intermediate wave function, while the B^+ $2p^2$ $^1S_0$ configuration state function provides a 7% contribution. Consequently, the study of SI, DI, and TI incorporates correlation effects using the configuration interaction method. The ground state of the B^+ ion encompasses interacting configurations such as $2s^2$, $2p^2$, $3l^2$ ($l = 0,1,2$), $2p3p$, and $3s3d$. The inclusion of these correlation effects results in an enhancement of the theoretical ionization thresholds by approximately 1.6 eV compared to the single-configuration data (Table 4).

4.1.4. Conclusions

In this study, ionization thresholds for B^+ and Se^{2+} as well as Se^{3+} ions were analyzed in comparison to NIST data. Slight discrepancies between calculated thresholds and NIST values were observed, highlighting the significance of incorporating correlation effects. For B^+ ion, correlation effects, mainly stemming from the B^+ $2s^2$ $^1S_0$ and B^+ $2p^2$ $^1S_0$ configurations, contributed significantly. This inclusion elevated the theoretical ionization thresholds by approximately 1.6 eV. The study of the energy level structures for Se^{2+} and Se^{3+} ions highlights the potential for Auger transitions from excited states which are formed during SI and DI ionization processes of the initial ions.

4.2. Electron-Impact Single Ionization

The accuracy of the multi-step approach utilized to compute electron-impact DI and TI cross sections is partially dependent on SI cross sections. Hence, a comprehensive investigation of the SI process has been performed for B^+ and Se^{2+} ions. This study was important to validate that the calculated SI cross sections are in substantial agreement with experimental data, thus ensuring their reliability in accurately representing the distinct stages of the DI and TI processes.

4.2.1. Se^{2+} ion [A1]

The examination of contributions to the SI process (Fig. 4) of Se^{2+} ion originating from various energy levels within the ground configuration of the Se^{2+} ion reveals slightly larger DI cross sections for the highest $4p^2\ {}^1S_0$ level (detailed information about the levels of the ground configurations is provided in Table 2).
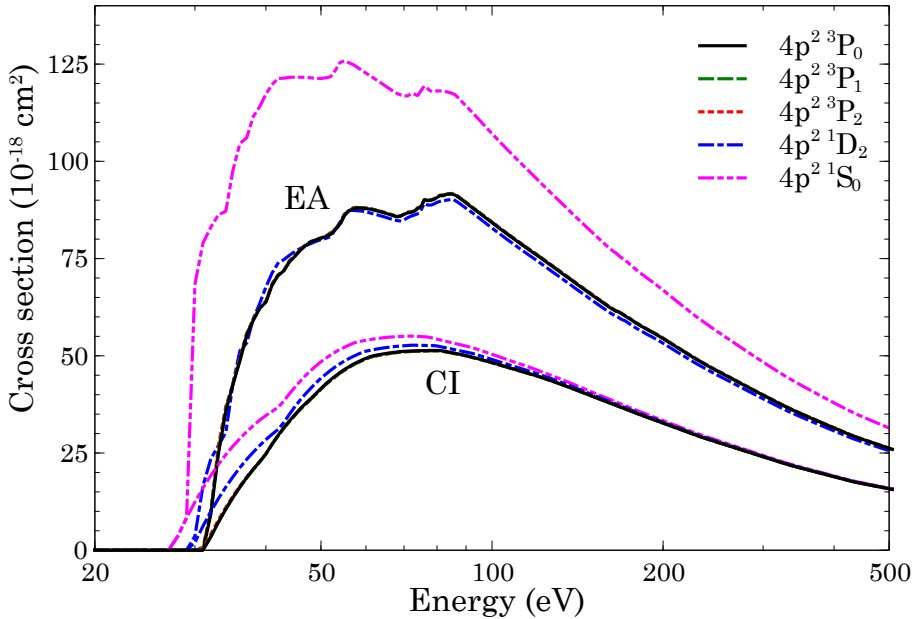
Figure 4. Contributions of the CI and EA processes to SI of Se^{2+} for different energy levels of the ground configuration.

However, the EA process for this level demonstrates a significant increase in cross sections across the entire energy range. As a result, incorporating the contribution of the EA process from the $4p^2\ ^1S_0$ level significantly enhances the agreement with experimental results compared to the contributions from other levels within the ground configuration. Consequently, the investigation turns its focus to investigating the SI, DI, and TI cross sections of the Se^{2+} ion, with specific attention directed towards the $4p^2\ ^1S_0$ level.

The total cross sections of SI by electron-impact for the Se^{2+} ion are compared with experiment in Fig. 5. It is important to highlight that the impact of radiative damping is of minimal significance. Total SI cross sections are in good agreement with experiment across the entire energy range of the incident electron.

Figure 5. Electron-impact SI of Se^{2+} for the $4p^2\ ^1S_0$ level. Short-dashed line (red): CI of $4p$ shell; long-dashed line (green): CI of $4p$ and $4s$ shells; solid line (black): CI with EA; empty circles: experiment [38]. Calculated contributions of the CI and EA processes are represented by the differently shaded (colored) areas.

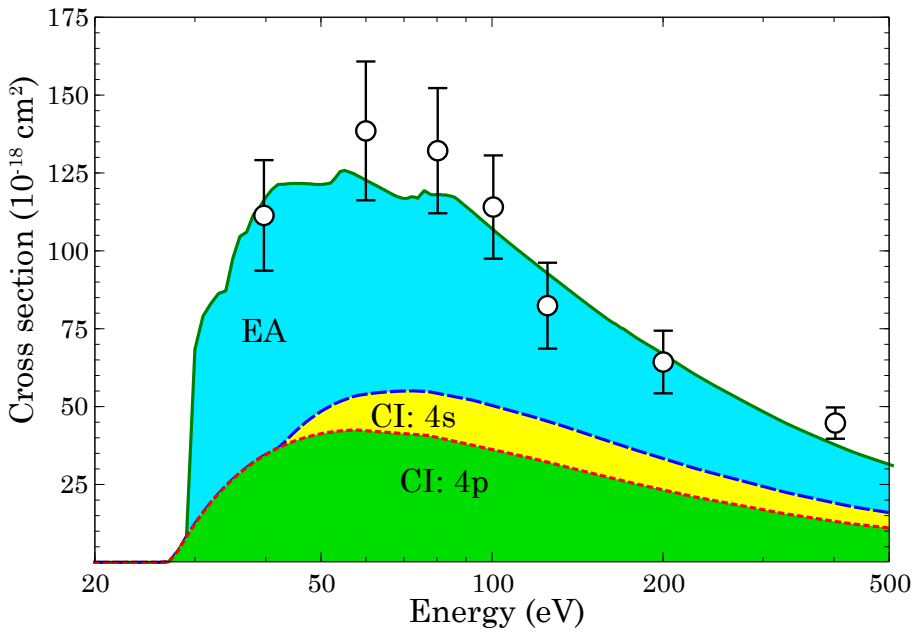Notably, the dominant contribution to the total SI cross sections arises from excitations leading to configurations within the Se^{2+} ion, subsequently followed by AI to the Se^{3+} ion. Furthermore, it is noteworthy that the contribution originating from direct ionization of the $4p$ shell substantially surpasses that of the $4s$ shell.

The most significant contributions to the EA process from the ground level originate from transitions such as $4s \rightarrow 4d$, $4s \rightarrow 5d$, $3d \rightarrow 4p$, $3d \rightarrow 4d$, $4s \rightarrow 5s$, and $4s \rightarrow 6s$ (Fig. 6). The individual contributions from other excitations are considerably smaller.

Figure 6. Contributions of various EA channels to the total EA cross sections for the ground $4p^2\ ^3P_0$ level. The strongest EA channels are represented by the differently shaded (colored) areas.

Surprisingly, the cross sections for distinct EA channels undergo significant changes for the excited $4p^2\ ^1S_0$ level (Fig. 7). First of all, the contribution from the $4s \rightarrow 4d$ excitation increases about by a factor of four compared to excitation from the ground level. This amounts to about 35% at the peak of the EA cross sections. Second, the next strongest contributions correspond to the $4s \rightarrow 5s$, $4s \rightarrow 5p$, $4s \rightarrow 5d$, $3d \rightarrow 4p$, and $4s \rightarrow 4d$ excitations which are presented in decreasing

order of the strength. Furthermore, these excitations produce much larger contribution to the EA cross sections compared to excitation from the ground level.
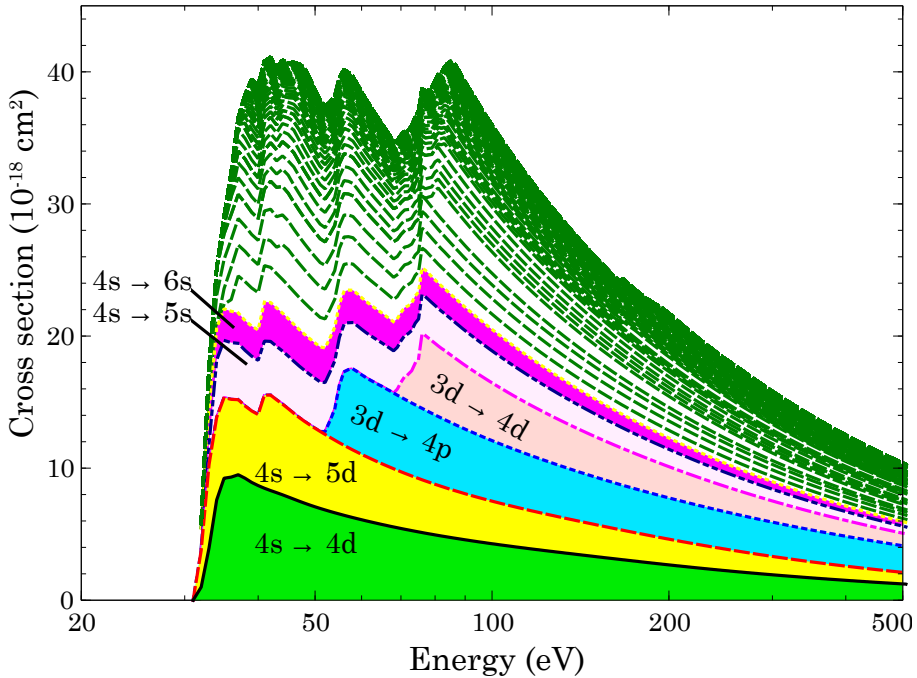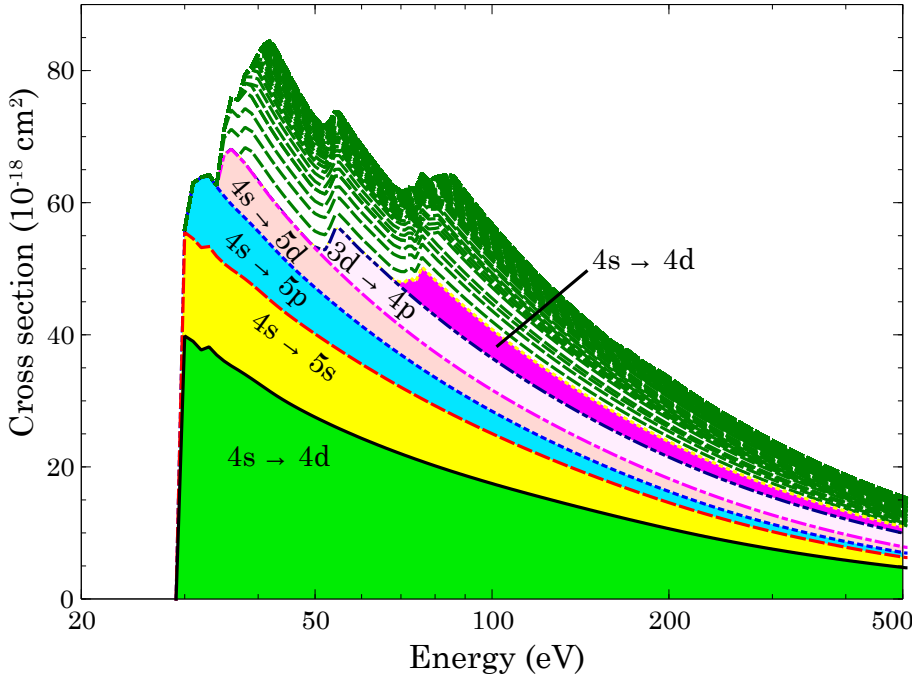

Figure 7. Contributions of various EA channels to the total EA cross sections for the $4p^2\ ^1S_0$ level. The strongest EA channels are represented by the differently shaded (colored) areas.

4.2.2. B⁺ ion [A3]

In the theoretical calculations of electron-impact SI cross sections for B⁺ ion, which results are depicted in Fig. 8, the wave function of the incident electron, describing its behavior before the collision, and the wave function of the scattered electron, representing its behavior after the collision, are evaluated in the potentials of ionizing and ionized ions. This analysis aims to determine which potential yields a better agreement with empirical data.

In this analysis the data for the ground state $2s^2\ ^1S_0$ and the long-lived $2s2p\ ^3P_0$ level are presented. Theoretical cross sections are then compared with experimental measurements from the reference [25]. It

is important to note that the experimental cross sections correspond to a 9% contribution from the long-lived levels of the $2s2p$ configuration and a 91% contribution from the ground state.

The electron-impact ionization cross sections for the long-lived $2s2p$ $^3P_2$ level exhibit close agreement with the data obtained for the $2s2p$ $^3P_0$ and $2s2p$ $^3P_1$ levels. Consequently, these particular cross sections are omitted from the present discussion.

Figure 8. Electron-impact SI cross sections for the ground $2s^2$ $^1S_0$ (green) and long-lived $2s2p$ $^3P_0$ (blue) levels of the B^+ ion. Solid and dot-dashed lines correspond to results obtained in the potential of the ionizing ion, dashed and dotted lines represent a study of the direct process in the potential of the ionized ion. Yellow circles with error bars: experiment for 9% of metastable fraction in the ion beam [25]

.

The SI cross sections exhibit higher values for both the ground and long-lived levels when the continuum orbitals of both incident and scattered electrons are evaluated within the potential of the ionizing ion, as compared to the potential of the ionized ion (Fig. 8).

In the case of the ground level, the theoretical cross sections com-

puted using the potential of the ionizing ion demonstrate good agreement with experimental results [25] near and slightly above the SI threshold energies. However, these theoretical values are slightly elevated both near and at the peak value of the cross sections when compared to the experimental data. It is reasonable to expect a certain level of disparity, considering that the experimental cross sections encompass a 9% contribution from the long-lived levels, as emphasized in the reference [25].

On the contrary, the theoretical cross sections computed within the potential of the ionized ion consistently show an underestimation of the experimental values across the entire spectrum of incident energies. In contrast, for the excited configuration levels in both examined potentials, the theoretical cross sections notably exhibit an overestimation of the experimental data across the complete range of energies (Fig. 8).

It's worth highlighting that the influence of correlation effects on the SI cross sections is relatively modest, resulting in a decrease of around 2% only. However, it's important to note that in the case of other ions, the correlation effects wielded a significant influence on the SI cross sections [96]. The obtained results also show that the contribution from indirect processes of SI is significantly lower, exhibiting a difference of two orders of magnitude when compared to the total SI cross sections.

The scaled SI cross sections for the ground and long-lived levels of the B^+ ion are compared with experimental ones [25] in Fig. 9. Observing the results, it becomes evident that the scaled DW cross sections calculated for the ground $2s^2\,^1S_0$ level in the potential of the ionizing ion consistently remain below the measured values across the entirety of the energy spectrum. It's important to highlight that the cross sections computed using the potential of the ionized ion exhibit a strong underestimation of the experimental data and are therefore excluded from presentation here.

For the long-lived $2s2p\,^3P_0$ level, the theoretical scaled cross sections computed within the potential of the ionizing ion notably overestimate the experimental values across the entire range of energies. However, when considering the theoretical cross sections that correspond to a 9% fraction of the long-lived levels within the ion beam, a reasonable agreement with experimental measurements is observed (Fig. 9).
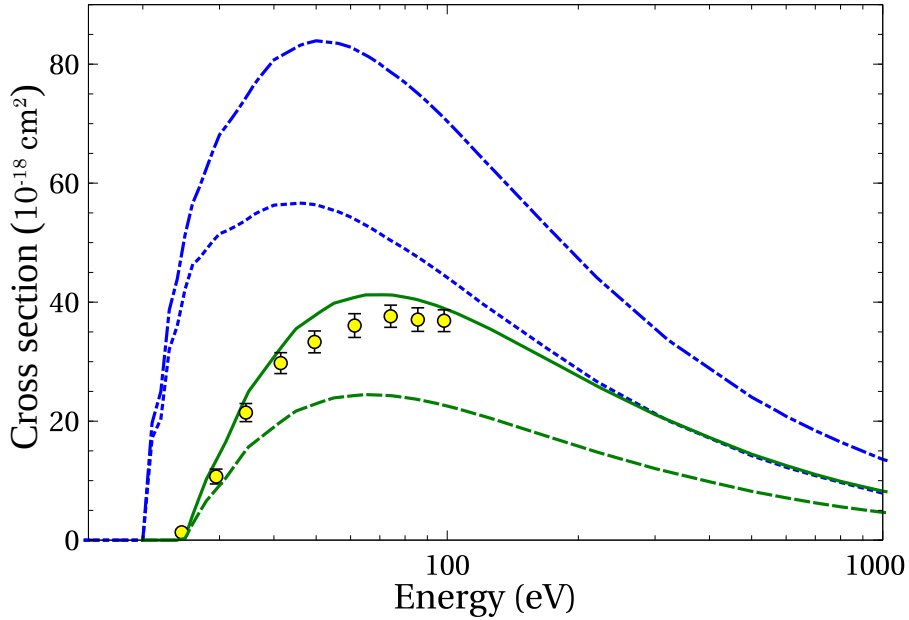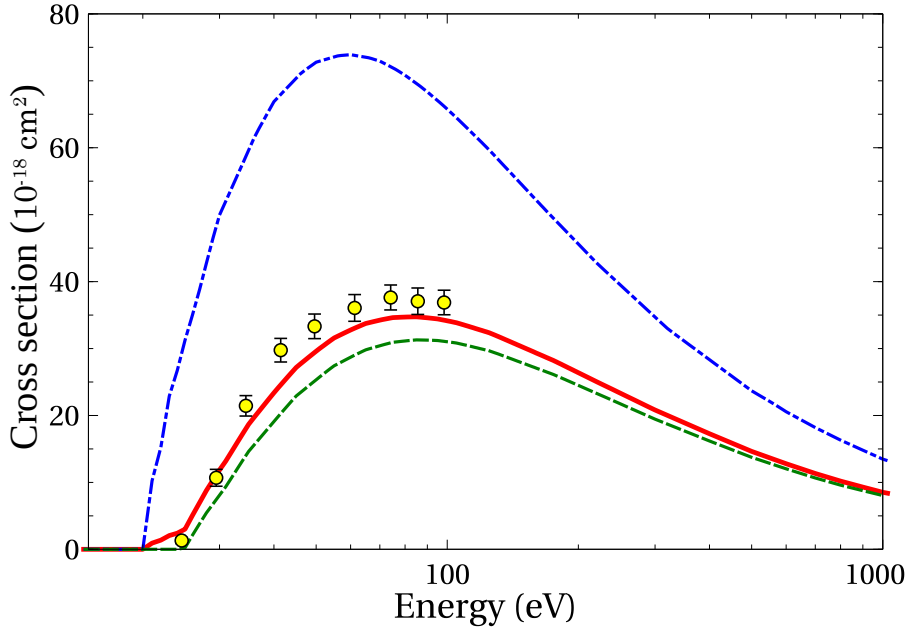
Figure 9. The scaled electron-impact SI cross sections for the ground $2s^2$ $^1S_0$ (green dashed) and long-lived $2s2p\ ^3P_0$ (blue dot-dashed) levels of B^+ ion. Solid line (red) represents the scaled DW cross sections with contribution of 91% from the ground level and 9% from the long-lived one. Yellow circles with error bars: experiment for 9% of metastable fraction in the ion beam [25].

4.2.3. Conclusions

For Se^{2+} it is demonstrated that the main part of ions in the parent beam exists in the excited $4p^2\ ^1S_0$ level of the ground configuration. A good agreement between our calculations and experimental measurements is found for the SI of the Se^{2+} ion across the entire energy range of incident electron with the largest contribution originating from the EA process.

For the B^+ ion a good agreement with experimental SI results is achieved for the study in the potential of the ionizing ion utilizing scaled DW cross sections. This investigation incorporates correlation effects for the ground configuration, along with scaled DW cross sections applied to electron-impact excitation and ionization processes.

4.3. Electron-Impact Double Ionization

4.3.1. Se²⁺ ion [A1]

For the Se^{2+} ion, the indirect process of DI involves ionization from the $3d$ subshell followed by AI:

$$3d^{10}4p^2 + e^- \rightarrow 3d^9 4p^2 + 2e^- \rightarrow 3d^9 + 3e^- \tag{63}$$
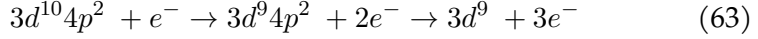
For the $4p$ subshell of the Se^{2+} ion, the DDI II process is defined by the sequential CI:

$$3d^{10}4p^2 + e^- \rightarrow 3d^{10}4p + 2e^- \Rightarrow 3d^{10} + 3e^- \tag{64}$$
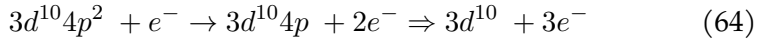
The ionization or excitation by the scattered or ejected electrons is indicated by the $\Rightarrow$ symbol. The DDI EII process involves CE with sequential CI of the valence subshells:

$$3d^{10}4p^2 + e^- \rightarrow 3d^{10}4p\, nl + e^- \Rightarrow \begin{cases} 3d^{10}4p \\ 3d^{10}\, nl \end{cases} + 2e^- \Rightarrow 3d^{10} + 3e^-, \tag{65}$$
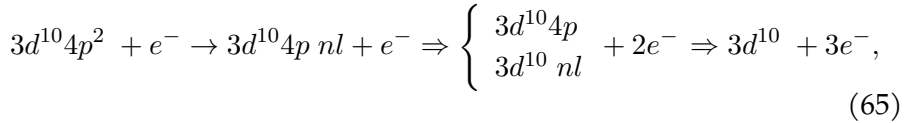
where $n \leqslant 10, l < n$, and $l \leqslant 5$. The DDI IEI process can be schematically represented as:

$$3d^{10}4p^2 + e^- \rightarrow 3d^{10}4p + 2e^- \Rightarrow 3d^{10}\, nl + 2e^- \Rightarrow 3d^{10} + 3e^- \tag{66}$$
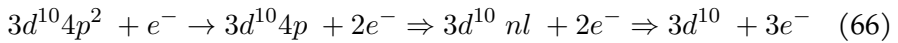
Electron-impact DI cross sections for the Se^{2+} ion are depicted in Fig. 10. As previously mentioned, the focus of this study is on DI from the excited $4p^2\ {}^1S_0$ level. However, similar results are observed for other levels within the ground configuration.

Cross sections of DDI-AI (II, EII, IEI) processes originating from the direct SI of the $3d$ electron contribute to TI, therefore these cross sections are subtracted from the IA values. As evident from Fig. 10, the primary contribution to the overall DI cross sections emerges from the IDI process, involving CI from the $3d$ shell with subsequent AI. The contribution from the direct ionization process constitutes approximately 10%.
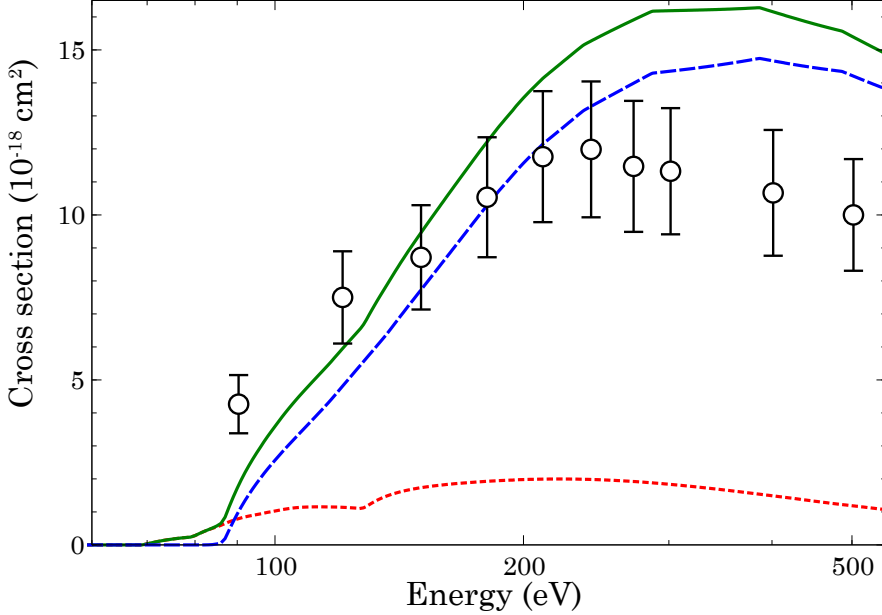
Figure 10. Electron-impact DI of Se^{2+}. Dotted line (red): DDI cross sections when one of the electrons takes all excess energy; dashed line (blue): indirect DI cross sections; solid line (green): total DI cross sections; hollow circles: experiment [38].

Total DI cross sections exhibit good agreement with experimental values near the peak of the experimental cross sections. However, at lower energies, theoretical cross sections underestimate the experimental results. On the other hand, at energies beyond the peak, theoretical cross sections strongly overestimate the experimental ones. These discrepancies align with those obtained using the CADW method [42].

In this study, the influence of correlation effects on the cross sections of the DI process was also investigated. The admixed configurations that exert the most significant influence on the ground configurations of Se^{2+} and Se^{3+} ions, as well as the Se^{3+} $3d^9 4s^2 4p^2$ configuration, were identified using CIS.

Unfortunately, this study has shown that even with the extension of the basis of interacting configurations, the correlation effects do not appear to significantly contribute to the cross sections of the DI process. Consequently, the reason for the discrepancy between theoretical and

experimental values remains unclear.

4.3.2. Se^{3+} ion [A2]

In the case of the Se^{3+} ion, the indirect DI process consists of ionization from the $3p$ subshell followed by AI:

$$3p^6 3d^{10} 4p + e^- \rightarrow 3p^5 3d^{10} 4p + 2e^- \rightarrow 3p^6 3d^{10} + 3e^- \qquad (67)$$
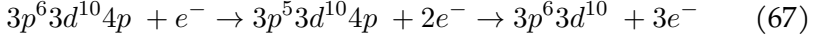
For the $4p$ subshell of the Se^{3+} ion, the DDI II process is characterized by sequential CI:

$$3d^{10} 4p + e^- \rightarrow 3d^{10} + 2e^- \Rightarrow 3d^9 + 3e^- \qquad (68)$$
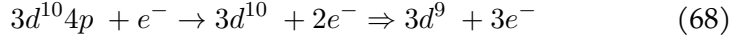
The DDI EII process is associated with CE through sequential CI of the valence subshells:

$$3d^{10} 4p + e^- \rightarrow 3d^9 4p \, nl + e^- \Rightarrow \begin{cases} 3d^9 4p \\ 3d^9 \, nl \end{cases} + 2e^- \Rightarrow 3d^9 + 3e^-, \quad (69)$$
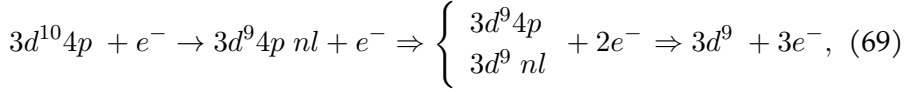
here, $n \leqslant 10$, $l < n$, and $l \leqslant 5$. The DDI IEI process can be depicted schematically as

$$3d^{10} 4p + e^- \rightarrow 3d^{10} + 2e^- \Rightarrow 3d^9 \, nl + 2e^- \Rightarrow 3d^9 + 3e^- \qquad (70)$$
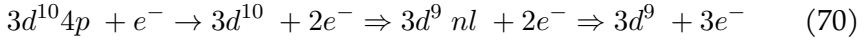
The contributions of different processes to the DI of the Se^{3+} ion are presented in Fig. 11. All calculations are based on data obtained using the single configuration approach.

As evident from the Fig. 11, the dominant process at the peak of the DI cross sections is the DDI process. To illustrate the influence of the DDI-AI process, the DDI contribution remains uncorrected for the possible decay of populated levels in Se^{5+} through Auger transitions to the Se^{6+} ion. It's worth noting that the study includes both two- and three-step processes. Previously, only the two-step process for DI of Se^{3+} was analyzed using the CADW approach [42].

At higher incident electron energies (Fig. 11), the most significant influence on the DI cross sections is observed from ionization of the $3p$ shell, followed by AI. After initial ionization process, the decay of the resulting $3p^5 3d^{10} 4s^2 4p$ configuration leads only to the formation of

Se^{5+} ions. This specific process was previously examined using the CADW approach [42], and our calculated values slightly deviate from the CADW results. Specifically, at the peak, our cross section reaches $1.44\times10^{-18}cm^2$, while CADW yields approximately $1.54\times10^{-18}cm^2$ [42].
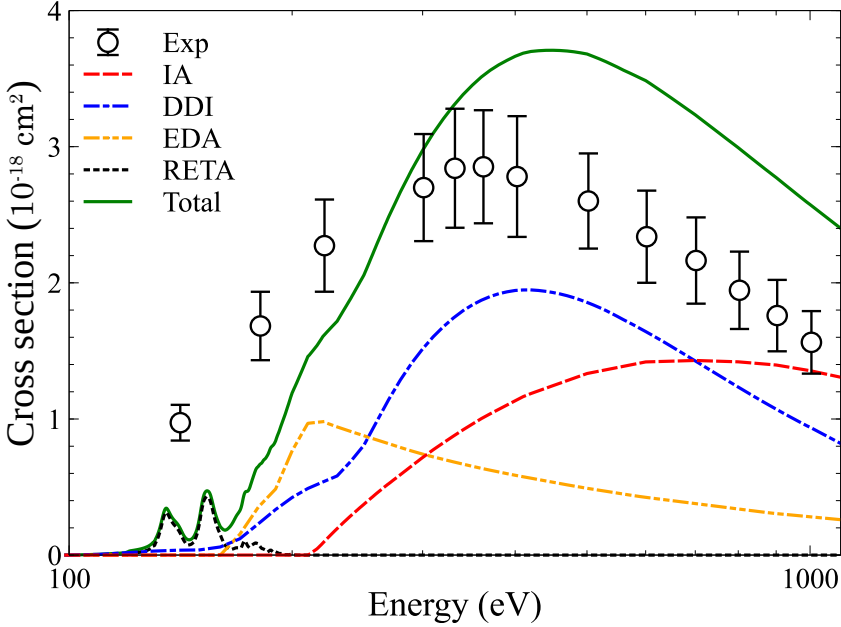
Figure 11. Electron-impact DI cross sections for the Se^{3+} ion. Dashed line (red): IA for ionization from the $3p$ shell; dashed-dotted line (blue): DDI without DDI-AI influence; dashed-dotted-dotted line (orange): EDA for excitation from the $3p$ shell; dotted line (black): RETA for the $3p$ shell excitation (convoluted with 1 eV FWHM Gaussians); solid line (green): total DI; empty circles: experiment [39].

Similar trends have been observed for other ions as well [97–99]. These differences may be attributed to the fact that continuum orbitals of the incident and scattered electrons are investigated in the potential of the ionizing ion, while the ejected electrons are determined in the potential of the ionized ion for the CADW data [42]. Our CI investigation, on the other hand, is performed in the potential of the ionized ion. Detailed IA cross sections are provided in Table 5.

A significant contribution of EDA process to the DI cross sections is observed from excitations of the $3p$ shell up to shells with principal

quantum numbers $n \leqslant 15$ and orbital quantum numbers $l \leqslant 5$. These produced configurations subsequently decay through Auger cascade processes. The contribution of excitations from the $3p$ shell to shells with the principal quantum number $n = 4$ amounts to approximately 50% of the total value of the process. It is worth noting that the influence of this process on the DI cross sections of Se^{3+} had not been studied previously. As depicted in Fig. 11, this process contributes about 0.5×10^{-18}cm^2 to the total DI cross sections at their peak value. Detailed cross sections of EDA process are listed in Table 6.

Table 5. IA cross sections (σ in 10^{-18}cm^2) for the $3p$ shell of Se^{3+} ion. Correlation effects are included in calculations. ε - electron energy in eV, $a \pm b = a \times 10^{\pm b}$.

ε	σ	ε	σ	ε	σ	ε	σ
1.2+2	0.01	7.0+2	130.27	6.1+4	5.58	7.4+4	4.71
1.9+2	0.30	8.0+2	128.34	6.2+4	5.50	7.6+4	4.59
2.1+2	1.51	1.0+3	122.31	6.3+4	5.43	7.8+4	4.48
2.2+2	11.48	2.0+3	90.63	6.4+4	5.36	8.0+4	4.36
2.5+2	37.00	3.0+3	71.25	6.5+4	5.29	8.2+4	4.25
3.5+2	87.66	5.0+3	46.83	6.6+4	5.22	8.4+4	4.14
4.1+2	105.71	9.0+3	29.59	6.7+4	5.16	8.6+4	4.04
5.1+2	122.31	1.3+4	22.00	6.8+4	5.09	1.0+5	3.36
5.6+2	125.92	2.3+4	13.17	7.0+4	4.96	4.0+5	0.87
6.0+2	128.44	4.1+4	7.95	7.2+4	4.83	6.0+5	0.53

Another process which contributes to the total DI cross sections is RETA. The cross sections of this process are detailed in Table 7. As it can be seen from this Table, the RETA process reaches maximum value of 42.36×10^{-18}cm^2 at 153 eV energy, thus contributing the main part to DI cross sections at the lower end of energies (see also Fig. 11). As depicted in Fig. 11, the theoretical DI cross sections are notably lower than the experimental values at lower incident electron energies, while the experimental data tend to be overestimated at higher energies. Here it's important to note that the presented DDI cross sections do not account for the potential decay of populated levels to the next ionization stage through Auger transitions. Therefore in addition to the three aforementioned DDI processes, we have also estimated the contribution

of DDI with subsequent Auger cascade leading to the formation of Se^{5+} ion. This implies the study of triple-autoionization in this case. The impact of this process on electron-impact DI cross sections for the Se^{3+} ion had not been investigated previously.

Table 6. EDA cross sections (σ in $10^{-18}cm^2$) for the $3p$ shell of Se^{3+} ion. ε - electron energy, $a \pm b = a \times 10^{\pm b}$.

ε	σ	ε	σ	ε	σ	ε	σ
1.65+2	1.05	2.14+2	98.92	4.60+2	52.54	6.00+3	6.51
1.70+2	15.31	2.18+2	99.15	5.00+2	49.08	1.00+4	4.48
1.82+2	34.96	2.22+2	97.59	6.00+2	42.45	2.20+4	2.23
1.86+2	43.16	2.26+2	96.10	1.00+3	28.13	3.60+4	1.26
1.94+2	61.71	2.42+2	90.64	1.40+3	22.37	4.40+4	1.17
2.02+2	78.48	2.76+2	80.30	1.80+3	19.44	7.60+4	0.93
2.06+2	89.11	3.00+2	74.19	3.00+3	13.48	1.00+5	0.81
2.10+2	96.93	3.40+2	66.82	4.00+3	10.13	5.00+5	0.29

Table 7. RETA cross sections (σ in $10^{-18}cm^2$) of Se^{3+} ion. ε - electron energy, $a \pm b = a \times 10^{\pm b}$.

ε	σ	ε	σ	ε	σ	ε	σ
1.200+2	0.00	1.442+2	8.11	1.585+2	20.46	1.793+2	8.23
1.208+2	1.21	1.448+2	7.66	1.589+2	18.72	1.798+2	7.44
1.216+2	1.37	1.453+2	7.54	1.594+2	17.09	1.802+2	6.88
1.236+2	1.80	1.456+2	7.59	1.598+2	15.54	1.807+2	6.53
1.256+2	2.45	1.460+2	7.82	1.600+2	14.76	1.810+2	6.25
1.273+2	3.36	1.463+2	8.07	1.604+2	13.44	1.816+2	5.40
1.284+2	4.29	1.468+2	8.75	1.610+2	11.10	1.822+2	4.77
1.296+2	6.05	1.470+2	9.15	1.617+2	9.00	1.826+2	4.62
1.304+2	7.01	1.475+2	10.32	1.623+2	7.35	1.831+2	4.34
1.314+2	10.83	1.479+2	11.67	1.628+2	6.53	1.835+2	3.82
1.320+2	13.76	1.484+2	13.35	1.634+2	5.64	1.840+2	3.28
1.327+2	17.51	1.486+2	14.35	1.646+2	4.70	1.846+2	2.83
1.330+2	19.45	1.489+2	15.87	1.657+2	4.36	1.853+2	2.67
1.335+2	23.10	1.491+2	17.15	1.665+2	4.54	1.855+2	2.65

Table 7 – continued from previous page

ε	σ	ε	σ	ε	σ	ε	σ
1.339+2	26.15	1.495+2	20.10	1.674+2	5.02	1.861+2	2.95
1.341+2	27.55	1.497+2	21.79	1.680+2	5.32	1.866+2	3.39
1.346+2	29.80	1.501+2	24.85	1.683+2	5.36	1.871+2	3.63
1.348+2	30.54	1.507+2	30.15	1.694+2	5.30	1.875+2	3.40
1.351+2	31.08	1.511+2	33.92	1.696+2	5.27	1.877+2	3.17
1.354+2	31.11	1.516+2	37.62	1.702+2	5.28	1.882+2	2.54
1.355+2	30.94	1.521+2	39.95	1.707+2	5.58	1.887+2	2.07
1.358+2	30.34	1.525+2	41.48	1.713+2	7.23	1.896+2	1.78
1.361+2	29.29	1.529+2	42.30	1.717+2	8.83	1.898+2	1.83
1.367+2	27.56	1.531+2	42.53	1.726+2	10.34	1.903+2	1.92
1.372+2	25.63	1.534+2	42.63	1.728+2	10.18	1.911+2	1.78
1.375+2	24.77	1.535+2	42.63	1.733+2	9.37	1.924+2	1.19
1.384+2	22.65	1.538+2	42.51	1.739+2	7.49	1.935+2	1.07
1.390+2	21.36	1.540+2	42.32	1.746+2	6.15	1.944+2	0.79
1.401+2	19.32	1.544+2	41.64	1.750+2	5.88	1.954+2	0.44
1.408+2	17.43	1.549+2	40.38	1.756+2	6.28	1.969+2	0.35
1.412+2	16.08	1.553+2	38.49	1.761+2	6.78	1.987+2	0.39
1.419+2	13.87	1.558+2	36.01	1.765+2	7.27	2.000+2	0.27
1.424+2	11.92	1.563+2	32.77	1.774+2	8.10	2.001+2	0.26
1.430+2	10.22	1.568+2	29.48	1.780+2	8.63	2.018+2	0.12
1.433+2	9.53	1.573+2	26.44	1.787+2	8.89	2.040+2	0.01
1.440+2	8.38	1.578+2	23.77	1.789+2	8.78	1.200+3	0.00

Fig. 12 illustrates the contribution of two- and three-step processes to the DDI cross sections. The II path contributes to approximately 57% of the total cross sections when one of the ejected or scattered electrons absorbs all the excess energy after the first ionization process. The most prominent branch of the II process corresponds to sequential ionization from the $3d$ shell, resulting in the Se^{5+} $3d^8 4s^2 4p$ configuration with energy levels above the TI threshold. At the peak of the II cross sections, the population of energy levels for this configuration amounts to 69%. Unfortunately, this configuration cannot undergo Auger transitions to the Se^{6+} $3d^9 4s$ and $3d^9 4p$ configurations because the energy levels of these configurations are higher than those of the $3d^8 4s^2 4p$ configuration.
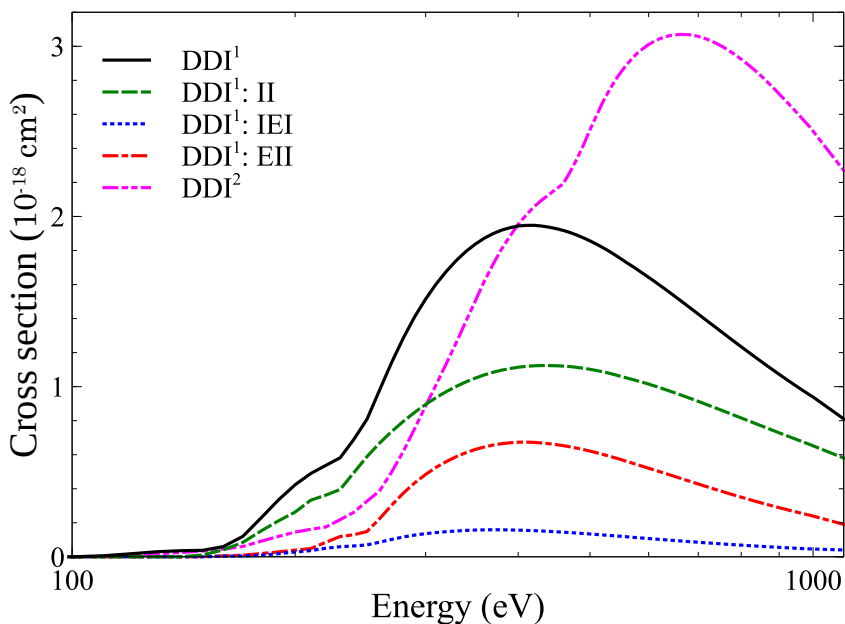
Figure 12. Electron-impact DDI cross sections for the Se^{3+} ion. Dashed line (green): II part of DDI; dashed-dotted line (red): EII part of DDI; dotted line (blue): IEI part of DDI. Superscript 1: DDI cross sections when one of the electrons takes all excess energy in the DDI process; superscript 2: DDI cross sections when scattered and ejected electrons share the excess energy equally.

Other configurations produced by the II process at the peak of the II cross sections include Se^{5+} $3d^9 4s 4p$ (17%), $3d^9 4s^2$ (14%), $3d^{10} 4s$ (0.5%), $3d^{10} 4p$ (0.2%). However, all of these configurations have energy levels below the TI threshold. Therefore, the II process does not contribute to the TI of Se^{3+}.

Surprisingly, the EII process plays a significant role in shaping the DDI cross sections (Fig. 12). It accounts for approximately 34% of the total DDI cross sections at their peak value. The contribution from the IEI process amounts to 8%.

For the scenario where electrons share the excess energy, the DDI cross sections at lower incident electron energies are lower than those obtained when one of the electrons takes all the excess energy (Fig. 12). The situation reverses at higher energies, where the cross sections are higher when the electrons share the excess energy equally. Previous

studies have demonstrated that the scenario where one of the electrons takes all the excess energy provides better agreement with measurements for the DDI cross sections at lower energies [44]. Conversely, better agreement with experimental data at higher energies is achieved when the scattered and ejected electrons equally share the excess energy.

Fig. 13 presents the DDI cross sections when Auger decay of the excited levels of Se^{5+} to the next ionization stage is considered. Contribution of the different DDI processes undergoes significant changes compared to the scenario depicted in Fig. 12. The cross sections produced by the II process account for approximately 91% of the total data. Conversely, the contribution from the EII process drastically decreases as many of the produced excited levels of the Se^{5+} ion decay to Se^{6+}. DDI cross sections with subtracted DDI-AI contribution are detailed in Table 8.
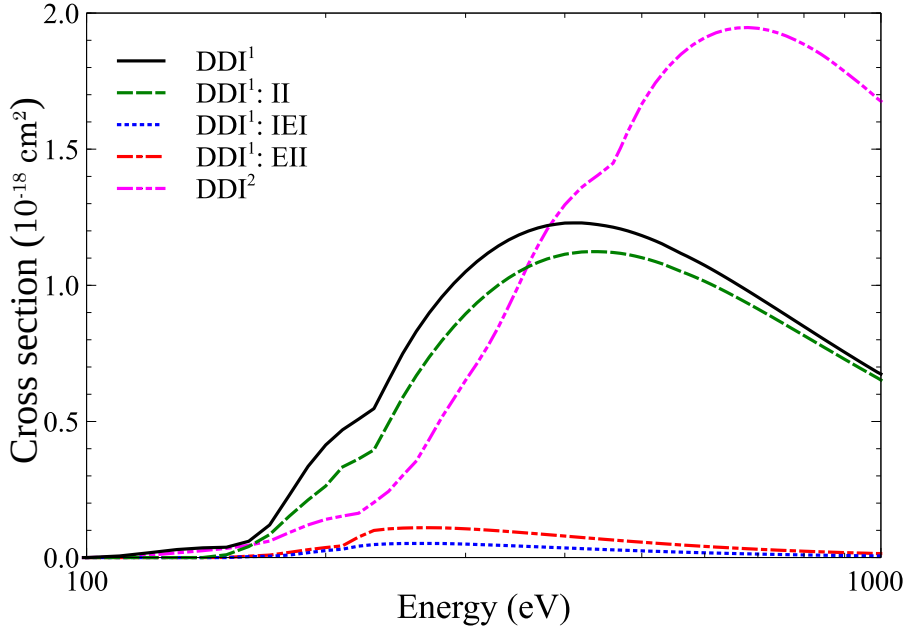
Figure 13. The same as Fig. 12 but diminished due to DDI-AI.

The levels of the $Se^{5+}3d^84s4p^2$ configuration have a relative population of 55% at the peak of the EII cross sections. This configuration is produced by the $4s \rightarrow 4p$ excitation with subsequent double CI from the $3d$ shell. The subsequent decay through the Auger transitions leads to the $Se^{6+}3d^94s$ (54%) and $3d^94p$ (1%). Although there are some levels

of the $3d^84s4p^2$ configuration below the levels of the $3d^94s$ and $3d^94p$ configurations (Fig. 3), the population of these levels is negligible when compared to the population transfer to the next ionization stage.

Table 8. DDI cross sections (σ in 10^{-18}cm^2) of Se^{3+} ion with subtracted DDI-AI contribution . ε - electron energy, $a \pm b = a \times 10^{\pm b}$.

ε	σ	ε	σ	ε	σ	ε	σ
1.1+2	0.59	2.5+2	74.93	5.1+2	117.30	3.0+3	24.50
1.3+2	2.96	2.9+2	100.72	5.5+2	112.89	5.0+3	14.93
1.5+2	3.81	3.1+2	108.71	6.1+2	106.15	7.0+3	10.77
1.6+2	6.00	3.5+2	118.49	6.8+2	97.94	1.0+4	7.72
1.7+2	12.00	3.7+2	121.08	7.9+2	85.88	2.0+4	3.90
1.8+2	22.94	4.0+2	122.85	9.0+2	75.41	3.0+4	2.60
2.0+2	41.36	4.1+2	122.91	9.9+2	68.06	5.0+4	1.56
2.3+2	54.71	4.5+2	121.85	2.0+3	34.99	1.0+5	0.77

Among the configurations produced by the EII process at the peak of the cross sections, the $3d^84s^24d$ configuration has the second-largest population at 22%. The formation of this configuration is determined by the $4p \rightarrow 4d$ excitation, followed by double CI by electron impact from the $3d$ shell. Subsequent Auger transitions from the levels of this configuration populate the $3d^94s$ configuration.

The Se^{4+} $3p^53d^{10}4s^24p$ configuration, generated through electron impact ionization from the $3p$ shell, possesses energy levels ranging from 209.67 to 218.57 eV, which surpasses the TI threshold for Se^{3+}. Auger transitions leading to the $3d^84s^24p$ configuration from the $3p^53d^{10}4s^24p$ configuration are prohibited since the final configuration's energy levels exceed those of the initial configuration. Conversely, the energy levels of the Se^{5+} $3d^94s^2$, $3d^94s4p$, $3d^{10}4p$, and $3d^{10}4s$ configurations fall below the TI threshold. Therefore, electron impact ionization from the $3p$ shell does not yield Se^{6+}.

Nevertheless, the scenario undergoes a significant transformation when accounting for correlation effects. The CIS method is utilized to identify admixed configurations for the Se^{4+} $3p^53d^{10}4s^24p$ configuration. The basis of interacting configurations encompasses $3d^84s^24p\,4f$, $3d^84s^24p\,5f$, $3d^84s^24p\,5p$, $3p^53d^{10}4p^3$, $3p^53d^{10}4s\,4p\,4d$, $3d^84s^24p\,6f$, $3d^84s^24p\,7f$, $3d^84s^24p\,6p$, $3d^84s^24p\,8f$, $3d^84s^24p\,9f$, $3d^94s\,4p^2$, $3d^94s\,4p^2$,

$3d^8 4s^2 4p^2$, $3p^5 3d^{10} 4s\, 4p\, 5d$, and $3s 3p^6 3d^{10} 4s\, 4p^2$ configurations.

This results in a reduction of the total cross sections for electron impact DI initiated by the $3p$ shell ionization with subsequent AI. A 9% decrease is observed for the cross sections at the peak value. The total DI cross sections with the corrected DDI and IA values are presented in Fig. 14 and detailed in Table 9. The partial cross sections for the TI process are presented in Tables 10 – 12.
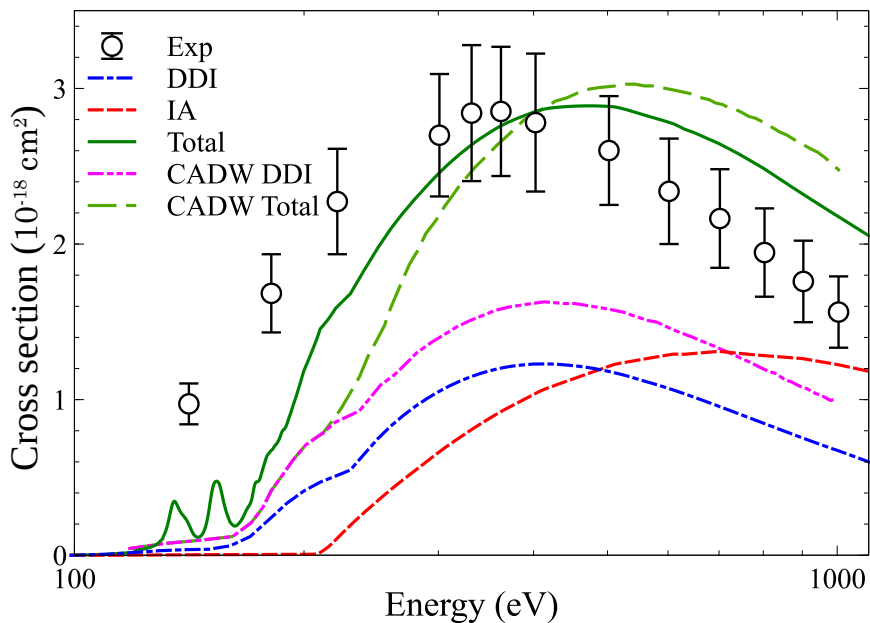
Figure 14. The same as Fig. 11 but the IA cross sections include correlation effects and DDI is diminished by DDI-AI. Dashed-dotted-dotted line (magenta): CADW DDI [42] but II part; dashed-fine line (light green): CADW Total which includes CADW DDI and IA for the $3p$ shell ionization.

For the total DI cross sections, a more favorable alignment with experimental data is achieved at the cross section peak in this scenario. Calculations marginally exceed the experimental error bars at higher energies. Unfortunately, at the lower electron incident energies, theoretical values remain significantly below the measurements, consistent with prior findings [42]. The underlying cause of these disparities remains elusive.

Table 9. Total electron-impact DI cross sections (σ in 10^{-18}cm^2) for the Se^{3+} ion. ε - electron energy, $a \pm b = a \times 10^{\pm b}$.

ε	σ	ε	σ	ε	σ	ε	σ
1.01+2	0.06	1.62+2	15.52	2.03+2	124.93	1.30+3	193.96
1.12+2	0.83	1.63+2	13.92	2.05+2	129.87	1.50+3	179.41
1.19+2	1.68	1.65+2	14.58	2.09+2	142.72	1.70+3	165.06
1.20+2	2.42	1.67+2	20.12	2.12+2	148.60	2.00+3	143.84
1.23+2	3.83	1.68+2	22.96	2.22+2	160.70	3.00+3	109.24
1.25+2	4.51	1.69+2	30.45	2.26+2	164.51	5.00+3	69.29
1.27+2	5.75	1.70+2	32.77	2.34+2	174.48	7.00+3	53.29
1.29+2	7.45	1.71+2	34.56	2.42+2	186.52	8.00+3	47.86
1.30+2	10.08	1.72+2	43.59	2.58+2	207.61	1.10+4	36.32
1.32+2	17.31	1.72+2	50.52	2.70+2	220.30	1.30+4	32.28
1.34+2	28.46	1.74+2	56.23	2.88+2	235.75	1.50+4	28.71
1.35+2	33.14	1.76+2	59.41	3.10+2	251.63	1.90+4	22.55
1.36+2	34.22	1.78+2	64.47	3.30+2	262.76	2.40+4	18.09
1.37+2	30.30	1.79+2	65.84	3.50+2	271.41	3.20+4	13.58
1.38+2	26.09	1.80+2	65.41	3.90+2	282.56	4.00+4	11.27
1.40+2	23.01	1.82+2	65.24	4.20+2	287.14	5.10+4	9.03
1.42+2	18.60	1.83+2	65.76	4.60+2	288.50	5.80+4	8.21
1.43+2	14.39	1.85+2	72.07	4.80+2	288.54	6.20+4	7.79
1.45+2	11.39	1.86+2	77.88	5.00+2	288.24	6.60+4	7.42
1.47+2	12.40	1.88+2	81.19	5.20+2	287.26	7.00+4	7.06
1.48+2	15.83	1.91+2	86.32	5.60+2	282.76	7.60+4	6.57
1.49+2	23.00	1.92+2	92.23	6.00+2	278.20	8.00+4	6.26
1.50+2	30.85	1.93+2	98.52	6.30+2	273.86	8.60+4	5.84
1.52+2	42.41	1.94+2	100.02	6.80+2	266.62	9.30+4	5.38
1.53+2	46.68	1.96+2	103.38	7.40+2	256.96	9.60+4	5.19
1.54+2	47.03	1.99+2	113.92	8.00+2	247.09	9.90+4	5.01
1.56+2	40.82	2.00+2	116.50	8.50+2	239.47	1.00+5	4.95
1.57+2	35.83	2.00+2	118.83	9.10+2	230.69	2.00+5	3.37
1.58+2	30.15	2.01+2	119.66	9.70+2	221.96	3.00+5	2.40
1.59+2	24.42	2.02+2	120.65	1.00+3	218.19	4.00+5	2.07
1.61+2	18.97	2.02+2	121.96	1.10+3	209.61	5.00+5	1.78

Table 10. DDI cross sections (σ in 10^{-18}cm^2) of Se^{3+} ion for the II branch. ε - electron energy in eV, $a \pm b = a \times 10^{\pm b}$.

ε	σ	ε	σ	ε	σ	ε	σ
1.09+2	0.12	2.30+2	39.41	4.50+2	112.30	1.65+3	36.26
1.19+2	1.12	2.44+2	53.43	4.80+2	111.30	1.83+3	31.79
1.29+2	1.80	2.58+2	65.35	5.10+2	109.50	2.00+3	28.07
1.39+2	2.19	2.72+2	74.96	5.40+2	107.00	3.70+3	11.69
1.49+2	2.36	2.86+2	82.91	5.70+2	104.20	5.20+3	6.72
1.60+2	3.44	3.00+2	89.54	6.80+2	93.34	6.70+3	4.34
1.74+2	12.60	3.30+2	100.20	7.60+2	85.34	1.00+4	2.06
1.88+2	23.25	3.60+2	106.90	8.40+2	77.93	2.00+4	0.52
2.02+2	30.36	3.90+2	110.60	1.00+3	65.24	3.00+4	0.24
2.16+2	35.18	4.20+2	112.30	1.29+3	48.90	1.00+5	0.04

Table 11. DDI cross sections (σ in 10^{-18}cm^2) of Se^{3+} ion for the IEI branch with subtracted DDI-AI contribution. ε - electron energy in eV, $a \pm b = a \times 10^{\pm b}$.

ε	σ	ε	σ	ε	σ	ε	σ
1.09+2	3.83−2	1.96+2	3.57+0	3.00+2	4.94+0	2.60+3	6.31−2
1.14+2	2.13−1	2.04+2	4.16+0	3.20+2	4.67+0	3.30+3	3.37−2
1.17+2	2.80−1	2.20+2	4.78+0	3.90+2	3.68+0	4.00+3	2.00−2
1.20+2	3.25−1	2.30+2	4.94+0	4.60+2	2.84+0	4.70+3	1.28−2
1.32+2	6.22−1	2.40+2	5.12+0	5.30+2	2.22+0	1.00+4	1.28−3
1.44+2	7.10−1	2.50+2	5.24+0	6.00+2	1.76+0	3.00+4	4.28−5
1.56+2	7.20−1	2.60+2	5.27+0	7.54+2	1.11+0	5.00+4	1.02−5
1.68+2	8.61−1	2.70+2	5.24+0	8.38+2	8.87−1	7.00+4	3.91−6
1.80+2	1.69+0	2.80+2	5.17+0	9.22+2	7.20−1	9.00+4	2.04−6
1.88+2	2.65+0	2.90+2	5.06+0	1.19+3	4.05−1	1.00+5	1.55−6

Table 12. DDI cross sections (σ in 10^{-18}cm^2) of Se^{3+} ion for the EII branch with subtracted DDI-AI contribution. ε - electron energy in eV, $a \pm b = a \times 10^{\pm b}$.
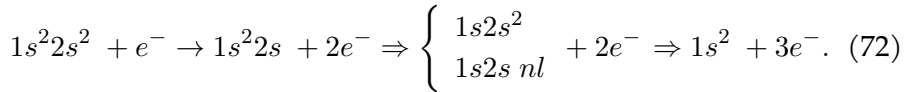
ε	σ	ε	σ	ε	σ	ε	σ
1.09+2	3.61−2	1.96+2	7.47+0	2.97+2	1.06+1	9.22+2	1.73+0
1.11+2	1.16−1	2.04+2	8.60+0	3.08+2	1.04+1	1.19+3	9.93−1
1.13+2	1.82−1	2.12+2	9.37+0	3.19+2	1.01+1	2.50+3	1.69−1
1.17+2	2.82−1	2.20+2	9.87+0	3.20+2	1.01+1	2.60+3	1.53−1
1.20+2	3.35−1	2.31+2	1.02+1	3.90+2	8.16+0	4.20+3	4.29−2
1.32+2	6.07−1	2.42+2	1.07+1	4.60+2	6.44+0	5.80+3	1.70−2
1.44+2	7.09−1	2.53+2	1.09+1	5.30+2	5.11+0	7.40+3	8.05−3
1.68+2	1.44+0	2.64+2	1.10+1	6.00+2	4.09+0	9.00+3	4.27−3
1.80+2	3.94+0	2.75+2	1.10+1	6.70+2	3.32+0	7.00+4	1.42−5
1.88+2	5.81+0	2.86+2	1.08+1	7.54+2	2.63+0	9.00+4	7.82−6

4.3.3. B$^+$ ion [A3]

For B$^+$ ion, the indirect process of DI includes ionization from the $1s$ subshell with subsequent AI:

$$1s^2 2s^2 + e^- \rightarrow 1s2s^2 + 2e^- \rightarrow 1s^2 + 3e^- \qquad (71)$$
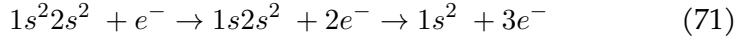
The IE-AI process is described by ionization of the $2s$ subshell with subsequent excitation of the $1s$ subshell and AI:

$$1s^2 2s^2 + e^- \rightarrow 1s^2 2s + 2e^- \Rightarrow \begin{cases} 1s2s^2 \\ 1s2s\ nl \end{cases} + 2e^- \Rightarrow 1s^2 + 3e^-. \qquad (72)$$

The EI-AI process includes the excitation of B$^+$ with subsequent ionization and AI:

$$1s^2 2s^2 + e^- \rightarrow 1s2s^2\ nl + e^- \Rightarrow \begin{cases} 1s2s^2 \\ 1s2s\ nl \end{cases} + 2e^- \rightarrow 1s^2 + 3e^-, \qquad (73)$$

$$1s^2 2s^2 + e^- \rightarrow 1s^2 2s\ nl + e^- \Rightarrow 1s2s\ nl + 2e^- \rightarrow 1s^2 + 3e^-. \qquad (74)$$
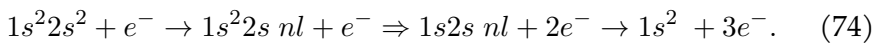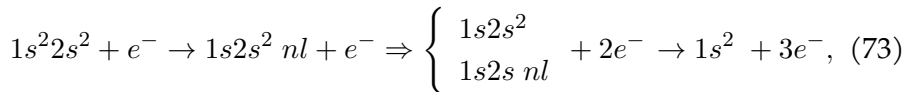
For the $2s$ subshell of B^+ ion, , the DDI II process is defined by the sequential CI:

$$1s^2 2s^2 + e^- \rightarrow 1s^2 2s + 2e^- \Rightarrow 1s^2 + 3e^- \qquad (75)$$
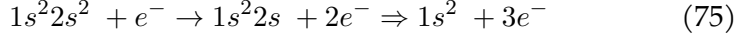
The ionization or excitation by the scattered or ejected electrons is shown by the $\Rightarrow$ symbol. The DDI EII process presents CE with sequential CI of the valence subshells:
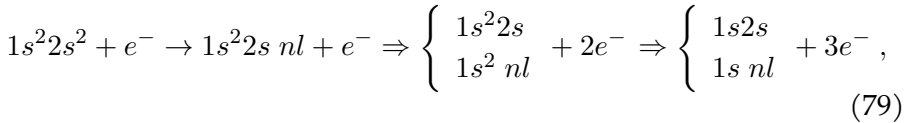
$$1s^2 2s^2 + e^- \rightarrow 1s^2 2s\, nl + e^- \Rightarrow \begin{cases} 1s^2 2s \\ 1s^2\, nl \end{cases} + 2e^- \Rightarrow 1s^2 + 3e^-, \quad (76)$$
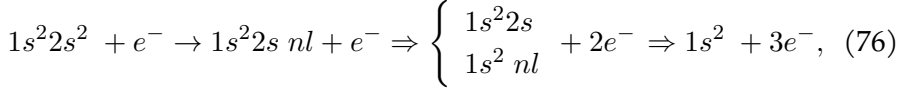
where $n \leqslant 10, l < n$, and $l \leqslant 5$. The DDI IEI process can be schematically shown as

$$1s^2 2s^2 + e^- \rightarrow 1s^2 2s + 2e^- \Rightarrow 1s^2\, nl + 2e^- \Rightarrow 1s^2 + 3e^- \qquad (77)$$
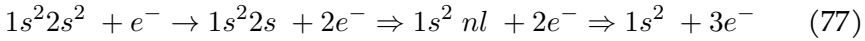
The DDI process that involves $1s$ subshell is studied separately since this subshell was not investigated before [28]. DDI II which includes the $1s$ subshell of B^{2+} is defined as

$$1s^2 2s^2 + e^- \rightarrow 1s^2 2s + 2e^- \Rightarrow 1s2s + 3e^- \qquad (78)$$
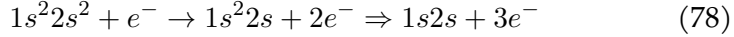
In this case, DDI EII starts by the excitation from the $2s$ subshell:

$$1s^2 2s^2 + e^- \rightarrow 1s^2 2s\, nl + e^- \Rightarrow \begin{cases} 1s^2 2s \\ 1s^2\, nl \end{cases} + 2e^- \Rightarrow \begin{cases} 1s2s \\ 1s\, nl \end{cases} + 3e^-, \quad (79)$$

The DDI IEI process includes the excitation from the $1s$ subshell of the B^{2+} ion:

$$1s^2 2s^2 + e^- \rightarrow 1s^2 2s + 2e^- \Rightarrow 1s^2\, nl + 2e^- \Rightarrow 1s\, nl + 3e^- \qquad (80)$$
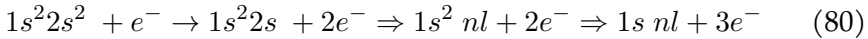
Electron-impact DI cross sections for the B^+ ion are presented in comparison with experimental measurements by Shevelko et al. [100] in Fig. 15. Calculations are performed for the ground level of the B^+ ion utilizing the scaled DW cross sections. The examination of total DI

cross sections involves the analysis of both the DDI and AI processes. The method used to estimate the distribution of excess energy between the scattered and ejected electrons resulting from the initial ionization process relies on the differential cross sections derived from the BED approximation, as explained earlier in this study.
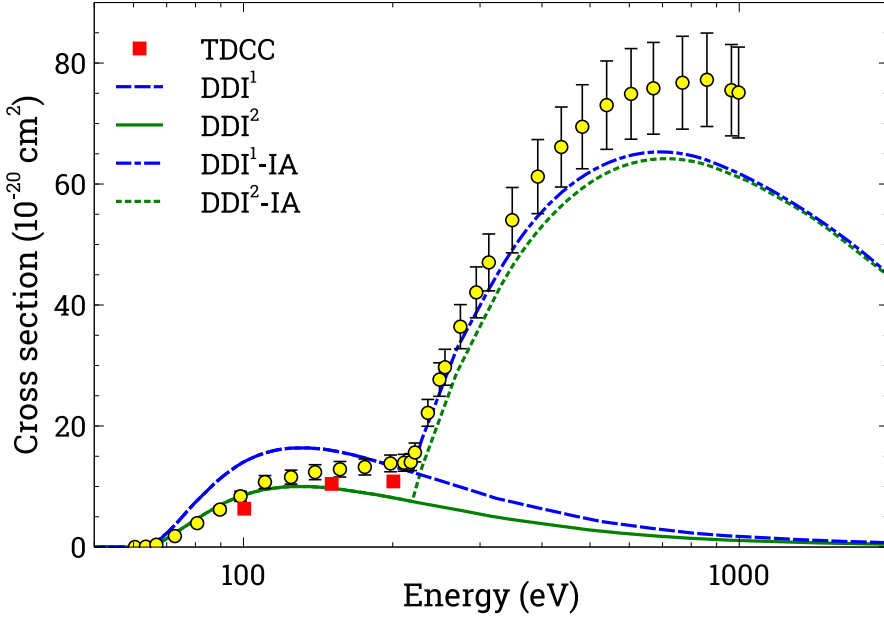

Figure 15. Electron-impact DI cross sections for the ground level of the B^+ ion. Configurations with vacancy in the $1s$ subshell are not included in the study of the DDI process. DDI^1: CI cross sections obtained in the potentials of the ionizing ions; DDI^2: $B^+ \rightarrow B^{2+}$ CI cross sections obtained in the potential of the ionizing ion but $B^{2+} \rightarrow B^{3+}$ CI cross sections obtained in the potential of the ionized ion; DDI^1-IA: sum of DDI^1 and IA cross sections; DDI^2-IA: sum of DDI^2 and IA cross sections. TDCC: previous calculations [28]. Yellow circles with error bars: experiment for 9% of metastable fraction in the ion beam [100].

Configurations with a vacancy in the $1s$ subshell have been excluded from the investigation of the DDI process. This practice aligns with prior calculations that utilized the TDCC approach for the DDI process, which similarly did not incorporate the $1s$ subshell [28]. To address this

omission, an extrapolation technique was employed, commencing from the ionization threshold of the $1s$ subshell [28].

In this investigation, the CI cross sections used to calculate the DDI cross sections through a multi-step approach for ionization from the levels of the B^+ ion are examined within the potential of the ionizing ion. The potentials of both the ionized and ionizing ions are employed to analyze the CI process involving the levels of the B^{2+} ion generated by ionization from the B^+ ion. The DDI cross sections obtained within the potentials of the ionizing ions are approximately $\sim 6 \cdot 10^{-20}$ cm^2 higher when compared to the theoretical values calculated within the potentials of the ionizing and ionized ions (Fig. 15).

As can be seen from Fig. 15, the theoretical DDI cross sections obtained in the potentials of the ionizing and ionized ions are in good agreement with experiment at the lower energies of the incident electron. At energies near the ionization threshold of the $1s$ subshell, the DDI cross sections, when analyzed within the potential of the ionizing ion, exhibit good agreement with experimental measurements. The TDCC cross sections, available only between the DDI threshold and the inner-shell SI threshold, are slightly lower than the experimental measurements.

While quite good agreement with measurements is observed in both cases of theoretical calculations for total DI at energies beyond the inner shell ionization threshold (Fig. 15). However, the theoretical cross sections start to decrease more rapidly than the experimental ones, leading to a significant discrepancy at the peak and beyond, where the theoretical DI cross sections strongly underestimate the experimental values. This indicates the presence of additional ionization processes that are not considered in the study presented above and should be taken into account.

The contribution of various pathways to the electron-impact DDI process for the B^+ ion is depicted in Fig. 16. It is evident that the II path overwhelmingly dominates over IEI and EII. The II pathway accounts for approximately 70% of the total DDI cross sections, while the contribution of IEI is slightly higher but comparable to that of EII.
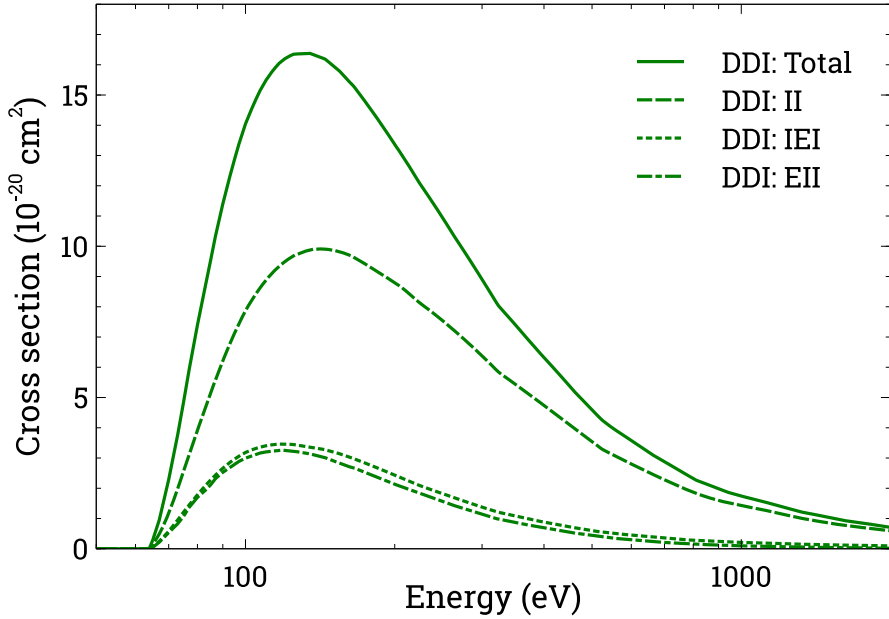
Figure 16. Contribution of various multi-step paths to the total DDI process of the B^+ ion. See explanations in the text for the listed processes.

The DDI study is expanded to encompass ionization originating from the $1s$ subshell of B^{2+} ion configurations. The resultant configurations of the B^{3+} ion, featuring a single vacancy in the $1s$ subshell, lie below the TI threshold. The outcomes of this extension are showcased in Fig. 17.

It becomes evident that the augmentation of DDI cross sections at higher energies, resulting from the inclusion of ionization from the $1s$ subshell of the B^{2+} ion, yields an improved alignment between the total theoretical DI cross sections and experimental results. Contribution of the additional EI-AI and IE-AI processes (Eqs. (58) and (59)) leads to even more improved agreement with experimental cross sections at higher energies of incident electron (Fig. 18).
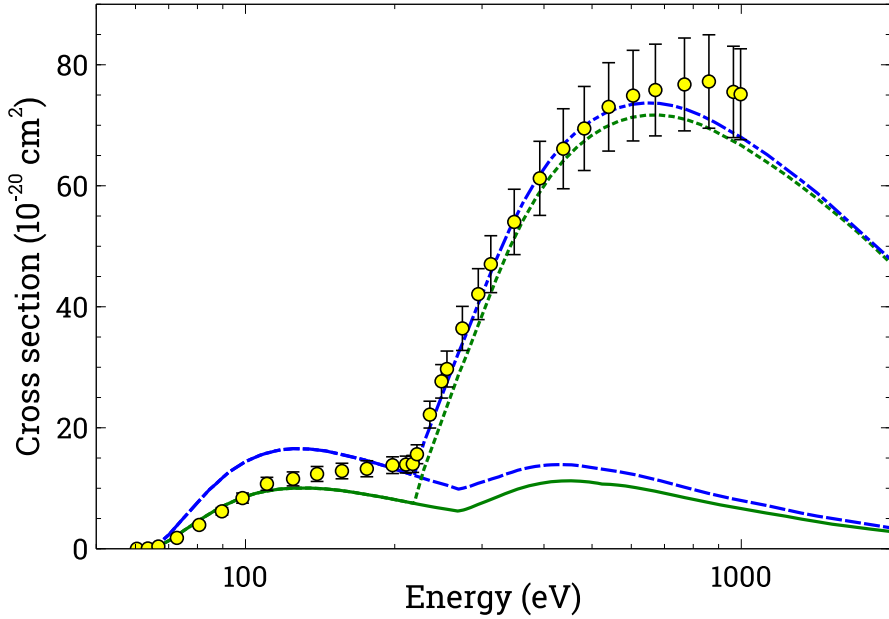
Figure 17. Same as Fig. 15, but includes ionization from the $1s$ subshell of the B^{2+} ion for the DDI process. See explanations in the text.

Comparison with the previous calculations [28] that utilized the TDCC method for DDI and CADW for the indirect DI process is also presented in Fig. 18. The current values slightly exceed the previous calculations. This discrepancy could be attributed to the extrapolation of the DDI cross sections beyond the $1s$ subshell ionization threshold, which might have introduced inaccuracies in the DDI values of previous studies. Moreover, their DDI calculations omitted the $1s$ subshell. This underscores the significance of the EI-AI and IE-AI processes in the DI of B^+. These processes involve excitations from the $1s$ subshell. In the case of EI-AI, this entails excitations to the B^+ $1s2s^2nl$ ($n \leqslant 4$, $l \leqslant n$) configurations, followed by ionization from the $2s$ or nl subshells (Eq. (74)). The resulting configurations are susceptible to AI effects. Notably, cross section convergence must be studied for electron-impact excitations to ensure reliable data.
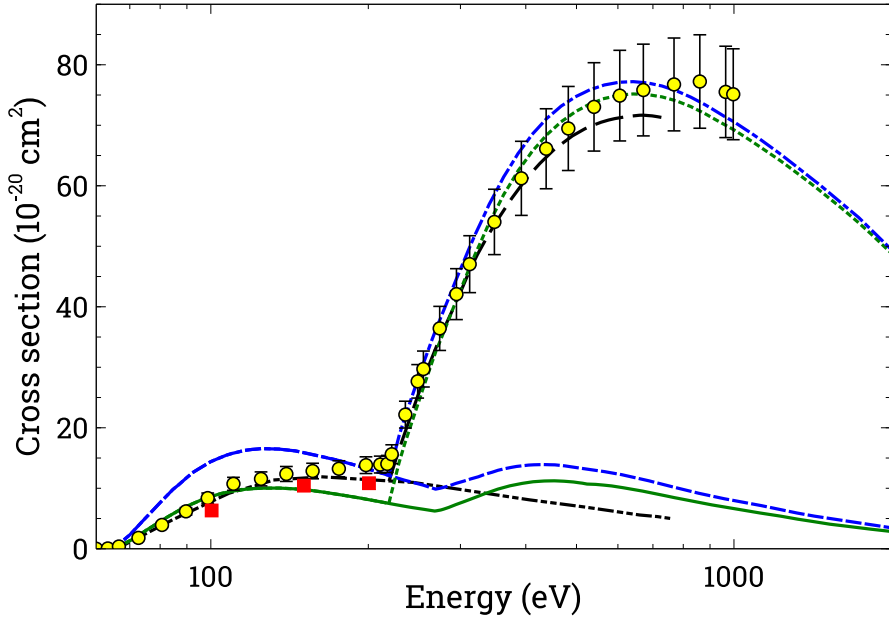
Figure 18. Same as Fig. 17, but with the EI-AI and IE-AI processes included. Solid squares (red): TDCC calculations [28]; dashed-fine line (black): CADW calculations for the SI of the $1s$ subshell of the ground configuration added to a background of TDCC fit (black dash-dot-dot line). See explanations in the text.

Earlier studies on tungsten ions with an open $4f$ subshell in the ground configurations underscored the significance of high-nl excitations for the indirect SI process [97–99, 101–103]. Channels corresponding to excitations in shells with principal quantum numbers $n > 4$ contribute approximately 3% to the total excitation cross sections for the B^+ ion.

For the IE-AI process, ionization from the $2s$ subshell of the B^+ ion yields the $1s^2 2s$ configuration. Excitations from the $1s$ subshell of B^{2+} generate autoionizing configurations that subsequently decay into states of the B^{3+} ion (Eq. (72)). The cross sections for the IE-AI process peak at around $\sim 4 \times 10^{-20}$ cm^2 ($\sim$400 eV), whereas EI-AI yields values approximately an order of magnitude lower.

It's worth noting that the IE-AI and EI-AI processes culminate in AI, as opposed to CI. The CI from autoionizing configurations stemming from the initial IE and EI processes corresponds to the IEI and EII pathways

of the DDI process. However, not all autoionizing states of the B^{2+} ion ultimately transition to the B^{3+} ion during the final stages of IEI and EII, as the final CI is determined by a probability lower than one (as seen in Eq. (49) and (50)). In contrast, all autoionizing states of the B^{2+} ion undergo Auger transitions leading to the B^{3+} ion. This explains why the $1s$ subshell of B^{2+} is initially excluded from the study of the DDI process presented in Fig. 15. Excitations and ionizations from the $1s$ subshell are separately investigated, given that they give rise to autoionizing states whose populations are significantly diminished by Auger transitions.

Additionally, ionization from the $1s$ subshell of the B^+ ion results in autoionizing states that decay via Auger transitions to B^{3+}. However, a portion of these states proceeds to B^{3+} via CI involving scattered or ejected electrons in the II or IEI paths of the DDI process. These processes, specifically DDI(II) and DDI(IEI), which involve the initial ionization from the $1s$ subshell of B^+ ion, compete with IA to reach the states of B^{3+} first. In the DDI process, the final CI from autoionizing states is expected to occur more promptly compared to Auger transitions, assuming an instantaneous interaction with the bound electrons. However, as mentioned earlier, not all populations of the autoionizing states of the B^{2+} ion are depleted by the final CI in the DDI process, leading to their further decay through Auger transitions.

In both scenarios, the states of the B^{3+} ion are eventually attained. Hence, the analysis of the produced autoionizing states exclusively considers Auger transitions, as this ensures a complete population transfer to the B^{3+} ion. Limiting the study solely to the DDI process involving autoionizing states would yield lower cross sections in comparison to the IE-AI, EI-AI, and IA processes.

4.3.4. Conclusions

For DI of the Se^{2+} ion, there is good agreement with experimental data near the peak of experimental cross sections. However, the theoretical cross sections tend to overestimate the experimental ones at higher incident electron energies, while underestimating the experimental values at lower energies. The exact reasons for these differences remain unclear, and further experiments may be necessary to resolve this discrepancy.

In the case of DI of the Se^{3+} ion, the excitation from the $3p$ subshell, followed by double autoionization, contributes significantly to the formation of Se^{5+} ions. Conversely, DC, which involves excitation from the $3p$ subshell, provides the lowest contribution among the considered processes. This process plays a more prominent role at lower incident electron energies.

In the study of DI for the B^+ ion, the EI-AI and IE-AI processes, which involve excitations from the $1s$ subshell, have been included. The additional contribution from these processes enhances the agreement with measurements, especially at higher energy levels. Only the DDI process is responsible for the formation of states of the B^{3+} ion in the energy range from the DI threshold up to the SI threshold of the $1s$ subshell. Within the DDI process, the double ionization (II) path dominates over the IEI and EII paths.

4.4. Electron-Impact Triple Ionization

4.4.1. Se^{2+} ion [A1]

Electron-impact TI cross sections for the Se^{2+} ion are presented in Fig. 19. TI is investigated starting from the highest $4p^2\,{}^1S_0$ level of the ground configuration. In this study, the contribution from the DDI-AI process and the Auger cascade following the ionization of the $3p$ subshell is taken into account. Theoretical values at the peak are slightly higher than the experimental data when one of the electrons absorbs all the excess energy during DDI.
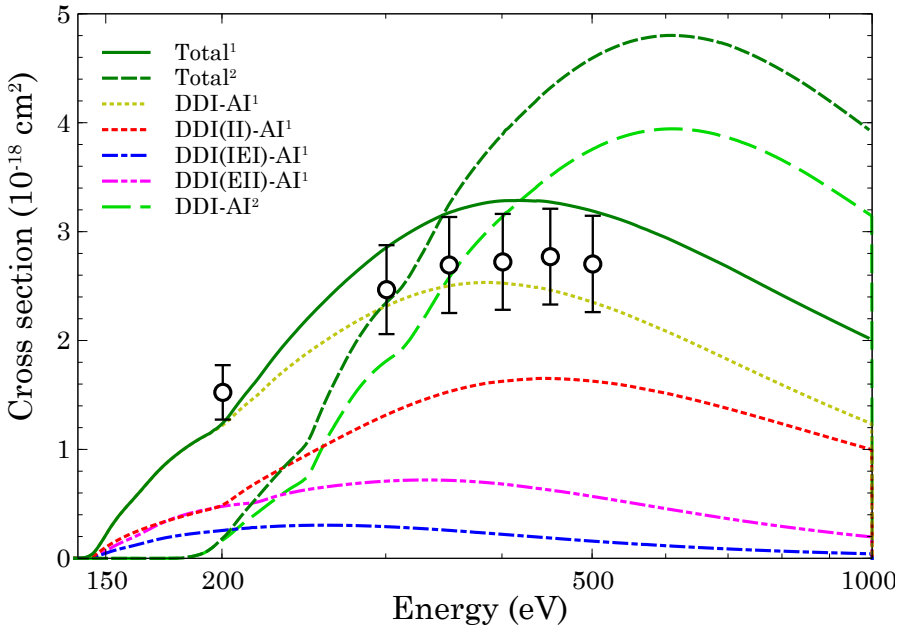
Figure 19. Contribution of various pathways to the electron-impact TI of Se^{2+}. Superscript 1: TI cross sections when one of the electrons takes all excess energy in the DDI process; superscript 2: TI cross sections when scattered and ejected electrons share equally the excess energy in the DDI process; hollow circles: experiment [38] See explanations in the text for the DDI-AI, DDI(II)-AI, DDI(IEI)-AI and DDI(EII)-AI processes.

It's important to note that studies incorporating correlation effects for Auger cascades lead to the production of ions in higher ionization stages [55, 56], which would likely result in better agreement for the TI cross sections.

Conversely, calculations performed in the potential of the ionizing ion yield cross sections approximately 20% lower at the peak. These obtained TI cross sections underestimate the experimental ones at lower energies and overestimate them at higher energies of the incident electron when the excess energy is equally shared between the electrons.

The largest contribution to the total TI cross sections comes from the DDI-AI process, accounting for more than 75 percent of the total TI cross sections at the peak (Fig. 19). Interestingly, the DDI(II)-AI process contributes to about 70% of the total DDI-AI cross sections, with smaller contributions from DDI(II)-AI and DDI(IEI)-AI processes. It's worth noting that the two-step II process has the most significant impact on the TI process at its peak. However, at lower incident electron energies, three-step processes provide a larger contribution compared to the two-step process. Furthermore, the three-step EII process dominates over the IEI process. This can be explained by the fact that excitations like $4s \rightarrow 4p$ and $4p \rightarrow 4d$ have larger cross sections compared to ionization from the $3d$, $4s$, and $4p$ subshells.

Additionally, DDI with subsequent Auger cascade contributes to the Se^{6+} ion. However, the cross sections for quadrupole ionization are approximately an order of magnitude smaller compared to the TI cross sections.

Configurations of the Se^{4+} ion obtained from DDI for the $4p^2$ $^1S_0$ level that can decay to Se^{5+} include $3d^84s^24p^2$, $3d^84s\ 4p^3$, $3d^94s\ 4p^2$, $3d^94p^3$, $3d^94s\ 4p\ 4d$, and $3d^94s^24d$. The highest population is obtained for levels of the $3d^84s^24p^2$ and $3d^94s; 4p^2$ configurations of Se^{4+} at the peak of the TI cross sections. In contrast, the $3d^84s; 4p^3$ configuration, ranked third in terms of population, has a level population more than four times smaller than that of the first two configurations.

DDI-AI process gives rise to the formation of the Se^{5+} $3d^{10}4s$, $3d^{10}4p$, $3d^{10}4d$, $3d^94p^2$, $3d^94s^2$, and $3d^94s; 4p$ configurations. Among these, the $3d^{10}4s$ and $3d^94s; 4p$ configurations exhibit the highest population at the peak of the TI cross sections. The population of the other Se^{5+} configurations is roughly half as much in comparison.

The contribution of the Auger cascade following the SI of the $3p$ electron of the Se^{2+} ion accounts for approximately 25 percent of the total TI cross sections. In this process, the Se^{3+} $3p^5 3d^{10} 4s^2 4p^2$ configuration decays into the Se^{5+} ion through two main pathways: the $3d^8 4s^2 4p^2$ and $3d^9 4s^1 4p^2$ configurations. The primary route for population transfer to Se^{5+} is via the $3d^9 4s^1 4p^2$ configuration, particularly at lower incident electron energies.

Ionization of the $3s$ and deeper subshells, followed by Auger cascade, has not been analyzed due to their much lower SI cross sections compared to those of the $3p$ subshell. Additionally, the energy levels of configurations produced by ionization of the $3d$ subshell are below the TI threshold, meaning that this process does not influence the population of Se^{5+} ions through Auger cascade.

Furthermore, it is evident that the excited $4p^2$ $^1S_0$ level, resulting from the SI of the $3p$ electron of the Se^{2+} ion (Fig. 20) exhibits a significant increase in cross sections across the entire energy range. This is in contrast to the contribution of the ground $4p^2$ $^3P_0$ level.
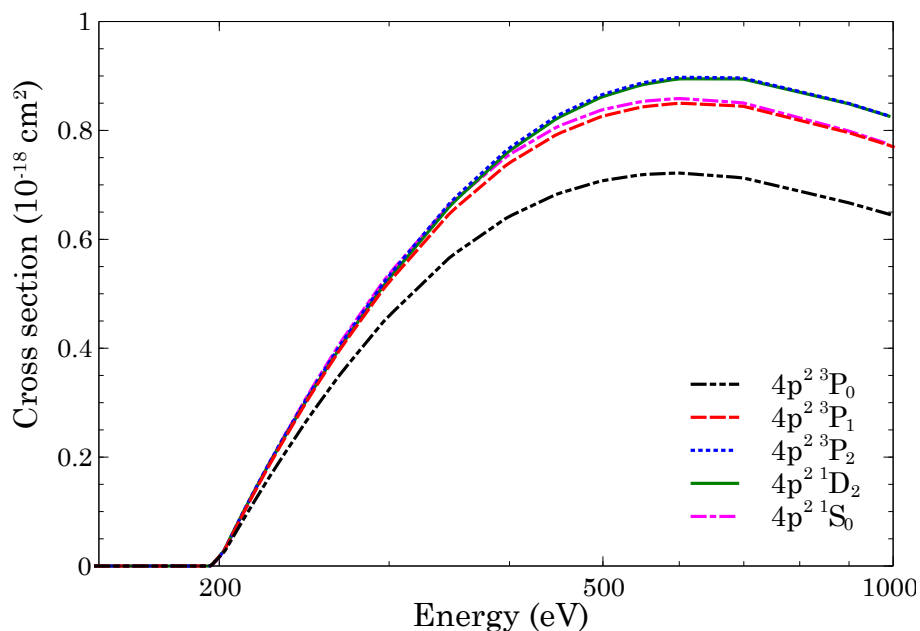
Figure 20. Electron-impact SI of $3p$ shell of Se^{2+} for energy levels of the ground configuration.

4.4.2. Se^{3+} ion [A2]

The total TI cross sections for the Se^{3+} ion are depicted in Fig. 21, along with the contributions of various processes to the total TI cross sections. As illustrated in this figure, the total TI cross sections attain their maximum value at an incident electron energy of 440 eV. Total TI cross sections are presented in detail in Table 13.

The DDI-AI process primarily contributes to the majority of the TI cross sections, accounting for 79% at the peak of the total TI cross sections. Although the influence of the DDI-AI process decreases at higher energies, it still maintains a significant contribution across the entire range of considered energies. The cross sections of the DDI-AI process are detailed in Table 14.
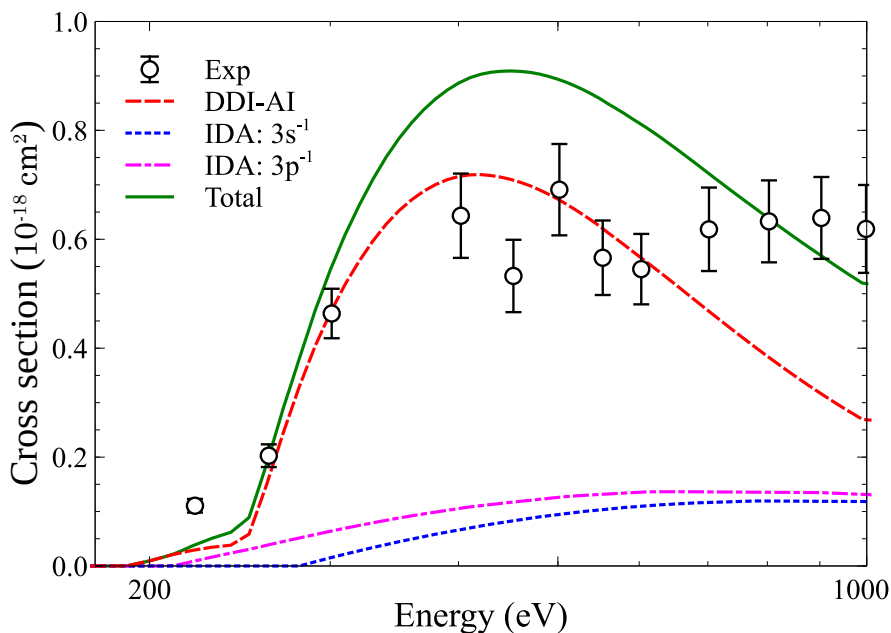
Figure 21. Electron-impact TI cross sections for the Se^{3+} ion. Dashed line (red): DDI with subsequent autoionization (DDI-AI); dotted line (blue): ionization from the $3p$ subshell with double autoionization; dashed-dotted line (magenta): ionization from the $3p$ subshell with double autoionization; solid line (green): total.

Table 13. Total TI cross sections (σ in 10^{-18}cm^2). ε - electron energy in eV, $a \pm b = a \times 10^{\pm b}$.

| ε	σ	ε	σ	ε	σ	ε	σ
1.9+2	0.03	3.9+2	86.98	6.0+2	81.67	3.7+3	14.72
2.0+2	1.55	4.1+2	89.34	6.0+2	81.23	4.8+3	11.39
2.2+2	3.53	4.2+2	90.53	7.1+2	71.62	5.9+3	9.47
2.3+2	5.45	4.4+2	90.90	8.2+2	62.91	8.1+3	7.28
2.5+2	7.36	4.6+2	90.82	9.2+2	55.73	9.8+3	6.06
2.5+2	8.13	4.8+2	90.26	1.5+3	33.78	2.5+4	2.75
2.7+2	32.90	5.0+2	89.30	1.6+3	31.59	4.2+4	1.75
3.0+2	53.73	5.2+2	88.06	1.7+3	29.69	5.9+4	1.27
3.2+2	68.23	5.4+2	86.62	1.8+3	27.98	1.0+5	0.74
3.5+2	78.20	5.6+2	84.99	2.0+3	26.43	4.0+5	0.26
3.7+2	83.40	5.8+2	83.41	2.6+3	20.35	6.0+5	0.18

Table 14. DDI-AI cross sections (σ in 10^{-18}cm^2). ε - electron energy in eV, $a \pm b = a \times 10^{\pm b}$.

ε	σ	ε	σ	ε	σ	ε	σ
1.90+2	0.01	4.00+2	71.55	4.97+2	67.63	1.34+3	15.44
2.21+2	2.95	4.10+2	71.84	5.16+2	65.84	1.50+3	12.01
2.44+2	3.97	4.15+2	71.91	5.33+2	64.12	1.62+3	10.35
2.49+2	5.14	4.22+2	71.88	5.46+2	62.76	1.88+3	7.70
2.53+2	7.65	4.27+2	71.79	5.66+2	60.54	2.00+3	6.78
2.61+2	15.83	4.32+2	71.67	5.83+2	58.68	2.30+3	5.05
2.85+2	36.98	4.37+2	71.51	6.00+2	56.87	2.60+3	3.78
3.05+2	49.20	4.42+2	71.34	6.28+2	54.01	3.40+3	2.00
3.16+2	54.31	4.47+2	71.14	6.51+2	51.69	4.00+3	1.33
3.38+2	62.22	4.51+2	70.95	7.20+2	45.12	4.80+3	0.82
3.60+2	67.28	4.62+2	70.36	8.38+2	35.79	7.00+3	0.29
3.75+2	69.51	4.71+2	69.74	1.00+3	26.43	1.00+4	0.10
3.91+2	71.03	4.86+2	68.58	1.19+3	19.35	2.00+4	0.01

The contribution of the three-step DDI processes to the TI cross sections is illustrated in Fig. 22. Among the branches of the DDI-AI process, the EII process with subsequent AI from the excited levels plays the primary role in the formation of TI cross sections, constituting about 83% at the peak value of DDI-AI when one of the electrons absorbs all the excess energy after the initial ionization process.
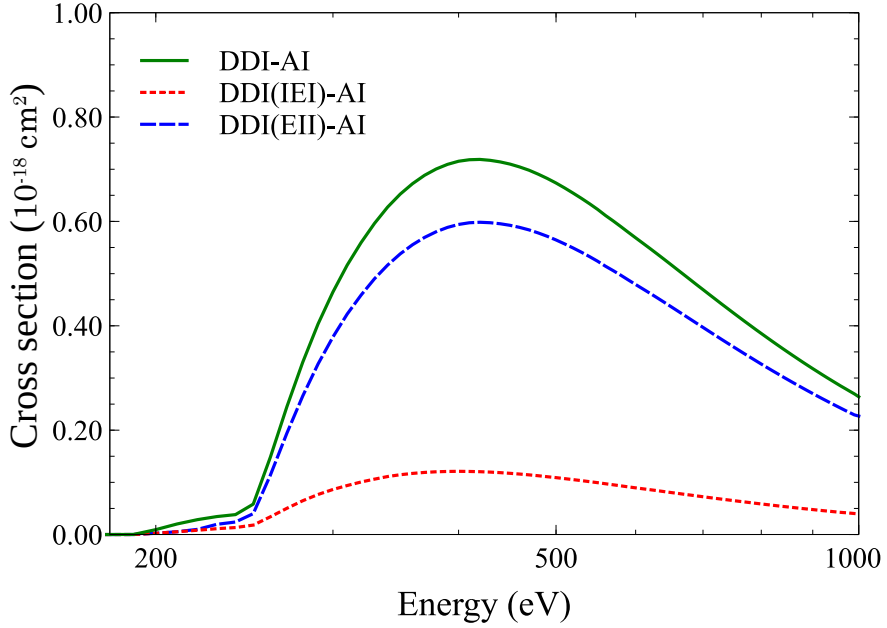
Figure 22. DDI-AI cross sections for the Se^{3+} ion.

The obtained results reveal that the majority of the population (79%) at the peak of cross sections for EII corresponds to the Se^{6+} $3d^94s$ configuration. The second most populated configuration is Se^{6+} $3d^94p$ (4%), while the population of the ground configuration of Se^{6+} is 3%. The cross sections for the EII and IEI branches of the DDI-AI process are provided in Tables 15 and 16.

Table 15. DDI-AI cross sections (σ in $10^{-18}\mathrm{cm}^2$) for the EII branch. ε - electron energy in eV, $a \pm b = a \times 10^{\pm b}$.

ε	σ	ε	σ	ε	σ	ε	σ
1.90+2	5.87−3	3.88+2	5.87+1	1.29+3	1.42+1	5.00+3	6.38−1
2.04+2	9.35−1	4.18+2	5.99+1	1.64+3	8.64+0	6.20+3	3.54−1
2.18+2	1.75+0	4.56+2	5.90+1	1.75+3	7.63+0	7.40+3	2.13−1
2.32+2	2.27+0	5.24+2	5.46+1	1.86+3	6.75+0	8.60+3	1.37−1
2.46+2	2.78+0	5.92+2	4.86+1	1.97+3	6.00+0	9.80+3	9.27−2
2.60+2	1.14+1	6.60+2	4.29+1	2.00+3	5.82+0	2.00+4	1.10−2
2.72+2	2.10+1	7.28+2	3.76+1	2.70+3	2.96+0	4.00+4	2.00−3
2.84+2	2.92+1	7.96+2	3.29+1	3.20+3	2.00+0	6.00+4	8.01−4
2.96+2	3.60+1	8.64+2	2.89+1	3.70+3	1.39+0	9.00+4	3.31−4
3.08+2	4.13+1	9.32+2	2.55+1	4.20+3	1.01+0	1.00+5	2.50−4
3.20+2	4.59+1	1.00+3	2.25+1	4.70+3	7.52−1	6.00+5	7.02−6

Table 16. DDI-AI cross sections (σ in $10^{-18}\mathrm{cm}^2$) for the IEI branch. ε - electron energy in eV, $a \pm b = a \times 10^{\pm b}$.

ε	σ	ε	σ	ε	σ	ε	σ
1.90+2	3.73−3	3.10+2	9.40+0	5.89+2	9.16+0	3.20+3	3.23−1
2.04+2	5.06−1	3.41+2	1.12+1	6.20+2	8.60+0	5.00+3	9.48−2
2.18+2	9.83−1	3.72+2	1.19+1	6.99+2	7.26+0	9.00+3	1.78−2
2.32+2	1.28+0	4.03+2	1.21+1	7.78+2	6.14+0	2.00+4	1.69−3
2.46+2	1.50+0	4.34+2	1.19+1	8.57+2	5.21+0	4.00+4	2.71−4
2.60+2	3.43+0	4.65+2	1.15+1	9.36+2	4.46+0	6.00+4	9.38−5
2.70+2	5.07+0	4.96+2	1.10+1	1.33+3	2.26+0	8.00+4	4.66−5
2.80+2	6.49+0	5.16+2	1.06+1	1.52+3	1.73+0	9.00+4	3.36−5
2.90+2	7.70+0	5.27+2	1.04+1	1.71+3	1.34+0	1.00+5	2.69−5
3.00+2	8.65+0	5.58+2	9.78+0	1.90+3	1.08+0	6.00+5	3.23−7

At the peak value of the total TI cross sections, the contributions from ionization of the $3s$ and $3p$ subshells amount to approximately 12% and 9%, respectively. The cross sections of these processes are detailed in Tables 17 and 18. The contribution of these processes to the total TI cross section increases with the rising energy of the incident electron.

Table 17. IDA cross sections (σ in $10^{-18}\mathrm{cm}^2$) for the $3s$ subshell. ε - electron energy in eV, $a \pm b = a \times 10^{\pm b}$.

ε	σ	ε	σ	ε	σ	ε	σ
2.8+2	0.07	7.6+2	11.87	1.4+3	10.81	1.3+4	2.41
3.3+2	3.26	8.0+2	11.95	1.8+3	9.69	2.0+4	1.63
3.8+2	6.00	8.3+2	11.97	2.1+3	8.99	3.5+4	1.07
4.4+2	7.87	9.2+2	11.97	2.7+3	7.85	5.0+4	0.72
5.2+2	9.74	9.4+2	11.95	3.1+3	7.22	1.0+5	0.38
5.6+2	10.41	9.7+2	11.92	4.1+3	5.94	2.0+5	0.27
6.2+2	11.09	1.0+3	11.87	6.2+3	4.32	4.0+5	0.17
7.0+2	11.66	1.2+3	11.40	8.6+3	3.36	6.0+5	0.10

Table 18. IDA cross sections (σ in $10^{-18}\mathrm{cm}^2$) for the $3p$ subshell. ε - electron energy in eV, $a \pm b = a \times 10^{\pm b}$.

ε	σ	ε	σ	ε	σ	ε	σ
2.8+2	0.07	7.0+2	11.66	1.2+3	11.40	1.3+4	2.41
3.3+2	3.26	7.6+2	11.87	1.4+3	10.81	2.0+4	1.63
3.8+2	6.00	8.0+2	11.95	1.8+3	9.69	3.5+4	1.07
4.4+2	7.87	8.3+2	11.97	2.1+3	8.99	5.0+4	0.72
4.7+2	8.79	9.2+2	11.97	3.1+3	7.22	1.0+5	0.38
5.2+2	9.74	9.4+2	11.95	4.1+3	5.94	2.0+5	0.27
5.6+2	10.41	9.7+2	11.92	6.2+3	4.32	4.0+5	0.17
6.2+2	11.09	1.0+3	11.87	8.6+3	3.36	6.0+5	0.10

The theoretical values surpass the measurements at the peak of the total cross sections. Experimental data slightly exceed the calculations at both lower and higher incident electron energies. The divergence between theoretical and experimental values could be attributed to correlation effects, which may play a significant role in the DDI process.

Nevertheless, a comprehensive examination of these effects would necessitate a separate study.

The corresponding MRCs are listed in Table 19.

Table 19. Maxwellian rate coefficients for the CI, IA, IDA, DDI-AI, and EDA processes in $cm^3\ s^{-1}$. Temperatures (T_e) are given in K. $a \pm b = a \times 10^{\pm b}$.

T_e	CI	IA	IDA	DDI-AI	EDA
6.894+1	2.069−12	5.551−11	5.382−12	1.159−10	1.132−10
1.723+2	3.398−11	4.698−10	4.807−11	5.930−10	3.699−10
3.447+2	9.216−11	8.984−10	9.393−11	8.587−10	4.766−10
6.894+2	1.550−10	1.270−09	1.351−10	8.550−10	4.769−10
1.724+3	2.021−10	1.740−09	1.878−10	7.692−10	4.076−10
3.447+3	2.006−10	1.815−09	1.970−10	6.334−10	3.516−10
6.894+3	1.799−10	1.661−09	1.810−10	4.647−10	2.940−10
1.724+4	1.439−10	1.310−09	1.432−10	3.178−10	2.182−10
3.467+4	1.162−10	1.041−09	1.139−10	2.314−10	1.642−10
6.894+4	9.412−11	8.035−10	8.800−11	1.447−10	1.041−10
1.724+5	7.092−11	5.224−10	5.749−11	1.324−10	6.923−11
3.447+5	4.744−11	3.178−10	3.532−11	1.413−10	6.102−11

4.4.3. B$^+$ ion [A3]

The TI process is examined for the B$^+$ ion, specifically considering DDI with subsequent AI. The sequential ionization from the $1s$ subshell of the B$^+$ ion results in the B^{3+} $2s^2$ configuration, which subsequently decays to B^{4+}. Since, to the best of our knowledge, no experimental data are available for TI in the B$^+$ ion, only the theoretical TI cross sections are presented in Fig. 23.

Two different potentials are considered for the TI cross sections. Notably, the TI cross sections are two orders of magnitude lower than the DI cross sections. The peak of the cross sections is observed at around ~1300 eV, with a maximum value of $0.18 \cdot 10^{-20}$ cm^2 in the case of studying in the potentials of the ionizing ions. The calculations in the ionizing and ionized potentials are approximately 0.6% lower compared to the study in the ionizing potentials. It's worth noting that experimental

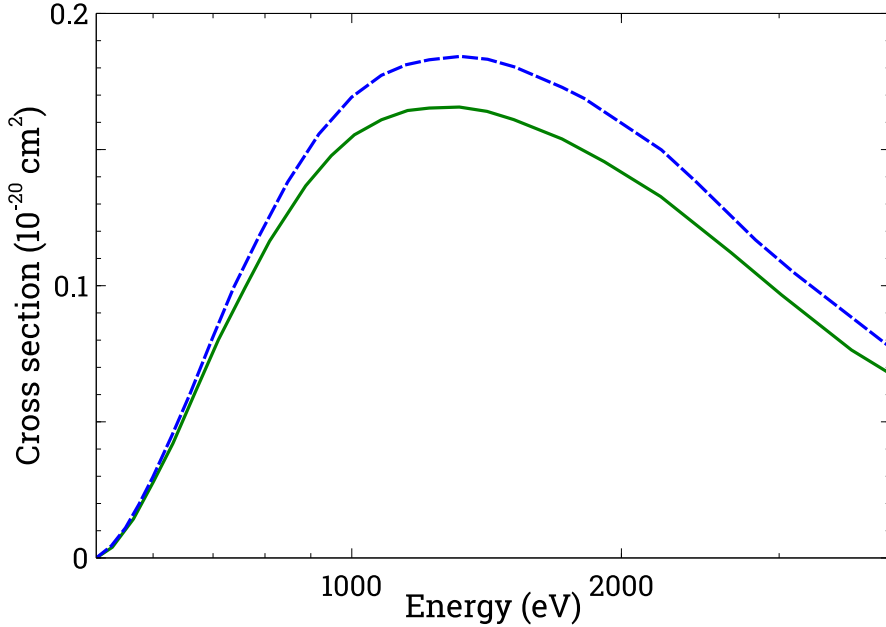results are needed to determine which case more accurately describes the TI process.

Figure 23. Electron-impact TI (DDI-AI) cross sections for the B^+ ion. See explanations in the text.

Finally, the most significant disparity between experimental and theoretical values is observed for the DDI cross sections below the $1s$ subshell ionization threshold, with an uncertainty of approximately 50% in this energy range. A similar level of disagreement is found between theoretical results calculated in different potentials (Fig. 18). Significantly better agreement with measurements is achieved for energies beyond the $1s$ subshell ionization threshold. The calculated DI and TI cross sections for different potentials agree within approximately 10% for peak values.

4.4.4. Conclusions

In the case of the Se^{2+} ion, our current findings indicate that the TI process is primarily formed through DDI with subsequent AI, along with the Auger cascade following electron-impact ionization from the $3p$ subshell. Importantly, our results demonstrate that the knock-out model

with subsequent AI prevails over the Auger cascade in contributing to the TI process.

A high level of agreement with experimental cross sections for the TI of the Se^{2+} ion was achieved by assuming that all excess energy following the initial interaction with the target ion during DDI is captured by one of the electrons. The contribution of the DDI-AI process to the overall TI cross sections exceeds 75%.

For the Se^{3+} ion, it is demonstrated that excitation from the $3p$ subshell followed by double autoionization significantly contributes to the formation of Se^{5+} ions. Conversely, DC process involving $3p$ subshell excitation exhibits the smallest contribution among the considered processes. This process becomes more prominent at lower incident electron energies. Nevertheless, disparities persist between theoretical predictions and experimental measurements for DI cross sections within this energy range. Potential future experiments may offer insights to address this issue.

The DDI process, involving sequential ionization from the $1s$ subshell, results in the autoionizing $2s^2$ configuration of the B^{3+} ion, which subsequently decays to B^{4+}. It's noteworthy that the TI cross sections for the B^+ ion are approximately two orders of magnitude lower than the DI cross sections.

5. MAIN CONCLUSIONS

Electron-impact DI and TI are examined through a multi-step approach, which breaks down direct DI into distinct two- and three-step processes (II, EII, IEI). Additionally, the study encompasses supplementary two-step processes (EI-AI and IE-AI) in the analysis of indirect DI and TI. The required atomic parameters are computed using the FAC [45], which employs the DFS method. The electron-impact excitation and ionization processes are studied employing the DW approximation.

1. The study of DDI shows significant contribution of three-step processes to DI and TI. The largest contribution is seen in case of Se^{3+} ion, where three-step processes contribute up to around 40% of the total DDI cross sections near the peak value:

    1.1 For the B^+ ion, the II path dominates over IEI and EII. However, the IEI and EII processes together contribute to approximately 30% of the DDI. The contribution of IEI is slightly higher but comparable to that of EII.

    1.2 For Se^{2+} ion, the DDI(II)-AI process contributes to approximately 70% of the total DDI-AI cross sections at the peak, with smaller contributions from DDI(EII)-AI and DDI(IEI)-AI. However, at lower incident electron energies, the three-step processes provide the largest contribution compared to the two-step process. At an energy of 200 eV, DDI(EII)-AI and DDI(IEI)-AI processes together contribute about 60% to the total DDI-AI cross sections, with the three-step EII process dominating over the IEI process.

    1.3 For Se^{3+} ion, the IEI and EII paths contribute to approximately 40% of the total cross sections at the peak of cross sections. The EII process plays a significant role in the formation of the DDI cross sections, accounting for about 34% of the total DDI cross sections at the peak value. The contribution from the IEI process amounts to 8%.

2. For B^+ ion, the study includes the EI-AI and IE-AI processes, involving excitations from the $1s$ subshell. These processes contribute up to 9% to the total DI cross sections. The additional contribution

from these processes improves agreement with measurements at the high-energy side.

3. Correlation effects reduce theoretical electron-impact DI cross sections for B^+ and Se^{3+} ions.

   3.1 For B^+ ion, the correlation effects improve the theoretical ionization thresholds by adding approximately 1.6 eV to the single-configuration data, but the SI cross sections are reduced by only about 2% when considering the correlation effects.

   3.2 For Se^{3+} ion, when the correlation effects are taken into account, electron-impact CI from the $3p$ subshell with subsequent double AI contributes to the TI cross sections. This leads to a reduction of the DI cross sections produced by electron-impact CI from the $3p$ subshell with subsequent AI at the peak and higher energy side. A change of approximately 9% is observed in the cross sections at the peak value.

4. For B^+ ion, the introduced scaling factors reduce the theoretical SI cross sections more significantly at energies near the ionization threshold than at higher energies. This reduction results in a better agreement with the experimental data. Reasonable agreement with experimental data is achieved for DI cross sections when using the reduced electron-impact CI and CE cross sections.

5. The DDI-AI process accounts for the majority of the total TI cross sections for Se^{2+} and Se^{3+} ions.

   5.1 For Se^{2+} ion, the largest contribution to the total TI cross sections comes from the DDI-AI process, accounting for more than 75% of the total TI cross sections at the peak. Additionally, the DDI(II)-AI process contributes to about 70% of the total DDI-AI cross sections.

   5.2 For Se^{3+} ion, the DDI-AI process contributes to the majority (about 80%) of the TI cross sections. The primary role in the formation of TI cross sections is played by the EII process, followed by AI from the excited levels, which accounts for approximately 83% at the peak value of DDI-AI in the case,

when one of the electrons takes all the excess energy after the first ionization process.

6. BIBLIOGRAPHY

[1] I. Bray, D. V. Fursa, A. S. Kadyrov, A. T. Stelbovics, A. S. Kheifets, and A. M. Mukhamedzhanov, "Electron- and photon-impact atomic ionisation," *Physics Reports*, vol. 520, no. 3, p. 135, 2012.

[2] W. Demtroder, *Atoms, Molecules and Photons*. Springer-Verlag GmbH Germany, 2018.

[3] M. Mohan, *New Trends in Atomic and Molecular Physics*. Springer-Verlag Berlin Heidelberg, 2013.

[4] K. Bartschat and M. J. Kushner, "Electron collisions with atoms, ions, molecules, and surfaces: Fundamental science empowering advances in technology," *Proceedings of the National Academy of Sciences*, vol. 113, no. 26, p. 7026, 2016.

[5] R. K. Smith and N. S. Brickhouse, "Chapter Four - Atomic Data Needs for Understanding X-ray Astrophysical Plasmas," *Advances in Atomic Molecular and Optical Physics*, vol. 63, p. 271, 2014.

[6] M. Hahn and D. W. Savin, "Influence of electron-impact multiple ionization on equilibrium and dynamic charge state distributions: A case study using iron," *The Astrophysical Journal*, vol. 800, no. 1, p. 68, 2015.

[7] E. J. H. J. Bernier and A. Giaccia, "Radiation oncology: A century of achievements," *Nature Reviews Cancer*, vol. 4, no. 9, p. 737, 2004.

[8] Y. Zheng, D. J. Hunting, P. Ayotte, and L. Sanche, "Role of secondary low-energy electrons in the concomitant chemoradiation therapy of cancer," *Phys. Rev. Lett.*, vol. 100, no. 19, p. 198 101, 2008.

[9] O. Rigaud, N. Fortunel, P. Vaigot, E. Cadio, M. Martin, O. Lundh, J. Faure, C. Rechatin, V. Malka, and Y. Gauduel, "Exploring ultrashort high-energy electron-induced damage in human carcinoma cells," *Cell Death & Disease*, vol. 1, e73, 2010.

[10] K. Miyamoto, *Plasma Physics for Controlled Fusion*. Springer-Verlag GmbH Germany, 2016.

[11] V. L. F.B. Rosmej V.A. Astapenko, *Plasma Atomic Physics*. Springer Nature Switzerland AG, 2021.

[12]   A. Müller, "Multiple ionization and the charge state evolution of ions exposed to electron impact," *Physics Letters A*, vol. 113, no. 8, p. 415, 1986.

[13]   K. T. Dolder, M. F. A. Harrison, and P. C. Thonemann, "A measurement of the ionization cross-section of helium ions by electron impact," *Proceedings of the Royal Society of London. Series A, Mathematical and Physical Sciences*, vol. 264, no. 1318, pp. 367–378, 1961.

[14]   R. A. Phaneuf, "Colliding-beams experiments for studying fundamental atomic processes," *Journal of Physics: Conference Series*, vol. 58, no. 1, p. 1, 2007.

[15]   K. Bartschat, "Electron collisions—experiment, theory, and applications," *Journal of Physics B: Atomic, Molecular and Optical Physics*, vol. 51, no. 13, p. 132 001, 2018.

[16]   T. N. Rescigno, M. Baertschy, W. A. Isaacs, and C. W. McCurdy, "Collisional breakup in a quantum system of three charged particles," *Science*, vol. 286, no. 5449, pp. 2474–2479, 1999.

[17]   I. Bray and A. T. Stelbovics, "The convergent close-coupling method for a coulomb three-body problem," *Computer Physics Communications*, vol. 85, no. 1, pp. 1–17, 1995.

[18]   P. G. Burke, *R-Matrix Theory of Atomic Collisions. Application to Atomic, Molecular and Optical Processes*. Springer Berlin, Heidelberg, 2011.

[19]   M. S. Pindzola, F. Robicheaux, S. D. Loch, J. C. Berengut, T. Topcu, J. Colgan, M. Foster, D. C. Griffin, C. P. Ballance, D. R. Schultz, T. Minami, N. R. Badnell, M. C. Witthoeft, D. R. Plante, D. M. Mitnik, J. A. Ludlow, and U. Kleiman, "The time-dependent close-coupling method for atomic and molecular collision processes," *Journal of Physics B: Atomic, Molecular and Optical Physics*, vol. 40, no. 7, R39, 2007.

[20]   M. C. E. Vangioni-Flam and J. Audouze, "Lithium-beryllium-boron: Origin and evolution," *Physics Reports*, vol. 333-334, p. 365, 2000.

[21] R. Lunsford, V. Rohde, A. Bortolon, R. Dux, A. Herrmann, A. Kallenbach, R. M. McDermott, P. David, A. Drenik, F. M. Laggner, R. Maingi, D. K. Mansfield, A. Nagy, R. Neu, and E. Wolfrum, "Active conditioning of asdex upgrade tungsten plasma-facing components and discharge enhancement through boron and boron nitride particulate injection," *Nuclear Fusion*, vol. 59, 2019.

[22] J. Li, Y. P. Zhao, X. M. Gu, C. F. Li, B. N. Wan, X. D. Zhang, J. R. Luo, X. Z. Gong, J. K. Xie, Y. X. Wan, P. J. Qin, X. M. Wang, Y. D. Meng, S. F. Li, X. Gao, Y. Yang, D. Y. Xue, Y. Z. Mao, X. Den, L. Chen, Y. C. Fang, F. X. Yin, S. X. Liu, X. K. Yang, D. Z. Xu, J. Y. Ding, Y. X. Jie, Q. C. Zhao, J. S. Mao, S. Y. Zhang, J. Y. Zhao, J. S. Hu, H. Y. Fan, M. S. Wei, B. L. Lin, G. X. Wang, Y. D. Fang, and W. C. Shen, "ICRF boronization - a new technique towards high efficiency wall coating for superconducting tokamak reactors," *Nuclear Fusion*, vol. 39, no. 8, p. 973, 1999.

[23] J. C. Berengut, S. D. Loch, M. S. Pindzola, C. P. Ballance, and D. C. Griffin, "Electron-impact ionization of the boron atom," *Phys. Rev. A*, vol. 76, no. 4, p. 042 704, 2007.

[24] O. Z. K. Wang and K. Bartschat, "Electron-impact excitation and ionization of atomic boron at low and intermediate energies," *Phys. Rev. A*, vol. 93, no. 5, p. 052 715, 2016.

[25] J. C. Berengut, S. D. Loch, M. S. Pindzola, C. P. Ballance, D. C. Griffin, M. Fogle, and M. E. Bannister, "Electron-impact ionization of B^+," *Phys. Rev. A*, vol. 78, no. 1, p. 012 704, 2008.

[26] O. Woitke, N. Djuri ć, G. H. Dunn, M. E. Bannister, A. C. H. Smith, B. Wallbank, N. R. Badnell, and M. S. Pindzola, "Absolute cross sections for excitation of the $2s^2 \, \vec{S} \, 2p^2 P$ transition in B^{2+} and for electron-impact single ionization of B^{2+}," *Phys. Rev. A*, vol. 58, no. 6, p. 4512, 1998.

[27] R. A. Falk, G. Stefani, R. Camilloni, G. H. Dunn, R. A. Phaneuf, D. C. Gregory, and D. H. Crandall, "Measured electron-impact ionization of be-like ions: B^+, C^{2+}, N^{3+}, and O^{4+}," *Phys. Rev. A*, vol. 28, no. 1, p. 91, 1983.

[28] M. S. Pindzola, J. A. Ludlow, C. P. Ballance, F. Robicheaux, and J. Colgan, "Electron-impact double ionization of B^+," *Journal of*

Physics B: Atomic, Molecular and Optical Physics, vol. 44, no. 10, p. 105 202, 2011.

[29] J. M. Lattimer and D. N. Schramm, "Black-Hole-Neutron-Star Collisions," *Astrophysical Journal*, vol. 192, p. L145, 1974.

[30] S. Wanajo, Y. Sekiguchi, N. Nishimura, K. Kiuchi, K. Kyutoku, and M. Shibata, "Production of all the r-process nuclides in the dynamical ejecta of neutron star mergers," *The Astrophysical Journal Letters*, vol. 789, no. 2, p. L39, 2014.

[31] I. U. Roederer, H. Schatz, J. E. Lawler, T. C. Beers, J. J. Cowan, A. Frebel, I. I. Ivans, C. Sneden, and J. S. Sobeck, "New detections of arsenic, selenium, and other heavy elements in two metal-poor stars*," *The Astrophysical Journal*, vol. 791, no. 1, p. 32, 2014.

[32] A. L. Mashburn, N. C. Sterling, S. Madonna, H. L. Dinerstein, I. U. Roederer, and T. R. Geballe, "Neutron-capture element abundances in magellanic cloud planetary nebulae*," *The Astrophysical Journal Letters*, vol. 831, no. 1, p. L3, 2016.

[33] N. C. Sterling, S. Madonna, K. Butler, J. García-Rojas, A. L. Mashburn, C. Morisset, V. Luridiana, and I. U. Roederer, "Identification of near-infrared Se III and Kr VI emission lines in planetary nebulae," *The Astrophysical Journal*, vol. 840, no. 2, p. 80, 2017.

[34] B. Sharpee, Y. Zhang, R. Williams, E. Pellegrini, K. Cavagnolo, J. A. Baldwin, M. Phillips, and X.-W. Liu, "S-process abundances in planetary nebulae," *The Astrophysical Journal*, vol. 659, no. 2, p. 1265, 2007.

[35] Sterling, N. C. and Witthoeft, M. C., "Atomic data for neutron-capture elements - i. photoionization and recombination properties of low-charge selenium ions," *A&A*, vol. 529, A147, 2011.

[36] I. U. Roederer, "Germanium, arsenic, and selenium abundances in metal-poor stars*," *The Astrophysical Journal*, vol. 756, no. 1, p. 36, 2012.

[37] J. Colgan, D. M. Mitnik, and M. S. Pindzola, "Electron-impact ionization of multiply charged manganese ions," *Phys. Rev. A*, vol. 63, no. 1, p. 012 712, 2000.

[38] G. A. Alna'washi, N. B. Aryal, K. K. Baral, C. M. Thomas, and R. A. Phaneuf, "Electron-impact ionization of se2+," *Journal of Physics B: Atomic, Molecular and Optical Physics*, vol. 47, no. 13, p. 135 203, 2014.

[39] G. A. Alna'washi, K. K. Baral, N. B. Aryal, C. M. Thomas, and R. A. Phaneuf, "Electron-impact ionization of se3+," *Journal of Physics B: Atomic, Molecular and Optical Physics*, vol. 47, no. 10, p. 105 201, 2014.

[40] W. Lotz, "Electron-impact ionization cross-sections and ionization rate coefficients for atoms and ions from hydrogen to calcium," *Zeitschrift für Physik*, vol. 216, no. 3, p. 241, 1968.

[41] V. P. Shevelko, H. Tawara, I. Y. Tolstikhina, F. Scheuermann, B. Fabian, A. Müller, and E. Salzborn, "Double ionization of heavy positive ions by electron impact: Empirical formula and fitting parameters for ionization cross sections," *Journal of Physics B: Atomic, Molecular and Optical Physics*, vol. 39, no. 6, p. 1499, 2006.

[42] M. S. Pindzola and S. D. Loch, "Electron-impact ionization of se2+ and se3+," *Journal of Physics B: Atomic, Molecular and Optical Physics*, vol. 49, no. 12, p. 125 202, 2016.

[43] S. Pakalka, S. Kučas, Š. Masys, A. Kynienė, A. Momkauskaitė, and V. Jonauskas, "Electron-impact single ionization of the Se^{3+} ion," *Phys. Rev. A*, vol. 97, no. 1, p. 012 708, 2018.

[44] V. Jonauskas, A. Prancikevičius, Š. Masys, and A. Kynienė, "Electron-impact direct double ionization as a sequence of processes," *Phys. Rev. A*, vol. 89, no. 5, p. 052 714, 2014.

[45] M. F. Gu, "The flexible atomic code," *Canadian Journal of Physics*, vol. 86, no. 5, p. 675, 2008.

[46] D. H. Sampson, H. L. Zhang, A. K. Mohanty, and R. E. H. Clark, "A dirac-fock-slater approach to atomic structure for highly charged ions," *Phys. Rev. A*, vol. 40, no. 2, p. 604, 1989.

[47] D. H. Sampson, H. L. Zhang, and C. J. Fontes, "A fully relativistic approach for calculating atomic data for highly charged ions," *Physics Reports*, vol. 477, no. 4, p. 111, 2009.

[48] J. C. Slater, "A simplification of the hartree-fock method," *Phys. Rev.*, vol. 81, no. 3, p. 385, 1951.

[49] I. Shavitt, "The history and evolution of configuration interaction," *Molecular Physics*, vol. 94, no. 1, p. 3, 1998.

[50] P.-O. Löwdin, "Correlation problem in many-electron quantum mechanics i. review of different approaches and discussion of some current ideas," in *Advances in Chemical Physics*. John Wiley & Sons, Ltd, 1958, p. 207.

[51] R. Karazija, *Introduction to the Theory of X-Ray and Electronic Spectra of Free Atoms*. Plenum Press, New York, 1996.

[52] S. Kučas, V. Jonauskas, and R. Karazija, "Global characteristics of atomic spectra and their use for the analysis of spectra. IV. configuration interaction effects," *Physica Scripta*, vol. 55, no. 6, p. 667, 1997.

[53] L. Radžiūtė, G. Gaigalas, D. Kato, P. Jönsson, P. Rynkun, S. Kučas, V. Jonauskas, and R. Matulianec, "Energy level structure of Er^{3+}," *Journal of Quantitative Spectroscopy and Radiative Transfer*, vol. 152, p. 94, 2015.

[54] V. Jonauskas, R. Karazija, and S. Kučas, "The essential role of many-electron auger transitions in the cascades following the photoionization of 3p and 3d shells of Kr," *Journal of Physics B: Atomic, Molecular and Optical Physics*, vol. 41, no. 21, p. 215005, 2008.

[55] J. Palaudoux, P. Lablanquie, L. Andric, K. Ito, E. Shigemasa, J. H. D. Eland, V. Jonauskas, S. Kučas, R. Karazija, and F. Penent, "Multielectron spectroscopy: Auger decays of the Krypton $3d$ hole," *Phys. Rev. A*, vol. 82, no. 4, p. 043419, 2010.

[56] V. Jonauskas, S. Kučas, and R. Karazija, "Auger decay of $3p$-ionized Krypton," *Phys. Rev. A*, vol. 84, no. 5, p. 053415, 2011.

[57] V. Jonauskas, A. Momkauskaite, S. Kučas, and R. Karazija, "Intensity enhancement in the emission spectra of Sb, Sn, and W ions due to the mixing of configurations with symmetric exchange of symmetry," *Lithuanian Journal of Physics*, vol. 47, p. 249, 2007.

[58] V. Jonauskas, R. Kisielius, A. Kynienė, S. Kučas, and P. H. Norrington, "Magnetic dipole transitions in $4d^N$ configurations of T ungsten ions," *Phys. Rev. A*, vol. 81, no. 1, p. 012506, 2010.

[59] V. Jonauskas, G. Gaigalas, and S. Kučas, "Relativistic calculations for M1-type transitions in $4d^N$ configurations of W $^{29+}$-W $^{37+}$ ions," *Atomic Data and Nuclear Data Tables*, vol. 98, no. 1, p. 19, 2012.

[60] R. Karazija and S. Kučas, "Average characteristics of the configuration interaction in atoms and their applications," *Journal of Quantitative Spectroscopy and Radiative Transfer*, vol. 129, p. 131, 2013.

[61] H. S. W. Massey and C. B. O. Mohr, "The collision of slow electrons with atoms. i. general theory and elastic collisions," *Proceedings of the Royal Society of London. Series A, Containing Papers of a Mathematical and Physical Character*, vol. 136, no. 829, p. 289, 1932.

[62] H. S. W. Massey and C. B. O. Mohr, "The collision of slow electrons with atoms. ii. general theory and inelastic collisions," *Proceedings of the Royal Society of London. Series A, Containing Papers of a Mathematical and Physical Character*, vol. 139, no. 837, p. 187, 1933.

[63] D. H. Madison and W. N. Shelton, "Distorted-wave approximation and its application to the differential and integrated cross sections for electron-impact excitation of the 2^1P state of helium," *Phys. Rev. A*, vol. 7, no. 2, p. 499, 1973.

[64] Y. Itikawa, "Distorted-wave methods in electron-impact excitation of atoms and ions," *Physics Reports*, vol. 143, no. 2, p. 69, 1986.

[65] P. L. Hagelstein, "Relativistic distorted-wave results for nickel-like gadolinium," *Phys. Rev. A*, vol. 34, no. 2, p. 874, 1986.

[66] G. Gaigalas, Z. Rudzikas, and C. F. Fischer, "An efficient approach for spin - angular integrations in atomic structure calculations," *Journal of Physics B: Atomic, Molecular and Optical Physics*, vol. 30, no. 17, p. 3747, 1997.

[67] M. Hahn, A. Müller, and D. W. Savin, "Electron-impact multiple-ionization cross sections for atoms and ions of helium through zinc," *The Astrophysical Journal*, vol. 850, no. 2, p. 122, 2017.

[68] Y.-K. Kim and M. E. Rudd, "Binary-encounter-dipole model for electron-impact ionization," *Phys. Rev. A*, vol. 50, no. 5, p. 3954, 1994.

[69] Y.-K. Kim, "Scaling of plane-wave born cross sections for electron-impact excitation of neutral atoms," *Phys. Rev. A*, vol. 64, no. 3, p. 032 713, 2001.

[70] Y.-K. Kim and P. M. Stone, "Ionization of boron, aluminum, gallium, and indium by electron impact," *Phys. Rev. A*, vol. 64, no. 5, p. 052 707, 2001.

[71] Y.-K. Kim, "Scaling of coulomb born cross sections for electron-impact excitation of singly charged ions," *Phys. Rev. A*, vol. 65, no. 2, p. 022 705, 2002.

[72] Y.-K. Kim and P. M. Stone, "Ionization of boron, aluminum, gallium, and indium by electron impact," *Phys. Rev. A*, vol. 64, p. 052 707, 5 2001.

[73] Y.-K. Kim and J.-P. Desclaux, "Ionization of carbon, nitrogen, and oxygen by electron impact," *Phys. Rev. A*, vol. 66, p. 012 708, 1 2002.

[74] V. Jonauskas, "Electron-impact double ionization of the Carbon atom," *Astronomy and Astrophysics*, vol. 620, A188, 2018.

[75] A. Kynienė, S. Kučas, S. Pakalka, Š. Masys, and V. Jonauskas, "Electron-impact single ionization of Fe^{3+} from the ground and metastable states," *Phys. Rev. A*, vol. 100, no. 5, p. 052 705, 2019.

[76] V. Jonauskas, "Electron impact single ionization for Si atom," *Atomic Data and Nuclear Data Tables*, vol. 135-136, p. 101 363, 2020.

[77] I. P. Grant, "Gauge invariance and relativistic radiative transitions," *Journal of Physics B: Atomic and Molecular Physics*, vol. 7, no. 12, p. 1458, 1974.

[78] A. Müller, "Electron–ion collisions: Fundamental processes in the focus of applied research," in ser. Advances In Atomic, Molecular, and Optical Physics, E. Arimondo, P. R. Berman, and C. C. Lin, Eds., vol. 55, Academic Press, 2008, p. 293.

[79] M. S. Pindzola, F. Robicheaux, and J. Colgan, "Electron-impact double ionization of h-," *Journal of Physics B: Atomic, Molecular and Optical Physics*, vol. 39, no. 6, p. L127, 2006.

[80] M. S. Pindzola, F. Robicheaux, J. P. Colgan, M. C. Witthoeft, and J. A. Ludlow, "Electron-impact single and double ionization of helium," *Phys. Rev. A*, vol. 70, no. 3, p. 032 705, 2004.

[81] M. S. Pindzola, J. A. Ludlow, C. P. Ballance, F. Robicheaux, and J. Colgan, "Electron-impact double ionization of b+," *Journal of Physics B: Atomic, Molecular and Optical Physics*, vol. 44, no. 10, p. 105 202, 2011.

[82] M. S. Pindzola, J. A. Ludlow, F. Robicheaux, J. Colgan, and D. C. Griffin, "Electron-impact double ionization of magnesium," *Journal of Physics B: Atomic, Molecular and Optical Physics*, vol. 42, no. 21, p. 215 204, 2009.

[83] M. Gryziński, "Classical theory of atomic collisions. I. theory of inelastic collisions," *Phys. Rev.*, vol. 138, no. 2A, A336, 1965.

[84] D. N. Tripathi and D. K. Rai, "Cross Section for Double Ionization by Electron Impact: Li^+, Na^+, K^+," *The Journal of Chemical Physics*, vol. 55, no. 3, p. 1268, 1971.

[85] B. N. Roy and D. K. Rai, "Application of classical collision theory to electron impact double ionization of atoms," *Journal of Physics B: Atomic and Molecular Physics*, vol. 6, no. 5, p. 816, 1973.

[86] L. K. Jha, M. P. Singh, and S. V. K. Kumar, "Double ionization of Ne^{5+} and Ne^{6+} ions by electron impact," *The European Physical Journal D*, vol. 66, p. 1, 2012.

[87] Kumari, S. and Jha, L.K., "Electron impact double ionization of Mg^+ ions," *Eur. Phys. J. D*, vol. 66, no. 4, p. 87, 2012.

[88] Kumari, S., Jha, L. K., and Roy, B. N., "Double ionization of Sc^+ ions by electron impact," *Eur. Phys. J. D*, vol. 55, no. 1, p. 93, 2009.

[89] F. Zhou, Y. Ma, and Y. Qu, "Single, double, and triple auger decay probabilities of $C^+(1s2s^2 2p^2\,{}^2D, {}^2P)$ resonances," *Phys. Rev. A*, vol. 93, no. 6, p. 060 501, 2016.

[90] Y. Ma, F. Zhou, L. Liu, and Y. Qu, "Multiple auger decay probabilities of neon from the $1s$-core-hole state," *Phys. Rev. A*, vol. 96, no. 4, p. 042 504, 2017.

[91] Y. Ma, Z. Liu, F. Zhou, and Y. Qu, "Theoretical investigation of resonant multiple auger decay of the core-excited $2p_{3/2}{}^{-1}4s$ state in argon," *Phys. Rev. A*, vol. 98, no. 4, p. 043 417, 2018.

[92] Y. Ma, L. Liu, Y. Wu, Y. Qu, and J. Wang, "Theoretical investigation of electron-impact multiple ionization of O II − IV ions," *Phys. Rev. A*, vol. 101, no. 5, p. 052 703, 2020.

[93] J. Koncevičiūtė and V. Jonauskas, "Electron-impact double ionization of Li^+," *Phys. Rev. A*, vol. 93, no. 2, p. 022 711, 2016.

[94] V. Jonauskas, L. Partanen, S. Kučas, R. Karazija, M. Huttula, S. Aksela, and H. Aksela, "Auger cascade satellites following 3d ionization in Xenon," *Journal of Physics B: Atomic, Molecular and Optical Physics*, vol. 36, no. 22, p. 4403, 2003.

[95] A. Kramida, Yu. Ralchenko, J. Reader, and and NIST ASD Team, NIST Atomic Spectra Database (ver. 5.10), [Online]. Available: https://physics.nist.gov/asd. National Institute of Standards and Technology, Gaithersburg, MD. 2022.

[96] V. Jonauskas, A. Kynienė, S. Kučas, S. Pakalka, Š. Masys, A. Prancikevičius, A. Borovik, M. F. Gharaibeh, S. Schippers, and A. Müller, "Electron-impact ionization of W^{5+}," *Phys. Rev. A*, vol. 100, no. 6, p. 062 701, 2019.

[97] V. Jonauskas, A. Kynienė, G. Merkelis, G. Gaigalas, R. Kisielius, S. Kučas, Š. Masys, L. Radžiūtė, and P. Rynkun, "Contribution of high-nl shells to electron-impact ionization processes," *Phys. Rev. A*, vol. 91, no. 1, p. 012 715, 2015.

[98] A. Kynienė, Š. Masys, and V. Jonauskas, "Influence of excitations to high-nl shells for the ionization process in the W^{26+} ion," *Phys. Rev. A*, vol. 91, no. 6, p. 062 707, 2015.

[99] A. Kynienė, S. Pakalka, Š. Masys, and V. Jonauskas, "Electron-impact ionization of W^{25+}," *Journal of Physics B: Atomic, Molecular and Optical Physics*, vol. 49, no. 18, p. 185 001, 2016.

[100] V. P. Shevelko, H. Tawara, F. Scheuermann, B. Fabian, A. Müller, and E. Salzborn, "Semiempirical formulae for electron-impact double-ionization cross sections of light positive ions," *Journal of Physics B: Atomic, Molecular and Optical Physics*, vol. 38, no. 5, p. 525, 2005.

[101] D.-H. Zhang and D.-H. Kwon, "Theoretical electron-impact ionization of W^{17+} forming W^{18+}," *Journal of Physics B: Atomic, Molecular and Optical Physics*, vol. 47, no. 7, p. 075 202, 2014.

[102]   A. Kynienė, G. Merkelis, A. Šukys, Š. Masys, S. Pakalka, R. Kisielius, and V. Jonauskas, "Maxwellian rate coefficients for electron-impact ionization of W^{26+}," *Journal of Physics B: Atomic, Molecular and Optical Physics*, vol. 51, no. 15, p. 155 202, 2018.

[103]   F. Jin, A. Borovik, B. Ebinger, and S. Schippers, "Electron-impact single ionisation of W^{14+} ions: Subconfiguration-average and level-to-level distorted wave calculations," *Journal of Physics B: Atomic, Molecular and Optical Physics*, vol. 53, no. 7, p. 075 201, 2020.

7.   ACKNOWLEDGEMENTS

I dedicate this dissertation to my son, Arnas, for being both my greatest challenge and my most significant achievement.

I wish to extend my deepest appreciation to my academic supervisor, Assoc. Prof. Dr. Valdas Jonauskas. His guidance, support, patience, inspiration, and commitment to my research have been invaluable during my doctoral studies. Without his support, this journey would have been far more challenging.

I would also like to thank my family (my husband, my mother, and my aunt) for their support and encouragement throughout the process of writing this dissertation. They've been a constant source of motivation for me.

8. PUBLICATIONS ON THE SUBJECT OF THE DISSERTATION

8.1. Articles

A1 **J. Koncevičiūtė**, S. Kučas, Š. Masys, A. Kynienė, and V. Jonauskas, "Electron-impact triple ionization of Se^{2+}", Phys. Rev. A., vol. 97, no. 1, p. 012705, January 2018

A2 **J. Koncevičiūtė**, S. Kučas, A. Kynienė, Š. Masys, and V. Jonauskas, "Electron-impact double and triple ionization of Se^{3+}", J. Phys. B: At. Mol. Opt. Phys., vol. 52, no. 2, p. 025203, November 2018

A3 **J. Koncevičiūtė**, and V. Jonauskas, "Electron-impact single, double, and triple ionization of B^+", Phys. Rev. A., vol. 104, no. 4, p. 042804, October 2021

8.2. Conference Presentations

C1 Lithuanian National Physics Conference. Poster presentation "Electron-impact double ionization of Se^{2+}", Vilnius, Lithuania, 2017.

C2 31st International Conference on Photonic, Electronic and Atomic Collisions (ICPEAC XXXI). Poster presentation "Double photoionization of He isoelectronic sequence", Deauville, France, 2019.

C3 31st International Conference on Photonic, Electronic and Atomic Collisions (ICPEAC XXXI). Poster presentation "Radiative and Auger cascades in Fe^{3+}", Deauville, France, 2019

C4 31st International Conference on Photonic, Electronic and Atomic Collisions (ICPEAC XXXI). Poster presentation "Cascade of elementary processes in Se^+", Deauville, France, 2019.

C5 32st International Conference on Photonic, Electronic and Atomic Collisions (ViCPEAC 2021). Poster presentation "Electron-impact double ionization of B^+", held in virtual format, 2021.

NOTES

NOTES

NOTES